

# Pristine and Novel Fullerene Derivatives as Charge Transporting Materials or Additives in Perovskite Solar Cells

**Author**

*Silvia Collavini*

*Year 2019*

**Supervisors**

*Prof. Juan Luis Delgado*

Hybrid Materials for Photovoltaics Group

**POLYMAT**

*Dr. Ramón Tena-Zaera*

Institute for Surface Engineering

**CIDETEC**

eman ta zabal zazu



Universidad del País Vasco    Euskal Herriko Unibertsitatea

**POLYMAT**  
Basque Center for  
Macromolecular Design and Engineering

**cidetec** >  
surface engineering



*Only the chemist can tell, and not always the chemist,  
What will result from compounding  
Fluids or solids.  
And who can tell  
How men and women will interact  
On each other, or what children will result?  
There were Benjamin Pantier and his wife,  
Good in themselves, but evil toward each other;  
He oxygen, she hydrogen,  
Their son, a devastating fire.  
I Trainor, the druggist, a mixer of chemicals,  
Killed while making an experiment,  
Lived unwedded.*

**Trainor the Druggist**

Edgar Lee Masters-Spoon River Anthology, 1915



# Table of Contents

---

Acknowledgements .....	7
Abstract .....	11
Resumen .....	17
Riassunto .....	23
Laburpena .....	29
Abbreviations .....	33
1. Introduction .....	39
1.1 Solar Energy and Perovskite Solar Cells .....	39
1.2 Fullerenes in Perovskite Solar Cells .....	59
1.3 Conclusions .....	71
2. Objective .....	73
3. Results and Discussion .....	75
3.1 Pristine Fullerenes as ETMs in Regular, Compact PSCs .....	77
3.2 PEG-C <sub>60</sub> -based Materials as additives for PSCs .....	99
3.3 Innovative HTMs with C <sub>60</sub> core .....	137
4. References .....	191



# Acknowledgements

---

First of all I would like to acknowledge Professor Juan Luis Delgado for the great scientific and emotional support. Thanks for having believed in me when no one else did, not even myself. Thanks again for all the opportunities you gave me and the challenges you made me face. I grew up a lot during these years. Thanks also to absolutely everyone who is and was part of the Hybrid Materials for Photovoltaic Group for making it what it is now.

Thanks to my co-supervisor Doctor Ramón Tena-Zaera for welcoming me in Cidetec and introducing me to the amazing world of perovskite device fabrication. Thank you also for trusting me for later projects developed here in Polymat. Thanks to the whole Cidetec group, especially to Sandra, for the excellent support and friendship.

Thanks to Izaskun Balza, Idoia Azaldegui, Dr. Monica Moreno, and Liudmila Zhyhmiantovic for being the backbone of Polymat Fundazioa and for their never-ending patience.

Thanks to all Polymat, especially to Professor José M. Asua, for allowing me to develop my projects.

Thanks to all the technicians that helped me (a lot) through these years with any kind of analysis. I would especially acknowledge Dr. Sofia Guezala, Dr. JI Miranda, and Dr. Javier Calvo for their enormous help in any situation.

Thanks to Professor Michael Grätzel, Professor Anders Hagfeldt, Dr. Shaik Zakeeruddin, Dr. Michael Saliba, Dr. Wolfgang Tress, Dr. Silver Turren, Dr. Konrad Domanski, Dr. Amita Ummadisingu, Philippe Holzhey, Michael Prettl, and Heidi Francelet for the huge help and support during my internship in EPFL, and for the friendship.

Thanks to Professor Aurelio Mateo-Alonso and his group for their help with electrochemistry and UV spectroscopy and for the fun.

Thanks to Dr. Iván Mora-Seró and Marta Vallés-Pelarda from the Institute of Advanced Materials (UJI) for the great role they played with their photovoltaic studies.

Thanks to Dr. Luis Hueso and Elisabetta Zuccatti for the preparation and study of OFET devices.

---

Time to get less formal and to switch languages every now and then!

Vorrei iniziare ringraziando tutta la mia famiglia dal profondo del cuore. In particolare modo:

## Acknowledgements

Mio padre, che una volta pensionato è ringiovanito di almeno 15 anni ed è pieno di voglia di fare ma spesso si ritrova bloccato in quanto coperto da gatti.

Mia madre, che è la donna più buona e forte del mondo, che si fa in quattro per gli altri mentre si meriterebbe solo di poter stare tranquilla a casa facendosi coprire da gatti.

Il mio Pallino, che ha tanta difficoltà a credere che è una persona splendida e che vorrei riuscire a uguagliare in intelligenza e apertura mentale. Non dimenticare che sono la tua più grande fan (sì Luigi, hai letto bene).

Mia nonna Edda, che anche se gli anni passano e succedono cose brutte ha la stessa forza di sempre.

Mia zia Carmen, con le sue energie e il suo appoggio. Grazie a te e a Claudio per avermi fatto una bellissima visita!

Mio circa-cognato Luigi, l'hacker bianco. Grazie per la tua amicizia, la gorgopera e soprattutto per far felice al mio Pi ed è una cosa per cui ti vorrò bene sempre.

Last but not least nel paragrafo famiglia: Marco. Dire che sei come un fratello è quedarse corti. Grazie per le risate, la pizza, Kimmy, Tiger, Sharknado, i barbogianni, la Lidl, Padre de Familia, i terrapiattisti, gli involtini vietnamiti, il Mumi, il supporto costante, il bar dove sei stato un paio di volte con Darnelle, Misery Bear, il guacamole anche se non più, the Good Place, il Sushi. Potrei nominare ancora mille cose ma in realtà potevo fermarmi a grazie per essere come sei e per strapparmi sempre un sorriso. E grazie Mauro, che non sei solo "il ragazzo di Marco"; grazie per la tua amicizia (un onore) e per saper sempre dire le cose giuste al momento giusto.

Gracias Silvia (no pongo letras para identificarte, espero que sea claro ya que soy yo la que escribe). Mi BFF, mi mitad del microclima perfecto. Sin ti estos años habrian sido vacios. Te quiero muchisimo y te deseo lo mejor. Escribir esto a un metro de ti se me hace raro, pero es lo que hay y hay que aprovechar de esto hasta que dura! TQM VM.

Gracias Jorge, con tu alma tan parecida a la mia. No quiero ser ñoña, de hecho no es un piropo.

Gracias Marta, la mejor y la más dulce compañera de zumba del mundo mundial.

Gracias Melissa; acabas de llegar pero es como si siempre hubieras estado. Eres una maquina!

Gracias Javi por fabricarme un bastón para empujarme mejor más allá de mis límites.

Gracias Jose, te debo una Navidad. Nadie nunca habia hecho esto para mi, nunca podré olvidarlo.

Gracias Sebastian, empezar el grupo contigo ha sido un honor. Tu ayuda ha sido fundamental muchisimas veces y siempre te lo agradeceré.

Gracias Juanpi por recordarme que siempre hay alguna razón para sonreir.

Gracias Alberto, el niño original. Gracias por todas las risas que haces que me eche.

Gracias Felix por esa mirada que lanzas cuando te das cuenta que ya te he convencido para que nos tomemos (...) una mas.

Gracias Bet, que para mi venciste tu vertigo. Y de nada, porque te lo pasaste genial!



Gracias Rajeev, the less-indianlike Indian I have met. I will never ever forget your face of pure (evil) joy after the door prank.

Gracias Ottavia por todas las energias que has traído contigo al llegar aquí, y por haber siempre mantenido fuerte el animo del laboratorio.

Gracias a todos los demás que en los años han pasado por este laboratorio y por mi camino laboral. Belen, con la que he empezado regular y acabado (no, no se acabó) fenomenal. Shagha y Ali y el San Sebastián Film Festival. Cristian, mi primer compañero en Donosti. Gabriella y su espíritu tan grande que todavía me pregunto como pueda caber en un cuerpo tan pequeño. Valentina que estuvo allí cuando más lo necesitaba. Helena y su fuerza para luchar para las causas sociales. Miki por habernos acogido en lo que era su espacio. Os quiero a tod@s!

Gracias Ela. Es un honor poderme definir tu amiga. Has hecho mi estancia más ligera y me has mejorado como persona. Te quiero muchísimo, y a los gatis también.

Gracias Nati, tica de mi corazón. Aunque estemos lejos se que siempre estaremos allí la una para la otra.

Danke Phil für deine Freundschaft und deine Hilfe mit Solarzellen und...Leben. Danke für unsere Skypeanrufe, die mir in schlechten Momenten sehr geholfen haben.

Grazie, Elisa e Valentina. Due parti fondamentali del mio cuore e che so che ci saranno sempre, e io per loro. Dovreste venire qui più spesso.

Grazie Elisabetta. Troppo poco tempo per tanti progetti e tante emozioni. Continua così come sei, ma soprattutto continuiamo ad essere amiche e creative.

Grazie Lorenzo, vederti così "spesso" questi anni è stato importante. Grazie per le chiacchiere rilassanti, profonde e divertenti.

Gracias a los chicos del Rincon del Languí por las super risas, en especial a Roberto, que en poco tiempo se ha vuelto un amigo muy especial y una de las pocas personas con las que puedo hablar horas por Skype sin que me dé ansiedad.

Gracias Teresa, contigo siempre me siento como si estuviera en familia.

Gracias a Laura San Francisco porque es una de las razones para las que tuve fuerzas para seguir adelante.

Gracias a todos los que fueron parte de mi tiempo y de mi corazón en los últimos años, en lo bueno y en lo malo.

Grazie Andrea. Con te tutto è più bello. Ci completiamo e sosteniamo a vicenda in tutto e per tutto, ed è importante. Grazie per avermi sempre appoggiato e resa quello che sono. Non vedo l'ora di passare il resto della mia vita con te. Ti amo.



# Abstract

---

*"The molecule, buckminsterfullerene, is beautiful physically and intellectually. Its qualities, and even some of its properties, can be appreciated instantly and intuitively by nonscientists"*

Hugh Aldersey-Williams, *The Most Beautiful Molecule*

John Wiley & Sons, 1995

At the moment of their discovery, fullerenes and perovskite solar cells represented two enormous breakthroughs within the extended field of material sciences.

With their detection in the mid-eighties, fullerenes opened a whole new pathway through the amazing world of carbon chemistry. This carbon allotrope presents unique structure and properties that made it a leading character in many branches of biochemistry and material science.

Perovskite solar cells have a more recent yet bursting development. In just ten years, this new kind of photovoltaic devices saw its power conversion efficiency rise from 3.8% to 23.7%. That's not all though:

all the clues indicate that even higher efficiencies could be reached in a near future.

The merge of these two VIPs (Very Important Players) of materials science couldn't bring anything but great scientific development. In fact, the versatility of fullerene chemistry and applications combined with the potential of perovskite solar cells afforded a huge variety of solar cells with improved properties. Interestingly, the role played by fullerenes cannot be confined to a single function: in this dissertation, fullerenes will be presented as either electron or hole transporting / electron blocking materials, or as additives within the perovskite layer.

In the first chapter, well-known inorganic electron-transporting material  $\text{TiO}_2$  is replaced with pristine  $\text{C}_{60}$  and  $\text{C}_{70}$ .  $\text{TiO}_2$  is usually the first choice when preparing a regular perovskite solar cell; however it presents some issues that could hamper the possibility for perovskite solar cells to be competitive throughout the market. In fact, the high temperatures (i.e. close to  $500^\circ\text{C}$ ) make the cells' preparation too expensive to be cost-effective. Fullerenes, in this sense, could easily favour the high-scale preparation since no sintering is required; therefore the high-temperature step is not necessary. In this work, an easy all-solution processing of fullerene is proposed, as well as an exhaustive study on the film thickness and morphology. In order to improve the film quality, an interesting technique is proposed: the so-called "fullerene saturation approach". This strategy consists in preparing the perovskite solution dissolving

the components in a solvent which was previously saturated with the required fullerene. Several goals have been reached within this study. First of all, the viability of using solution-processed  $C_{70}$  as electron transporting material in efficient perovskite solar cells was demonstrated. This paves the way for the use of new materials for the electron transport in perovskite solar cells, in particular those that may have been excluded initially because of their relatively low electron mobility and significant absorption in the visible range of the electromagnetic spectrum. Finally, the issue of solubility is bypassed since the fullerene saturation approach allows processing the perovskite layer on materials which are soluble in either DMF or DMSO.

In the following section, a family of  $C_{60}$  monoadducts covalently functionalized with the polymer polyethylene glycol (PEG) is presented. These novel  $C_{60}$ -based materials have been incorporated as additives in  $CH_3NH_3PbI_3$  (MAPbI<sub>3</sub>), the most common organic-inorganic perovskite used in this kind of solar cells. The fullerene-containing cells, thanks to the peculiar nature of the new fullerene additives, showed increased stability against moisture. This seems to be due to the action of the PEG, which coordinates water molecules and thus prevents them to reach and degrade perovskite crystals. Moreover, the nature of the additives, thanks to the presence of the fullerene cage, helped reducing hysteresis. This phenomenon causes a discrepancy between the cell performances when they are measured either backwards (from a definite voltage value to zero) or

forwards (from zero to a definite voltage value) and results in an inaccurate efficiency measurement when this is extracted from a current density–voltage ( $J$ – $V$ ) curve. This phenomenon should be avoided in sight of future commercialization. Several studies have led to the conclusion that fullerenes can limit each one of the possible causes of hysteresis, such as interfacial charge accumulation, charge traps, and ion migration.

In the last of the studies, an innovative application of fullerenes in photovoltaics is presented. In fact, the first molecule with fullerene core and hole-transporting activity was synthesized, characterized, and tested as a hole-transporting/electron-blocking material with interesting results. Even though the fullerene core presents a well-known electron-transporting activity, an appropriate substitution could tailor the HOMO and LUMO to the extent that the overall charge-transporting ability of the resulting molecule is completely changed. It is important to point out the fact that no additive was used in the preparation of the novel fullerene films. Usually, the use of additives is required to increase the conductivity of hole transporting materials, just as it happens for the most common one, Spiro-OMeTAD. However, the introduction of these additives has some important drawbacks, being the reduction of long-term stability the most important one. In this sense, the possibility of working efficiently without additives is highly remarkable. Furthermore, for the first time a “fullerene-sandwich” perovskite

solar cell, in which both charge-transporting materials possess fullerene nature, is presented.

In this thesis the chemical versatility of fullerenes was implemented in order to obtain efficient and stable perovskite solar cells. Thus fullerenes and novel fullerene derivatives were used as ETMs, HTMs, or additives within the perovskite layer, illustrating the broad range of applications of these outstanding molecules.





# Resumen

---

*“La molécula, buckminsterfullerene, es hermosa físicamente e intelectualmente. Sus cualidades, y también algunas de sus propiedades, pueden ser apreciadas de forma instantánea e intuitiva por gente ajena al mundo científico.”*

Hugh Aldersey-Williams, *The Most Beautiful Molecule*

John Wiley & Sons, 1995

Los fullerenos y las celdas solares de perovskita constituyen dos enormes avances en el extenso campo de la ciencia de los materiales. Con su descubrimiento a mediados de los años ochenta, los fullerenos abrieron un nuevo camino a través del emocionante mundo de la química del carbono. Este alótropo del carbono posee una estructura y propiedades únicas, que lo han convertido en un protagonista en muchas ramas de la bioquímica y de la ciencia de los materiales.

Las celdas solares de perovskita se han desarrollado más recientemente, no obstante su desarrollo se ha producido de una forma muy rápida. En tan solo diez años, este nuevo tipo de

dispositivos fotovoltaicos vio su eficiencia subir de 3.8% hasta 23.7%. Y eso no es todo: todos los factores indican que eficiencias aun más altas pueden ser alcanzadas.

La fusión de estos dos VIPs (Very Important Players) de la ciencia de materiales está por lo tanto destinada a aportar grandes avances científicos. De hecho, la versatilidad de la química y de las aplicaciones de los fullerenos junto con el potencial de las celdas solares de perovskita ha proporcionado una gran variedad de celdas solares con propiedades mejoradas. Curiosamente, el papel desempeñado por los fullerenos no puede limitarse a una única función: en esta tesis, los fullerenos serán presentados como transportadores de electrones o de huecos / bloqueadores de electrones, o como aditivos dentro de la capa de perovskita.

En el primero de los proyectos desarrollados, el material transportador de electrones inorgánico más conocido,  $\text{TiO}_2$ , se reemplaza por  $\text{C}_{60}$  y  $\text{C}_{70}$ . El  $\text{TiO}_2$  suele ser la primera opción cuando se prepara una celda solar de perovskita con arquitectura regular; sin embargo, presenta algunos problemas que podrían dificultar la posibilidad de que las celdas solares de perovskita sean competitivas en todo el mercado. De hecho, las temperaturas extremadamente altas requeridas hacen que la preparación de las celdas sea demasiado costosa para ser rentable. Los fullerenos, en este sentido, podrían favorecer la preparación a gran escala ya que no se requiere sintering; por lo tanto, no es necesario alcanzar altas temperaturas en la fase de preparación de la celda. En este trabajo, se propone una

simple estrategia de preparación de capas de fullereno procesando disoluciones, así como un estudio exhaustivo sobre el espesor de la capa de fullereno y la morfología. Con el fin de mejorar la calidad de la capa, se propone una técnica interesante: el "fullerene-saturation approach". Esta estrategia consiste en preparar la solución de perovskita disolviendo los componentes en un disolvente previamente saturado con el fullereno requerido. Dentro de este estudio se han alcanzado varios objetivos. En primer lugar, se demostró la viabilidad de utilizar  $C_{70}$  procesado en solución como material de transporte de electrones en células solares de perovskita eficientes. Esto abre la puerta para el uso de nuevos materiales para el transporte de electrones en células solares de perovskita, en particular aquellos que pueden haber sido excluidos inicialmente debido a su movilidad de electrones relativamente baja y su absorción significativa en el rango visible del espectro electromagnético. Finalmente, el problema de la solubilidad se evita, ya que el "fullerene saturation approach" permite procesar la capa de perovskita en materiales que son solubles en DMF o DMSO.

En la siguiente sección, se presenta una familia de monoadductos del fullereno  $C_{60}$  funcionalizados covalentemente con el polímero polietilenglicol (PEG). Estos nuevos materiales basados en  $C_{60}$  se han incorporado como aditivos en  $CH_3NH_3PbI_3$  ( $MAPbI_3$ ), la perovskita híbrida orgánico-inorgánica más común, utilizada en este tipo de celdas solares. Las celdas que contienen fullereno, gracias a la naturaleza peculiar de los nuevos aditivos, mostraron una mayor

estabilidad contra la humedad. Esto parece deberse a la acción del PEG, que coordina las moléculas de agua y, por lo tanto, evita que reaccionen con los cristales de perovskita y los degraden. Además, la naturaleza de los aditivos ayudó a reducir la histéresis debido a la presencia de la esfera de fullereno. Este fenómeno provoca una discrepancia entre los rendimientos de las celdas cuando se miden de cero a un valor de voltaje definido o al revés y da como resultado una medición imprecisa de la eficiencia cuando se extrae de una curva de densidad de corriente-voltaje ( $J-V$ ). Este fenómeno debe evitarse ante la futura comercialización. Varios estudios han llevado a la conclusión de que los fullerenos pueden limitar cada una de las posibles causas de histéresis, como la acumulación de carga interfacial, las trampas de carga y la migración de iones.

En el último de los estudios, se presenta una aplicación innovadora de fullerenos en fotovoltaica. De hecho, en este capítulo se reporta la síntesis y caracterización –mediante técnicas espectroscópicas habituales- de la primera molécula con núcleo de fullereno y actividad para el transporte de huecos. Se demuestra la viabilidad de usar este innovador material como un material transportador de huecos/bloqueador de electrones en celdas solares de perovskita con resultados interesantes. Aunque el núcleo de fullereno presenta una actividad de transportador de electrones bien conocida, una sustitución apropiada puede adaptar el HOMO y el LUMO en la medida en que la capacidad general de transporte de carga de la molécula resultante se modifique por completo. Es importante

señalar el hecho de que no se utilizó ningún aditivo en la preparación de los films de fullereno. Por lo general, se requiere el uso de aditivos para aumentar la conductividad de los materiales transportadores de huecos, como en el caso del más común, Spiro-OMeTAD. Sin embargo, la introducción de estos aditivos tiene algunos inconvenientes importantes, como por ejemplo la reducción de la estabilidad a largo plazo. En este sentido, la posibilidad de obtener dispositivos fotovoltaicos eficientes sin usar aditivos dopantes es especialmente destacable. Además, por primera vez se presenta una celda solar de perovskita "fullerene-sandwich", en la que ambos materiales de transporte de carga poseen núcleo fullerenico.

En esta tesis hemos implementado la versatilidad química de los fullerenos, para obtener células solares de perovskita eficientes y estables. Por lo tanto, hemos sintetizado y usado fullerenos o derivados de fullereno como transportadores de electrones, transportadores de huecos o aditivos dentro de la capa de perovskita, lo que ilustra la amplia gama de aplicaciones de estas sorprendentes moléculas.



## Riassunto

---

*“La molecola, buckminsterfullerene, è bella fisicamente e intellettualmente. Le sue qualità, e anche alcune delle sue proprietà, possono essere apprezzate istantaneamente e intuitivamente dai non-scienziati.”*

Hugh Aldersey-Williams, *The Most Beautiful Molecule*

John Wiley & Sons, 1995

I fullereni e le celle solari di perovskite rappresentano due enormi innovazioni nell'ampio settore delle scienze dei materiali.

Con la loro scoperta a metà degli anni ottanta, i fullereni hanno aperto una nuova strada attraverso l'emozionante mondo della chimica del carbonio. Questo allotropo del carbonio possiede una struttura e delle proprietà uniche, che lo hanno reso un protagonista in molte branche della biochimica e delle scienze dei materiali.

Le celle solari di perovskite hanno un'evoluzione più recente, tuttavia esplosiva. In solo 10 anni, questo nuovo tipo di dispositivi solari ha visto la sua efficienza crescere da 3.8% a 23.7%. E non è

finita: tutto indica che efficienze ancora maggiori possano essere raggiunte.

La fusione di questi due VIPs (Very Important Players) delle scienze dei materiali non poteva essere che portare a grandi innovazioni scientifiche. Infatti, la versatilità della chimica e delle applicazioni dei fullereni combinate con il potenziale delle celle di perovskite ha portato a una gran varietà di celle solari con caratteristiche migliorate. Curiosamente, il ruolo del fullerene non può essere limitato a un'unica funzione: in questa tesi, i fullereni saranno presentati sia come materiali trasportatori di elettroni o di lacune elettroniche, sia come additivi posti all'interno dello strato di perovskite.

Nel primo dei progetti, il più diffuso materiale inorganico trasportatore di elettroni  $\text{TiO}_2$  è stato sostituito con pristini  $\text{C}_{60}$  e  $\text{C}_{70}$ .  $\text{TiO}_2$  è di solito la prima scelta quando si prepara una cella solare di perovskite con architettura regolare; tuttavia presenta alcuni problemi che potrebbero ostacolare la possibilità per le celle solari di perovskite di essere competitive sul mercato. Infatti, le temperature estremamente elevate richieste per il processo di sinterizzazione del  $\text{TiO}_2$  rendono la preparazione delle celle troppo costosa per essere redditizia. I fullereni, in questo senso, potrebbero facilmente favorire la preparazione su larga scala poiché non è richiesta alcuna sinterizzazione; quindi ricorrere ad alte temperature non è necessario. In questo lavoro viene proposto un facile protocollo di preparazione dei film di fullerene interamente a partire da soluzioni,



oltre a uno studio approfondito sullo spessore e la morfologia dei film di fullerene. Per migliorare la qualità del film, viene proposta una tecnica interessante: il cosiddetto "fullerene-saturation approach". Questa strategia consiste nel preparare la soluzione di perovskite sciogliendo i componenti in un solvente che è stato precedentemente saturato con il fullerene prescelto. Diversi obiettivi sono stati raggiunti all'interno di questo studio. Innanzitutto, è stata dimostrata la possibilità di utilizzare  $C_{70}$  processato in soluzione come materiale di trasporto di elettroni in celle solari di perovskite efficienti. Questo apre la strada all'utilizzo di nuovi materiali per il trasporto degli elettroni nelle celle solari di perovskite, in particolare quelli che potrebbero essere stati esclusi inizialmente a causa della loro mobilità elettronica relativamente bassa e dell'assorbimento significativo nel campo visibile dello spettro elettromagnetico. Infine, il problema della solubilità viene aggirato poiché il "fullerene saturation approach" consente di elaborare lo strato di perovskite su materiali solubili in DMF o DMSO.

Nella sezione seguente, viene presentata una famiglia di monoaddotti del  $C_{60}$  funzionalizzati covalentemente con il polimero polietilenglicole (PEG). Questi nuovi materiali a base di  $C_{60}$  sono stati incorporati come additivi in  $CH_3NH_3PbI_3$  ( $MAPbI_3$ ), la perovskite ibrida organica-inorganica più comunemente utilizzata in questo tipo di celle solari. Le celle contenenti fullerene, grazie alla natura particolare dei nuovi additivi, hanno mostrato una maggiore stabilità contro l'umidità. Questo sembra essere dovuto all'azione del PEG,

che coordina le molecole d'acqua e quindi impedisce loro di raggiungere e degradare i cristalli di perovskite. Inoltre, la natura degli additivi, grazie alla presenza della sfera di fullerene ha aiutato a ridurre l'isteresi. Questo fenomeno causa una discrepanza tra le prestazioni delle celle quando vengono misurate da un valore di tensione definito a zero o nel verso opposto, e risulta in misurazioni inaccurate dell'efficienza quando questa viene estratta da una curva di densità di corrente/voltaggio (J-V). Questo fenomeno dovrebbe essere evitato in vista della futura commercializzazione. Diversi studi hanno portato alla conclusione che i fullereni possono limitare ciascuna delle possibili cause dell'isteresi, come l'accumulo di carica interfacciale, le trappole di carica e la migrazione di ioni.

Nell'ultimo degli studi, viene presentata un'applicazione innovativa dei fullereni in fotovoltaica. In effetti, la prima molecola con attività di trasportatore di lacune elettroniche avente nucleo fullerenico è stata sintetizzata e caratterizzata e testata come materiale trasportatore di lacune/bloccante di elettroni con risultati interessanti. Anche se il nucleo di fullerene presenta una ben nota attività di trasportatore di elettroni, una sostituzione appropriata potrebbe modificare l'HOMO e il LUMO al punto tale da cambiare completamente la capacità complessiva di trasporto di carica della molecola. È importante sottolineare il fatto che nessun additivo è stato utilizzato nella preparazione dei film di fullerene. Solitamente, è necessario l'uso di additivi per aumentare la conduttività dei materiali trasportatori di lacune elettroniche, come nel caso del più

comune, Spiro-OMeTAD. Tuttavia, l'introduzione di questi additivi presenta alcuni importanti inconvenienti, tra cui la riduzione della stabilità a lungo termine. In questo senso, la possibilità di lavorare in modo efficiente senza additivi è davvero importante. Inoltre, viene presentata per la prima volta una cella solare di perovskite "fullerene-sandwich", in cui entrambi i materiali che trasportano le cariche presentano natura fullerenica.

In questo lavoro di tesi abbiamo implementato la versatilità chimica dei fullereni con lo scopo di ottenere celle solari di perovskite efficienti e stabili. Pertanto, fullereni e nuovi derivati sono stati usati come trasportatori di elettroni, di lacune elettroniche o come additivi della perovskite, dimostrando l'ampia gamma di applicazioni di queste sorprendenti molecole.



# Laburpena

---

*“Molekula hau, buckminsterfullerene, fisikoki eta intelektualki ederra da. Bere kalitatea, eta era berean bere ezaugarrietako batzuk, intuitiboki berehala antzeman daitezke, zientzian jarduten ez duen jendeagatik ere.”*

Hugh Aldersey-Williams, *The Most Beautiful Molecule*

John Wiley & Sons, 1995

Fullerenoak eta perovskitako eguzki-zelulak materialen zientziako arlo zabalaren aurrerapen handienetarik bi izan dira. Haien aurkikuntzarekin 1980-ko hamarkadan, fullerenoak bide berri bat ireki zuten karbonoaren kimika-mundu zirrargarrian zehar. Estructura eta propietate bereziak bere ditu karbonoaren alotropo honek, izan ere biokimika eta materialen zientzien adar askoren protagonista agertu da.

Perovskitako eguzki-zelulak duela gutxiago garatu dira, baina bat-batean fullerenoekin komparatuz. Hamar urteetan zehar besterik ez zelula fotovoltaiko mota honek ikusi du bere efizientzia 3.8%-tik

23.7%-ra igotzen. Eta hau ez da guztia: jakina da are efizientzia altuagoak lortu daitezkeela.

Bi zientzien VIP (Very Important Players) hauen fusioa ezin liteke ezer baina harrigarria izan. Izan ere, fullerenoen aniztasun kimikoak eta aplikagarritasunak, perovskita-materialen potentzialarekin batera, propietate aurreratuak dituzten eguzki-zelula mota berrien garapena ahalbidetu zuten. Gailu hauetan fullerenoen zeregina ez da bat bakarra, zeren kontaktu selektibo zein aditibo bezala perovskitako geruzaren barne jardun daiteke.

Edozein kasuan, bi mundu hauen bat-egitea sekulako emaitzak eman zituen.

Garatutako lehen proiektuan, elektroieramaile material inorganiko ezagunena,  $\text{TiO}_2$ ,  $\text{C}_{60}$  eta  $\text{C}_{70}$  fullerenoengatik ordezkutzen da. Normalean  $\text{TiO}_2$  lehen aukera izaten da arkitektura arruntarako; hala eta guztiz ere, zenbait arazo dakartza berekin perovskita-gailuen merkaturatzeari begira. Hau da, zelula hauek prestatzeko tenperatura oso altuak erabili behar dira, industriarako bideragarritasuna oztopatuz. Zentzu honetan, fullerenoak eskala handian erabilgarriagoak gerta litezke *sintering*-a beharrezkoa ez izanda; hortaz, ez dira zertan tenperatura altuak lortu behar. Lan honetan fullereno geruza hauek prestatzeko estrategia erraza proposatzen da, era berean fullereno geruzaren lodiera eta morfologia inguruko ikerketa eginez. Geruza honen kalitatea hobetzea bilatzearekin batera, teknika interesgarri berri bat proposatzen da, “fullerene-saturation approach” deiturikoa.

Estrategia honek perovskita disoluzioa fullerenoarekin saturatzea gomendatzen du, fullereno geruza disolbatu ez dadin. Ikerketa honen barruan hainbat helburu lortu dira. Lehenik eta behin, soluzioan prozesatutako C70-ren erabilgarritasuna material elektroieramaile bezala perovskita eguzki-zelula efizienteetan frogatu zen. Honek bidea irekitzen du perovskita eguzki-zeluletan material berrien erabilerarako, zehazki hasieratik baztertu zirenak haien elektroimobilitate erlatiboki baxuagatik edo argi ikusgaiaren eremu elektromagnetikoan absorzio garrantzitsuagatik. Amaitzeko, disolbagarritasunaren arazoa sahiesten da, "fulleren saturation approach" izenekoak perovskita geruzak prozesatzea ahalbidetzen baitu DMSO edo DMF-n disolbagarriak diren materialen gainean.

Hurrengo atalean polietilenglikol (PEG) polimeroarekin funtzionalizatutako C<sub>60</sub> fullereno monoaduktoak aurkezten dira. C<sub>60</sub>-an funtsatutako material berri hauek aditibo bezala gehitu ziren CH<sub>3</sub>NH<sub>3</sub>PbI<sub>3</sub> (MAPbI<sub>3</sub>) perovskitan, perovskita hibrido organiko-inorganiko erabiliena eguzki-zelula hauetan zehazki. Fullerenoa duten gailuak, molekula berri hauen izaera partikularra dela eta, hezetasunaren kontrako estabilitate hobetuarekin agertu ziren. Eragin hau PEG-ari esker izan daiteke, ur molekulekin koordinatzen baita eta, hortaz, hauek perovskita kristaletara heltzea, eta beraz degradatzea, sahiesten du. Gainera, aditibo hauen izaerak histeresia gutxiagotzen lagundu zuen, zehazki zelulen etekina korrante-tentsio (*J-V*) kurba zentzu ezberdinetan neurtzerakoan agertzen den desadostasuna. Fenomeno hau sahietsi behar da zelula hauen

komertzalizaziora begira. Hainbat ikerketek adierazi duten bezala, fullerenoak histeresia gutxitzearen atzean egon daitezkeen molekulak dira, karga interfazialaren akumulazioa, karga-tranpak eta ioien migrazioa direla eta.

Azken ikerketan fullerenoen guztiz berri den aplikazio bat aurkezten da. Izan ere, hutsak eramaten duen fullereno nukleodun lehen molekula sintetizatu eta karakterizatu zen, eta huts-eroale/elektroi-blokeatzaile emaitza interesgarriekin. Fullereno-nukleoak elektroeroale izaera ezaguna du, baina aldaketa kimiko egokiekin HOMO-LUMO energia-mailak molda daitezke helburu honetarako. Garrantzitsua da adieraztea ez zirela aditiborik erabili fullereno geruzak prestatzeko. Orokorrean, aditiboen erabilera beharrezkoa da material huts-eroaleen konduktibitatea handitzeko, kasu nagusiaren kasuan bezala, spiro-OMeTAD. Hala ere, aditibo hauen gehitzea eragozpen garrantzitsu batzuk ditu, batez ere epe luzean estabilitatea gutxitzen dela. Zentzu honetan, aditiborik gabe lan egiteko aukera eskuan da. Gainera, lehen aldiz „fullerene-sandwich“ perovskita aurkezten da, non bi karga-eramaile geruzak fullereno materialak dira.

Tesi honetan fullerenoen aniztasun kimikoaz baliatu da perovskita eguzki-zelula efiziente eta iraunkorrak eskuratzeko. Ondorioz, fullerenoak eta fullereno deribatu berriak ETM, HTM edo aditibo bezala perovskita geruzan barne erabili ziren, molekula sinestezin hauen aplikazio anitzak azpimarratuz.



## Abbreviations

---

<b>a-Si</b>	Amorphous silicon solar cells
<b>ACN</b>	Acetonitrile
<b>ATR</b>	Attenuated total reflectance
<b>bw</b>	Backward
<b>CB</b>	Chlorobenzene
<b>CdTe</b>	Cadmium telluride solar cells
<b>CIGS</b>	Copper indium gallium selenide solar cells
<b>COSY</b>	Correlation spectroscopy
<b>CV</b>	Cyclic voltammetry
<b>DBU</b>	1,8-diazabicyclo[5.4.0]undec-7-ene
<b>DC</b>	Direct current
<b>DCM</b>	Dichloromethane
<b>DFT</b>	Density functional theory
<b>DMAP</b>	Dimethyl aminopyridine
<b>DMF</b>	N, N-dimethylformamide
<b>DMSO</b>	Dimethylsulfoxide
<b>DSSC</b>	Dye-sensitized solar cell
<b>EG</b>	Ethylene glycol
<b>eQE</b>	External quantum efficiency
<b>EtOAc</b>	Ethylacetate

<b>EtOH</b>	Ethanol
<b>ETL</b>	Electron transporting layer
<b>Et<sub>2</sub>O</b>	Diethyl ether
<b>ETM</b>	Electron transporting material
<b>eV</b>	Electronvolt
<b>FAI</b>	Formamidinium iodide
<b>Fc/Fc<sup>+</sup></b>	Ferrocene/Ferrocenium
<b>FE-SEM</b>	Field emission scanning electron microscopy
<b>FF</b>	Fill factor
<b>FK 209</b>	tris(2-(1 <i>H</i> -pyrazol-1-yl)-4- <i>tert</i> -butylpyridine) cobalt(III) tri[bis(trifluoromethane)sulfonimide]
<b>FTIR</b>	Fourier-Transform Infrared Spectroscopy
<b>FTO</b>	Fluorine-doped tin oxide
<b>fw</b>	Forward
<b>Hex</b>	Hexane
<b>HMDS</b>	Hexamethyl disilazane
<b>HOMO</b>	Highest occupied molecular orbital
<b>HRMS</b>	High resolution mass spectrometry
<b>HTL</b>	Hole transporting layer
<b>HTM</b>	Hole transporting material
<b>ICBA</b>	Indene-C <sub>60</sub> bisadduct
<b>IPCE</b>	Incident photon-to-current efficiency
<b>iPrOH</b>	Isopropanol
<b>IR</b>	Infrared spectroscopy
<b>ITO</b>	Indium-doped tin oxide

<b><i>J-V</i></b>	Current-voltage
<b><i>J<sub>sc</sub></i></b>	Short-circuit current
<b>LED</b>	Light-emitting diode
<b>Li-TFSI</b>	Bis(trifluoromethylsulfonyl)amine lithium salt
<b>LUMO</b>	Lowest unoccupied molecular orbital
<b>MAI</b>	Methylammonium iodide
<b>MALDI-TOF</b>	Matrix Assisted Laser Desorption Ionization Time-of-Flight
<b>MAPbI<sub>3</sub></b>	Methylammonium lead triiodide
<b>MeOH</b>	Methanol
<b>Mono c-Si</b>	Monocrystalline silicon solar cells
<b>Multi c-Si</b>	Multicrystalline silicon solar cells
<b>MPPT</b>	Maximum power point tracking
<b>NaOtBu</b>	Sodium <i>tert</i> -butoxide
<b>NEt<sub>3</sub></b>	Triethylamine
<b>NMR</b>	Nuclear magnetic resonance
<b>NHE</b>	Normal hydrogen electrode
<b>NREL</b>	National Renewable Energy Laboratory
<b><i>o</i>-DCB</b>	<i>ortho</i> -Dichlorobenzene
<b>OFET</b>	Organic field-effect transistor
<b>OPV</b>	Organic photovoltaics
<b>OSW</b>	Osteryoung squarewave
<b>PCE</b>	Power conversion efficiency
<b>PC<sub>61</sub>BM</b>	Phenyl-C <sub>61</sub> -butyric acid methyl ester
<b>PE</b>	Petroleum ether

<b>PEDOT:PSS</b>	poly(3,4-ethylenedioxythiophene) sulfonate	polystyrene
<b>PEG</b>	Polyethylene glycol	
<b>PL</b>	Photoluminescence	
<b>ppm</b>	parts per million	
<b>PSC</b>	Perovskite solar cell	
<b>PTAA</b>	Poly-triarylamine	
<b>PtBu<sub>3</sub></b>	Tri- <i>tert</i> -butyl phosphine	
<b>PV</b>	Photovoltaics	
<b>rt</b>	Room temperature	
<b>SCE</b>	Saturated calomel electrode	
<b>SEM</b>	Scanning electron microscopy	
<b>Spiro-OMeTAD</b>	2,2',7,7'-tetrakis (N,N-di- <i>p</i> -methoxyphenylamine)-9,9'-spirobifluorene	
<b>TAA</b>	Triarylamine	
<b>TBAI</b>	Tetrabutylammonium iodide	
<b>TEG</b>	Tetraethylene glycol	
<b>THF</b>	Tetrahydrofuran	
<b>TBAF</b>	Tertabutylammonium fluoride	
<b>TBAHPF</b>	Tetrabutylammonium fluoride hydrate	
<b>TBP</b>	<i>tert</i> -Butylpyridine	
<b>TCSPC</b>	Time-correlated single-photon counting	
<b>TosCl</b>	<i>p</i> -toluenesulfonyl chloride	
<b>Tol</b>	Toluene	
<b>TRPL</b>	Time-resolved photoluminescence	

<b>UV</b>	Ultraviolet
<b>V<sub>oc</sub></b>	Open-circuit voltage
<b>XPS</b>	X-ray photoelectron spectroscopy
<b>XRD</b>	X-ray diffraction



# Introduction

---

## 1.1 Solar Energy and Perovskite Solar Cells

### 1.1.1 The Importance of Renewable Energy Sources

According to The World Bank, in 2016 around 1.1 billion people had no access to any form of energy, meaning around 13% of the world population has no access to electricity.<sup>1</sup> Furthermore, since a 2017 United Nations report states that world population will approach 10 billion in year 2050,<sup>2</sup> it is glaring that stronger technologies have to be developed in order to supply the world energy demand.

Beside this, we are still facing the issue of fossil fuels. It is estimated that the world will run out of natural gas and oil in almost 50 years, while coal should last for a bit longer than a century.<sup>3</sup>

Considering these projections, the need of affordable, clean and reliable energy is quite compelling.

In year 2015, 193 countries members of United Nations signed a document, the “Agenda for Sustainable Development”, containing 17 “Sustainable Development Goals” which should serve as a guideline to improve the quality of life around the world by 2030.<sup>4</sup> Among these goals, number 7 is about affordable and clean energy. A deepening into the topic can be found in the following page.

## 7 AFFORDABLE AND CLEAN ENERGY



### Follow-up: Sustainable Development Goals

#### Goal 7

***“Ensure access to affordable, reliable, sustainable and modern energy for all”***

Main Source: <https://www.un.org/sustainabledevelopment/energy/>

The access to such energy sources is unavoidably linked to various aspects of a minimum-wealth life: having access to clean electricity sources contributes to reduce the world poverty, reducing hunger and affording safer cooking facilities. Regarding this last aspect, it is estimated that 3.8 million of people per year die because of inadequate cooking facilities.<sup>1</sup> Moreover, the more electricity is available, the better the healthcare system is, and so on: it is thus clear that energy access is directly linked to a better quality of life under multiple aspects.

Hence, the targets of Goal 7 are the following (as reported by Main Source):

- By 2030, ensure universal access to affordable, reliable and modern energy services
- By 2030, increase substantially the share of renewable energy in the global energy mix
- By 2030, double the global rate, of improvement in energy efficiency
- By 2030, enhance international cooperation to facilitate access to clean energy research and technology, including renewable energy, energy efficiency and advanced and cleaner fossil-fuel technology, and promote investment in energy infrastructure and clean energy technology
- By 2030, expand infrastructure and upgrade technology for supplying modern and sustainable energy services for all in developing countries, in particular least developed countries, small island developing States, and land-locked developing countries, in accordance with their respective programmes of support

1. <http://www.who.int/news-room/fact-sheets/detail/household-air-pollution-and-health>



### 1.1.2 The Sun as a Source of Energy

The development of solar devices has its roots in the discovery of the photovoltaic effect, i.e. the generation of electric current in some materials, when they are exposed to light.<sup>5</sup> Applying this principle specifically to sunlight is the basis of the concept of photovoltaics, which consists in the direct conversion of sunlight into electricity. After the first preparation of solar devices by Charles Fritts in 1883,<sup>6</sup> this technology underwent impressive progress. Thus, solar power is expected to be the most employed energy source in 2050.<sup>7</sup>

### 1.1.3 Solar Devices

A solar device is an electrical device that directly converts sunlight into electricity. During the last decades, many different types of solar cells have been developed with a different degree of success.

According to National Renewable Energy Laboratory (NREL), almost 84000 MW of energy were produced in 2016 globally through the use of solar panels: the vast majority of these are based on silicon, either Mono- or Multicrystalline (Figure 1.1).<sup>8</sup> The five most commercialized types of solar cells are all based on inorganic materials, and are the following:<sup>9</sup>

- Multicrystalline Silicon solar cells (Multi c-Si):<sup>10</sup> These solar devices were the first to enter the market. The production does not require highly specialized processes; hence they have a low cost of fabrication. On the other hand, the final purity of the material is not 100%, resulting in limited power

conversion efficiencies (PCEs) of around 16%. Furthermore, these cells present low heat tolerance.

- Monocrystalline Silicon solar cells (Mono c-Si):<sup>11</sup> Monocrystalline Si solar cells guarantee higher PCEs (20%) than the aforementioned Multi c-Si, due to its high purity. This implies also a greater space-efficiency than that of Multi c-Si. Unlike their multicrystalline relative, they are demonstrated to be long-lasting, retaining enough efficiency for up to 25 years. Not surprisingly, all these advantages make these cells expensive, thus cheaper Multi c-Si are still leading the market.
- Thin-film inorganic solar cells: The three most famous types of thin-film devices are amorphous Silicon, Cadmium Telluride, and Copper Indium Gallium Selenide solar cells. Even if some of these devices can reach PCEs of around 20% in small scale, their market-scale PCEs are around 15%. Due to this fact, the combined application of the three types in the market was lower than 10% in 2016.
  - Amorphous Silicon solar cells (a-Si):<sup>12</sup> Usually employed in very small devices such as pocket calculators, a-Si have a smaller lifespan and space-efficiency than both Multi c-Si and Mono c-Si. The maximum PCE reached with these cells is around 10%. These cells are considered the first belonging to thin-film technology.

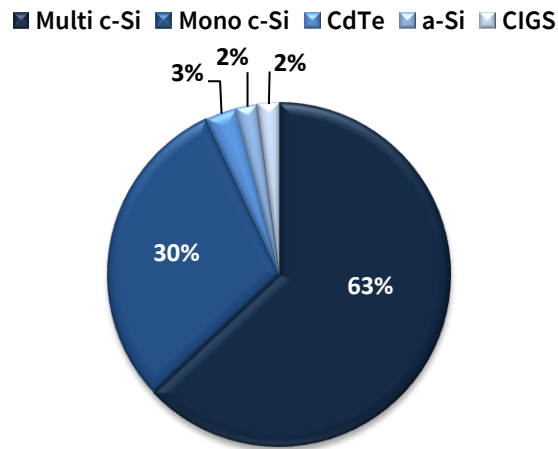


**Figure 1.1:** Global solar module production in 2016 by technology.<sup>8</sup> Multicrystalline Si devices still lead the market (53007 MW), followed by Monocrystalline Si devices (25469 MW). Thin-film technologies (Cadmium Telluride, Amorphous Silicon and Copper Indium Gallium Selenide devices) produced together 5217 MW.

- Cadmium Telluride solar cells (CdTe):<sup>13</sup> Nowadays, this is still the only kind of solar cells that is cheaper than Multi c-Si.<sup>14</sup> These devices give PCEs around 20% in laboratory scale; however their use is limited by the high toxicity of cadmium.
- Copper Indium Gallium Selenide solar cells (CIGS):<sup>15</sup> The highest PCEs of these cells exceed 20% in laboratory scale.

In addition to these solar devices, gallium arsenide technology deserves to be mentioned.<sup>16, 17</sup> A wider bandgap and a larger absorption coefficient make these devices more efficient than silicon-based thin film solar cells. However, the huge production costs and the high toxicity of arsenic keep them off the regular market, leaving

them room only when high efficiencies are needed and the application is safe, such as in space modules.

During the last decades, organic materials took hold in photovoltaic researchers' interest, giving rise to the branch of organic photovoltaics and dye-sensitized solar cells.<sup>18, 19</sup>

- Organic photovoltaics (OPV):<sup>20</sup> This technology resorts to organic polymers or small molecules in order to produce electricity from sunlight. A standard OPV device is showed in Figure 1.2.

The operation mechanism of OPV requires electron donor molecules to absorb sunlight in order to generate relatively localized excited states.<sup>21, 22</sup>

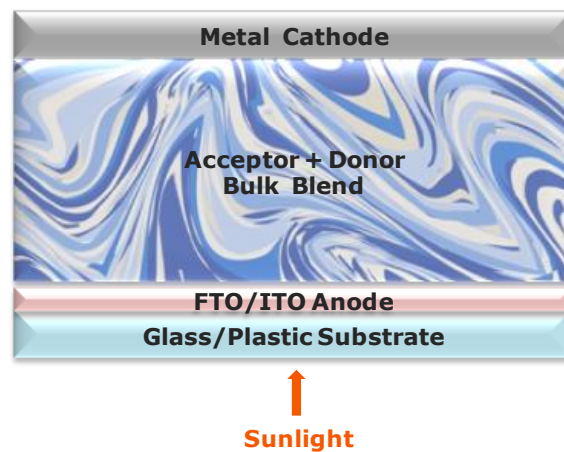


**Figure 1.2:** Schematic representation of a bulk heterojunction regular OPV device. The term “bulk heterojunction” defines the zone in which the donor and the acceptor are blended, in order to have an extremely high contact surface, in which the exciton separates into two opposite charges. FTO and ITO mean, respectively, fluorine-doped tin oxide and indium-doped tin oxide.

The generated excitons move towards the donor-acceptor interface, called p-n junction (named after the two semiconductors, the p-type donor and the n-type acceptor). Here they dissociate into positive and negative charges, which are transported towards the electrodes, where they are collected. Since the excitons have high binding energy, the dissociation takes its time: the exciton needs to reach the interface to separate into two opposite charges. The energy difference between the molecular orbitals of donor and acceptor plays a very important role in this process, and so does the ability to separate charges for their ulterior transport to reach the electrodes without recombining. For these reasons, the right choice of acceptor and donor materials is fundamental.<sup>23, 24</sup>

- Dye-sensitized solar cells (DSSC):<sup>25</sup> These devices belong to the category of thin-films solar cells. DSSC consist in a semiconductor based on a photosensitized anode and an electrolyte. A schematic representation of a DSSC can be found in Figure 1.3.

Photoexcitation of the sensitizer dye triggers the injection of an electron into the conduction band of nm-sized mesoporous particles of a semiconductor oxide, such as TiO<sub>2</sub>, ZnO or SnO<sub>2</sub>. The oxidized form of the dye is rapidly restored to the ground state by electron donation from the electrolyte reductant,

which in turn is restored by the reduction of the electrolyte oxidant at the counter electrode.

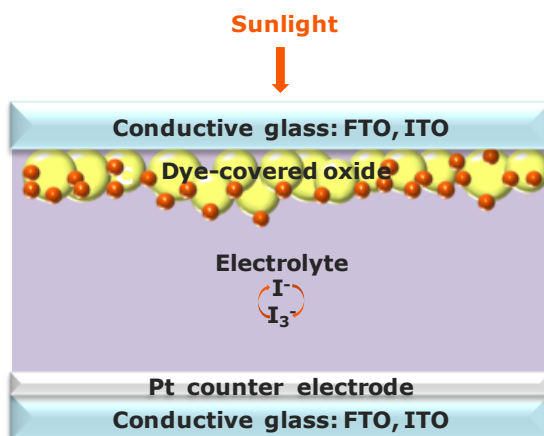


**Figure 1.3:** Schematic representation of a dye-sensitized solar cell. The yellow dots represent the nanoporous semiconductor oxide, covered with the dye (orange dots).

The voltage generated by the cell strongly depends on the difference between the Fermi level of the oxide and the redox potential of the electrolyte.

The interest raised by these two kinds of solar cells slipped partially with the discovery of a new kind of solar cells: hybrid organic-inorganic perovskite solar cells.

#### 1.1.4 Hybrid Organic–Inorganic Perovskite Solar Cells

When the first papers about hybrid organic-inorganic perovskite solar cells (PSCs) were published, surely the authors did not expect the impressive impact they were going to have over the scientific community.<sup>26, 27</sup>

Instead, the interest raised by this new all-solid-state technology was so huge that the PCE of these solar cells rose from below 10% to an

amazing 23.7% in just a few years, as reported in the NREL efficiency chart.<sup>28</sup> With this new certified PCE, PSCs surpassed CIGS solar cells.

#### 1.1.4.1 Perovskite Crystal Structure

The term “perovskite” refers to a large family of compounds which have in common a peculiar crystal structure. In the ideal form, the crystal structure of cubic  $ABX_3$  perovskite can be described as a corner-sharing  $BX_6$  octahedra with the A cation lying the coordination site formed in the middle of the cube of eight of these octahedral (Figure 1.4, left). In nature, the most common mineral presenting this structure is  $CaTiO_3$ . Mainly, perovskite-structured compounds are all-inorganic; however, there are also a few organic-inorganic hybrid structures that in the past few years gained huge attention thanks to their application in solar devices. In these hybrid structures,  $ABX_3$  is usually of the kind  $CH_3NH_3PbI_3$  ( $MAPbI_3$ ) for which A is an organic methylammonium cation and B represents lead.

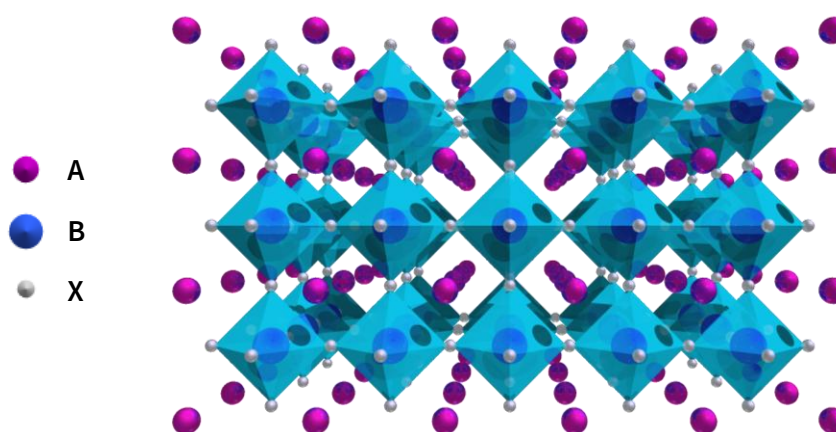


**Figure 1.4:** Crystal structure typical of perovskite, where A stands for the organic cation in hybrid perovskite and for  $Ca^{2+}$  in the standard  $CaTiO_3$ , B stands for the bivalent cation (usually  $Pb^{2+}$ ) in hybrid perovskite and for  $Ti^{4+}$  in  $CaTiO_3$ , and X stands for the halogen in hybrid perovskite and for oxygen in  $CaTiO_3$ .

#### 1.1.4.2 The Beginning of Hybrid PSCs

The first study about organic–inorganic hybrid perovskite solar cells was reported in 2009.<sup>29</sup> Miyasaka and co-workers sensitized TiO<sub>2</sub> nanoparticles with perovskite as a dye: the role of organic–inorganic hybrid perovskite in solar cells starts in a DSSC. Even if promising, this novelty presented a drawback which could not be left aside; in fact, perovskite crystals dissolved in the electrolyte liquid phase.

The main breakthrough in hybrid perovskite history came in 2012, when Grätzel, Park, and co-workers<sup>26</sup> and Snaith and co-workers,<sup>27</sup> almost at the same time, used MAPbI<sub>3</sub> as a light harvester in an all-solid state PSC with 2,2',7,7'-Tetrakis[N,N-di(4-methoxyphenyl)amino]-9,9'-spirobifluorene as hole transporting material (HTM). The former group, using mesoporous TiO<sub>2</sub> as electron transporting layer, obtained a then impressive PCE of 9.7%. Since then, countless modifications have been introduced in order to get the best performing, long lasting PSC.

#### 1.1.4.3 Architecture of PSCs

Each one of the PSCs that have been prepared since the first example is structured according to a few basic architectures, which are depicted in Figure 1.5.

The most commonly used structure starts with a transparent and conductive fluorine-doped tin oxide (FTO) treated glass (Figure 1.5.A). Compact TiO<sub>2</sub> is deposited on it; this serves both as selective electron transporting layer (ETL) and an efficient hole blocking layer.



Similarly to DSSCs, there is a mesoporous  $\text{TiO}_2$  layer in which the perovskite partially infiltrates. The perovskite is covered with a hole transporting material (HTM), on which a gold top electrode is deposited. When the conductive mesoporous  $\text{TiO}_2$  layer was replaced by insulating mesoporous  $\text{Al}_2\text{O}_3$ , the perovskite demonstrated to be capable of light harvesting and electron transport.<sup>27</sup> Besides its ability to act as electron transporting material (ETM), perovskite previously showed its capability to act as HTM in solid-state DSSC.<sup>30</sup>

The ambipolar charge transport nature of this material is demonstrated as charge transport lengths up to 1 mm have been reported.<sup>31,32</sup>

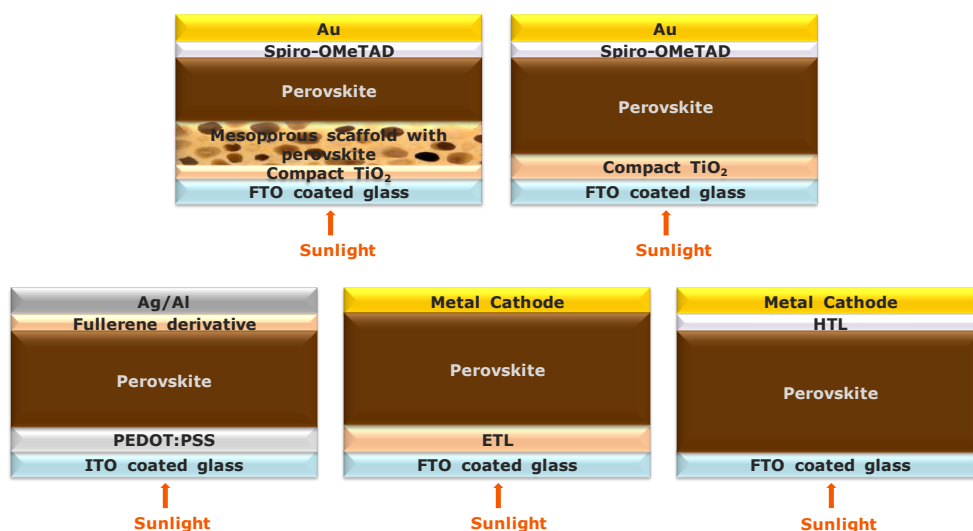


**Figure 1.5:** Different PSC architecture depicted bearing their most common components. A) Regular mesoporous PSC, with conducting meso- $\text{TiO}_2$  scaffold and Spiro-OMeTAD as HTM. B) Regular compact PSC, with no scaffold and compact  $\text{TiO}_2$  as ETM. In this configuration,  $\text{TiO}_2$  is commonly replaced with tin oxide.<sup>33</sup> C) Inverted PSC, with PEDOT:PSS as HTM and a fullerene derivative, usually  $\text{PC}_{61}\text{BM}$ , as ETM. D) HTL-free PSC. E) ETL-free PSC.

These features imply that the use of a conducting mesoporous scaffold is not essential. Thus, planar PSCs are also frequently reported, in which the perovskite is deposited directly on the compact TiO<sub>2</sub> (Figure 1.5.B).<sup>34</sup>

The aforementioned architectures are referred to as “regular”, i.e. those cells whose architectures follow the scheme FTO glass/ETL/perovskite/HTL/Au.

An “inverted” architecture has also been presented (Figure 1.5.C).<sup>35</sup> Recently, this configuration has overcome the 20% PCE barrier.<sup>36</sup> In this architecture, commonly FTO/glass is replaced by indium tin oxide (ITO) coated glass as bottom electrode. This configuration follows the scheme ITO glass/HTL/perovskite/ETL/Top electrode. The hole transporting and electron blocking material used as reference is, in this case, the polymer poly(3,4-ethylenedioxythiophene) polystyrene sulfonate (PEDOT:PSS). The perovskite is deposited on the top of this layer. To guarantee selective electron transport and hole blocking, an ETM (commonly a fullerene derivative) is deposited on top of the perovskite. The device is completed with an aluminium or silver top electrode.

The astonishing ability of perovskite of transporting both holes and electrons was the driving force towards HTL- or ETL-free regular solar cells (1.5.D and 1.5.E).<sup>37-40</sup> In both cases, the aim is simplifying the multi-step device preparation in order to optimize the costs and timing of device preparation.

#### 1.1.4.4 Working principles of PSCs

Since their first application was in a DSSC,<sup>29</sup> perovskites were included in this category of solar devices. Soon afterwards it was evident that something peculiar was occurring in these devices under working conditions. In one of the first papers facing this issue, Mora-Seró, Park and co-workers observed charge accumulation in the light-harvesting material MAPbI<sub>3</sub>, thus indicating that perovskite solar cells indeed constitute a new kind of solar device.<sup>41</sup>

In a subsequent work, the exciton binding energy of the MAPbI<sub>3-x</sub>Cl<sub>x</sub> perovskite crystal was estimated to be approximately 50 meV, which almost corresponds to full ionization energy when operating under conditions which are comparable to those of Si-based solar cells.<sup>42</sup> Therefore, the interfaces between perovskite material and both hole- and electron-transporting materials only assist charge extraction but do not contribute to charge separation.

Afterwards, the previously reported static dielectric constant of MAPbI<sub>3</sub> perovskite was demonstrated to have been underestimated.<sup>43</sup> This led to the estimation of an even lower exciton binding energy of roughly 2 meV. These results confirmed the non-excitonic nature of hybrid perovskite solar cells.

This was further demonstrated by successive works: Ng, Lee and co-workers found out that perovskite solar cells with fullerene C<sub>60</sub> as ETM are comparable to a n-n junction, different from the p-n junction typical for OPVs.<sup>44</sup> This means that the perovskite/fullerene interface does not provide enough driving force for an exciton to dissociate

into free charges. Hence, these devices are efficient due to the rapid charge dissociation which instantly produces free carriers within the perovskite film.

This almost non-excitonic nature is highly desirable for the development of high-performance devices. In fact, the efficient one-step generation of free charges might be considered one of the main advantages of perovskite solar cells. However, this feature is not free from drawbacks: during the several working steps (i.e. exciton dissociation, charge transport, and charge collection) the device might undergo significant losses in energy.

To sum up, after excitation of the light-harvesting perovskite, the electrons are extracted at the ETL/perovskite interface and are transported towards the FTO electrode. On the other side, the formed holes are extracted at the perovskite/HTM interface, with subsequent transport towards the gold electrode.<sup>45</sup>

#### 1.1.4.5 Perovskite's Sidekicks: Charge Transporting Layers

The choice of proper charge transporting layers is fundamental for a PSC to be efficient. Countless HTMs and a few ETMs have been tried these last few years.<sup>46-50</sup> All of these should fulfil some precise requirements in order to be a suitable candidate for PSCs.

- **Electron transporting layer:** An ideal ETL should promote electron transport and block holes, in order to avoid charge recombination. To enhance electron mobility towards the FTO anode, the lowest unoccupied molecular orbital (LUMO) level

of the ETM should be energetically lower than the conduction band of the perovskite. (Figure 1.6) On the other hand, to block hole transport the highest occupied molecular orbital (HOMO) level of the ideal ETM should be lower than the valence band of the perovskite. The conduction and valence bands of the well-known MAPbI<sub>3</sub> are, respectively, -3.9 eV (LUMO) and -5.4 eV (HOMO).<sup>51</sup> There are some examples in literature in which these requirements are not fulfilled. In these cases, a strong balance between an enhancement in electron transport and the hole-blocking activity results in acceptable performances of the devices.<sup>52</sup>

As mentioned above, TiO<sub>2</sub> has been the most exploited material for application in PSCs with regular configuration (Figure 1.5.A and 1.5.B). However, TiO<sub>2</sub> displays also some drawbacks, such as its degradation under UV irradiation.<sup>53</sup> Furthermore, the high temperature needed for the annealing process makes the procedure rather complex and unsuitable for low-cost production and for the fabrication of flexible substrates.<sup>27</sup> For these reasons, an alternative to TiO<sub>2</sub> is highly desired for cheaper, long-lasting, high-scale PSCs, that could gain a foothold in the PV market.<sup>54</sup>

- **Hole transporting layer:** The role of HTL is to enhance hole extraction from the light-harvesting perovskite material, and transport the charges towards the metal cathode, avoiding charge recombination by blocking electrons.

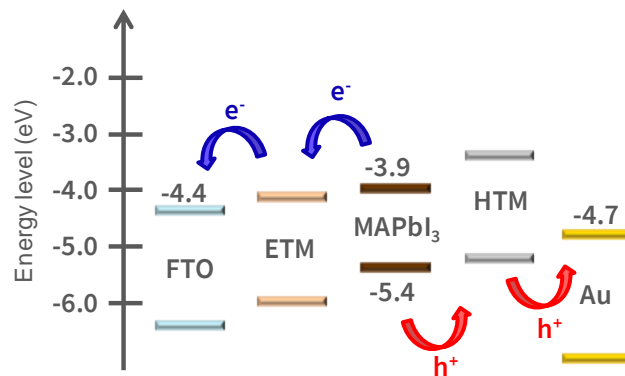


Figure 1.6: Energy levels of the several layers of a PSC.

The energy levels of the HTM have to be adjusted both to the bands of the perovskite material and to the energy levels of the cathode (Figure 1.6). Together with the generation of a sufficient driving force for hole extraction, the layer is also required to obtain a high output voltage of the solar cell. The open-circuit voltage ( $V_{oc}$ ) depends on the energy difference of the quasi-Fermi levels of the electrons in  $TiO_2$  and the HOMO level of the HTM.<sup>55</sup> To maximize this value, the HOMO energy of the HTM should be similar to the energy level of the valence band of the perovskite, but slightly higher in order to achieve the driving force required for hole extraction.

The reference HTM, Spiro-OMeTAD, has low conductivity and hole mobility by itself, thus the use of additives referred to as dopants is required in order to improve charge mobility to achieve good photovoltaic performances.<sup>56</sup> The most used dopants are tert-butylpyridine (tBP), bis(trifluoromethanesulfonyl)imide lithium salt (LiTFSI), and

tris(2-(1*H*-pyrazol-1-yl)-4-*tert*-butylpyridine)cobalt(III) tri[bis(trifluoromethane)sulfonimide] (FK209).<sup>57</sup> The use of these doping agents presents indeed several drawbacks that affect photovoltaic performances of PSCs. First of all, these dopants are hygroscopic and they might migrate into the perovskite layer during operation, leading to important losses in performance.<sup>58, 59</sup> Furthermore, LiTFSI and FK209 are added to the HTM solution dissolved in acetonitrile, which is known to dissolve perovskite, thus it could partially degrade the light-harvesting layer.

For these reasons, it is convenient to find a HTM that could work properly even without dopants. Moreover, removing the steps of the dopant preparation and addition, the number of steps required to prepare a PSC would be reduced, leading to diminished expenses in terms of time and money.

Another important feature of an optimal HTM involves its light-harvesting properties. If it superimposes that of perovskite, the undesired phenomenon of “parasitic light absorption” has been reported to occur.<sup>60</sup> When it takes place, the HTM subtracts part of the light from the perovskite, leading to lower performances. On the other hand, it is beneficial for the HTM to be able to absorb either in the ultraviolet (UV) region or up to the near-infrared (near-IR) in which the perovskite displays lower light-harvesting properties, so that a wider portion of the light spectrum can be

absorbed by the device and converted into electricity once the generated exciton reach the perovskite layer and dissociates into charges, subsequently transported towards the electrodes.

#### 1.1.4.6 The Issue of Hysteresis

Hysteresis causes a discrepancy between the cell performances when they are measured either backwards (from a definite voltage value to zero) or forwards (from zero to a definite voltage value) and results in an inaccurate efficiency measurement when this is extracted from a current density–voltage ( $J$ – $V$ ) curve (Figure 1.7).<sup>61–64</sup> Thus, this phenomenon should be avoided prior to the commercialization of PSCs. Hysteresis seems to be the consequence of three major effects: charge accumulation at the interfaces, charge traps, and migration of ions.

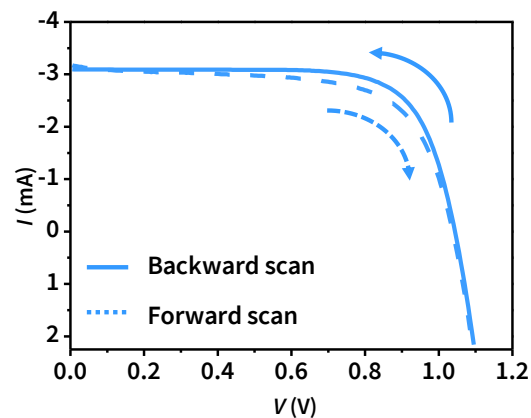


**Figure 1.7:** The hysteresis is defined as the discrepancy between the performances registered with a backward scan (solid line) and the forward scan (dashed line).



#### 1.1.4.7 Stability of Perovskite Solar Cells

To be ready to commercialization, PSCs have to meet several requirements:

- **Efficiency:** a new solar technology should equate or overcome the performances of the market leaders, i.e. silicon solar cells. As mentioned above, the efficiency of PSCs is already good enough for the purpose.
- **Cost:** the total price of the new cells should be low enough to be competitive with current market price of Si-based solar cells. Several analysis demonstrated that PSCs fulfil also this requirement.<sup>65</sup>
- **Stability:** in principle, the devices should be stable enough to guarantee a long-term functioning, in order to amortize the preparation and installation costs.

Nowadays, this remains the weakest spot of perovskite solar cells.<sup>66</sup>

Thus, for the PSCs to be commercialized the research efforts should be focused on the improvement of stability.

The factors that affect perovskite stability are various:<sup>67</sup>

- **Temperature:** When heated at temperatures higher than 150°C, perovskite undergoes an endothermic reaction that decomposes it into its precursors  $\text{PbI}_2$ ,  $\text{CH}_3\text{NH}_2$ , and  $\text{HI}$ .<sup>68</sup> At such high temperatures, both methylamine and hydriodic acid are volatile; hence this degradation mechanism is irreversible.

- UV-irradiation: Under irradiation,  $\text{TiO}_2$  oxidizes iodide into iodine, leading to a decomposition of the crystal structure.<sup>69-71</sup> Similarly to the previous, this process also results in the formation and subsequent removal of methylamine and hydriodic acid.
- Oxygen: Upon photoexcitation, perovskite can lose an electron in favour of oxygen, with the formation of the superoxide ion  $\text{O}_2^-$ .<sup>72</sup> This ultimately leads to the formation of the aforementioned volatile compounds.
- Moisture: When exposed to humidity,  $\text{MAPbI}_3$  tends to decompose into methylammonium iodide (MAI) and lead(II) iodide ( $\text{PbI}_2$ ), which are its precursors.<sup>73</sup> According to the proposed mechanism, a molecule of water, acting as a Lewis base, coordinates to the ammonium proton initiating the degradation process. Thus, a plausible solution to overcome this issue would be the use of chemical strategies to prevent the water molecules to get close to the perovskite or to get them bound by coordination to non-perovskite moieties.

#### 1.1.4.8 Fullerenes: a Possible Solution for PSCs' Issues

As it will be thoroughly discussed in the next section, the research community has resorted multiple times to fullerenes to address the major issues of PSCs, i.e. hysteresis<sup>74</sup> and stability,<sup>75</sup> and to replace the charge transporting layers.<sup>76</sup>

## 1.2 Fullerenes in Perovskite Solar Cells

### 1.2.1 Fullerenes: an Introduction

There is no aspect regarding fullerene history that lacks of appeal. Even the discovery of this Nobel-worthy molecule (depicted in figure 1.8) happened under interesting circumstances.

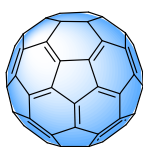


**Figure 1.8:** Structure of C<sub>60</sub>.

Since the moment of its discovery in 1985, C<sub>60</sub> has been subject of several studies thanks to and about its unique features. In fact, due to its peculiar structure, this astonishing molecule can accept and transfer electrons,<sup>77-81</sup> it is able to accommodate inside the hollow cage small structures such as metals (endohedral fullerenes),<sup>82, 83</sup> and can be functionalized on the surface through several reactions to get derivatives with a wide range of potential applications.<sup>84-87</sup>

Doubtlessly, the field in which fullerenes have demonstrated the highest versatility and appeal is photovoltaics.<sup>50</sup> Being able to transfer electron in such an efficient way might be the most remarkable feature of fullerenes: the charge mobility of C<sub>60</sub> and its derivatives is generally of the order of  $10^{-4}$ - $10^{-3}$  cm<sup>2</sup> V<sup>-1</sup> s<sup>-1</sup> in film.<sup>88</sup>

Theoretical studies have tried to better explain this feature, which may be ascribable to the singular hybridization of the carbon atoms of the C<sub>60</sub>.<sup>77</sup> Due to the curvature imposed by its closed shape, C<sub>60</sub> presents a hybridization which is thought to be a mixture of *sp*<sup>2</sup>, typical of graphite, and *sp*<sup>3</sup>, typical of diamond.



### Follow-up: The Discovery of $C_{60}$

From left to right, Sean O'Brien, Richard Smalley, Robert Curl, Harold Kroto, and James Heath pose with their models and a real football in front of the buildings of Rice University of Houston (TX).

Main Source: H. Aldersey-Williams, *The Most Beautiful Molecule-The Discovery of the Buckyball*, John Wiley & Sons, Inc., 1995.

Early in 1966, David Jones, under the pseudonym of Daedalus, so wrote: "The high-temperature graphite production might be modified to generate graphite balloons".<sup>1, 2</sup> Four years later, Eiji Osawa reported his conjecture on the existence of a  $C_{60}$  molecule, whose structure had the symmetry of a modern football.<sup>3</sup>

The final step of the fullerene discovery took place at Rice University of Houston, TX. Smalley, Curl, Kroto, and the students Yuan Liu, Sean O'Brien, and James Heath, together in the laboratory of the former, put an end to the years-long search for the  $C_{60}$  molecule, giving start to a new whole field of research.

By laser-irradiating rotating graphite rods, the group observed intense mass peaks at 720 a.m.u., corresponding to 60 carbon atoms, together with a less intense peak at 840 a.m.u. ( $C_{70}$ ). Curiously, one of the most important discoveries of the 20<sup>th</sup> century was close to not occurring. While running some preliminary experiments, in fact, the scientists focused their attention on a substantially lower range of the mass spectrum, in order to find what they were expecting, namely smaller clusters.

At first, the group speculated that what they found was just a cluster of graphite layers, then both Kroto and Smalley remembered 1967's EXPO and the Geodesic Dome, a hemispherical structure apparently entirely made of hexagons. The group was so amazed by the idea that the members started to independently build their own models: first Heath with toothpicks and gummy bears, then Smalley with paper shapes. Both the scientists first failed in the purpose, finding the construction of an all-hexagon sphere impossible. Finally, Smalley accepted Kroto's speculation about pentagons being part of the closed structure, and there it was. So, after many hypotheses concerning the most probable structure, on September 9th, 1985 the group finally agreed and ascribed to this molecule a football-like spherical structure, which was the only one that could satisfy all the valences.



The geodesic dome as designed by Richard Buckminster Fuller for the 1967 Montreal EXPO.

The research was rapidly submitted to *Nature*, together with Smalley's cover letter requesting "rapid publication as a letter [...] so that it reaches the widest possible scientific audience". The paper was published five weeks later.<sup>4</sup>

Afterwards, a dispute arose between Smalley and Kroto over who was the actual discoverer. The two scientists' respective points of view are explained in two catchy articles.<sup>5, 6</sup>

Alongside with this fight, the two scientists also disagreed over who came up with the name Buckminsterfullerene, or Fullerene (in honour of Richard Buckminster Fuller, designer of the aforementioned geodesic dome). In an interview with Dr. Cyrus Mody, Robert Curl states "Harry was convinced that [it] was his idea and Rick was convinced it was his idea and I'm convinced it wasn't my idea".<sup>7</sup>

Nevertheless, this amazing finding earned their discoverers the Nobel Prize of Chemistry for the year 1996.<sup>8</sup>

The three laureates receiving their prize.  
From left to right, Kroto, Curl, and Smalley



Stamp dedicated to R. Buckminster Fuller and his geodesic dome

1. D. E. H. Jones, *New Scientist*, **1966**, 245.
2. D. E. H. Jones, *The Inventions of Daedalus*, Freeman: Oxford, **1982**.
3. E. Osawa, *Superaromaticity*, Kagaku, **1970**, 854-863.
4. H. W. Kroto, J. R. Heath, S. C. O'Brien, R. F. Curl, and R. E. Smalley, *Nature*, **1985**, 318, 162-163
5. H. W. Kroto, *Angewandte Chemie International Edition*, **1992**, 31, 111-129.
6. R. E. Smalley, *The Sciences*, **1991**, 31, 22-28.
7. E. M. Speller, *Materials Science and Technology*, **2016**, 33, 924-933
8. The Nobel Prize in Chemistry, [https://www.nobelprize.org/nobel\\_prizes/chemistry/laureates/1996](https://www.nobelprize.org/nobel_prizes/chemistry/laureates/1996)

This intermediate nature makes the fullerene hybridization fluctuate between the two states. Rehybridization seems to play a fundamental role in the electronic structure and thus in the electron-accepting ability of the C<sub>60</sub> cage. In addition, fullerenes have low reorganization energy and demonstrated to be able to delay charge recombination in the dark.<sup>89</sup>

Moreover, studies have led to the conclusion that fullerenes can actually limit the aforementioned causes of hysteresis.<sup>88</sup> In the first paper linking fullerenes and hysteresis suppression in PSCs, Sargent and co-workers discovered that PC<sub>61</sub>BM, a C<sub>60</sub> derivative that will be better described in next section, was able to bond with Pb–I antisite defects, hence suppressing trap states occurring on the surface of grain boundaries.<sup>74</sup> These are also the preferential channels for ion migration, thought to be another cause of hysteresis. In the same work, it is showed how fullerenes are able to fill these boundaries, hence blocking these channels.

Thanks to all these unique properties, C<sub>60</sub> and other fullerenes have been extensively used in photovoltaics, both in their pristine and functionalized forms.<sup>23, 89-94</sup>

Fullerenes were first introduced into PSCs by Jeng and co-workers, who obtained a PCE of 3.9% with their planar, inverted device.<sup>35</sup> Later, Snaith and co-workers successfully replaced TiO<sub>2</sub> with a C<sub>60</sub> layer as ETL.<sup>76</sup> The benefits of using fullerene instead of TiO<sub>2</sub> mostly regard the low processing temperature. This is necessary for an application of perovskite in flexible cells and to reduce manufacturing costs.<sup>95</sup>

Together with their use as ETMs, it is also important to consider the role of fullerenes as additives incorporated into the perovskite layer. Mostly, these additives have the purpose of improve stability<sup>75</sup> or morphology,<sup>96</sup> or reducing hysteresis.<sup>74</sup>

Last but not least, fullerene derivatives were just recently employed as HTM in PSCs with good efficiencies.<sup>97</sup> This will be further discussed in chapter 3.3.

### 1.2.2 Fullerenes as Charge Transporting Materials in PSCs

The most famous fullerene derivative used in solar cells is Phenyl-C<sub>61</sub>-butyric acid methyl ester (**PC<sub>61</sub>BM**, Figure 1.9).<sup>98</sup> First synthesized in 1995 by the group of Prof. Fred Wudl, at the end of the same year **PC<sub>61</sub>BM** was first employed in a polymer solar cell.<sup>99</sup>

**PC<sub>61</sub>BM** has the tendency to create a charge-transporting network thanks to the phenyl moiety, which is inclined to undergo  $\pi$ - $\pi$  stacking with other **PC<sub>61</sub>BM** molecules. Since this pioneering work, **PC<sub>61</sub>BM** has been

employed in numerous studies concerning OPVs.<sup>100, 101</sup>

Given the interesting results in the field of OPV, **PC<sub>61</sub>BM** was thoroughly investigated for its application in PSCs, becoming the most famous organic ETM for this kind of solar cells as well.<sup>50, 91</sup> The HOMO and LUMO levels of **PC<sub>61</sub>BM**, which are -5.9 eV and -3.9 eV respectively, make it suitable for extracting electrons and blocking holes coming from methylammonium lead iodide, whose valence and conduction bands are, respectively, -5.4 eV and -3.9 eV.<sup>102</sup> For these

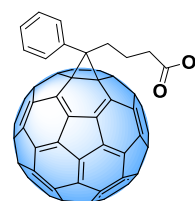


Figure 1.9: Structure of **PC<sub>61</sub>BM**

reasons, PC<sub>61</sub>BM has been often used in inverted PSCs to achieve remarkable power conversion efficiencies.<sup>103-105</sup>

However, PC<sub>61</sub>BM is not flawless. The films made using this molecule are often too thin to completely cover the perovskite, due to the small molecule nature of PC<sub>61</sub>BM and the low viscosity of the PC<sub>61</sub>BM solution.<sup>106</sup> In order to reach the perfect equilibrium between the film morphology and the electron transporting ability, PC<sub>61</sub>BM layer should be thin enough to ensure an efficient electron transport, together with suppressed charge recombination and low series resistance. Additionally, the film should be rather continuous as well.

To bypass this problem, researchers tried several routes. For example, one of the most common strategies is to add other molecules to the ETL, thus doping the PC<sub>61</sub>BM layer.<sup>107-113</sup> Another strategy involves a solvent annealing process, through which Huang and co-workers managed to increase the PCE of their cells from 17.1 to 19.4%.<sup>114</sup>

This improvement is directly linked to the decrease of the energy disorder in the ETL, which leads to an increased  $V_{OC}$  without affecting short-circuit current ( $J_{sc}$ ) and fill factor (FF).

Due to its success, PC<sub>61</sub>BM was extensively modified in order to get the best possible performances. For example, PC<sub>71</sub>BM was used several times as ETM in PSCs, giving remarkable results.<sup>115, 116</sup>

Together with PC<sub>61</sub>BM, another widely used fullerene derivative is Indene-C<sub>60</sub> bisadduct (IC<sub>60</sub>BA, Figure 1.10), first synthesized in 1997 through a Diels-Alder reaction<sup>117</sup> and successfully incorporated into



OPV device several years later.<sup>118</sup> However, when introduced into PSCs, **IC<sub>60</sub>BA** presented higher hysteresis than C<sub>60</sub> reference and **PC<sub>61</sub>BM**.<sup>119, 120</sup>

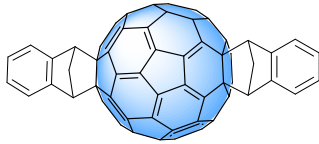


**Figure 1.10:** Structure of **IC<sub>60</sub>BA**

In principle, pristine C<sub>60</sub> would be a better ETM than **PC<sub>61</sub>BM**, thanks to its higher electron mobility, which is correlated to the resulting device performance.<sup>121</sup>

Unfortunately, its use is limited by its scarce processability. Nonetheless, there are several studies in which this carbon allotrope was used as ETL in PSCs. For example, Snaith and co-workers successfully deposited a C<sub>60</sub> layer on FTO/glass, in order to replace TiO<sub>2</sub>.<sup>76</sup> The ETL was deposited either by solution or vapor techniques. Through spectroscopic characterization, it was possible to notice the improvement in the electron extraction, with respect to what happens using TiO<sub>2</sub>, observing significant speeding up of the photoluminescence (PL) decay. The devices prepared by the group presented good performances, supported by low hysteresis. Moreover, a stability test showed good long-term performances of the C<sub>60</sub>-containing devices.

Furthermore, a study from our research group confirmed the good performances of C<sub>60</sub> as ETL, and C<sub>70</sub> was first introduced as ETL for regular PSCs.<sup>122</sup> This work will be extensively explained in chapter 3.1. Together with the most famous, aforementioned derivatives, other C<sub>60</sub> derivatives have been successfully used as ETLs in PSCs, leading to new interesting findings.<sup>90, 123-128</sup>

For example, Loi and coworkers incorporated a novel C<sub>60</sub> derivative bearing an hydrophilic oligoethylene glycol chain (**PTEG-1**, Figure 1.11) in a PSC, getting better results than those obtained with the **PC<sub>61</sub>BM** reference.<sup>129</sup> In fact, the performance increased from 11.8% to 13.1% with the use of the new derivative, which reached 16.1% after optimization. Through this derivative, the group investigated how the light-soaking effect is linked to the dielectric constant of the material.

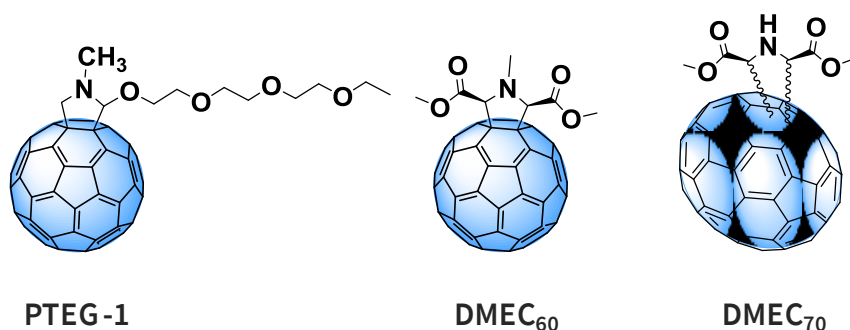


**Figure 1.11:** Structure of **PTEG-1**,<sup>129</sup> **DMEC<sub>60</sub>**, and **DMEC<sub>70</sub>**.<sup>130</sup>

This effect can be noticed when, after exposition to light, the efficiency of the device increases significantly. The higher dielectric constant of the novel derivative (5.9 with respect to 3.9 of **PC<sub>61</sub>BM**) seems to be linked to a reduction of the surface trap states concentration, leading to a lower light-soaking effect. The higher-constant derivative helps screening the recombination otherwise occurring in the extraction layer. As a consequence, the efficiency of **PTEG-1**-containing cells is more stable throughout the measurements.<sup>131</sup>

Two easy to prepare, cheap fulleropyrrolidinic derivatives of C<sub>60</sub> and C<sub>70</sub> (**DMEC<sub>60</sub>** and **DMEC<sub>70</sub>**, Figure 1.11) were used by Echegoyen and co-workers in inverted perovskite devices and compared to the

corresponding **PC<sub>61</sub>BM**, overcoming their performances in each case.<sup>130</sup> In fact, **DMEC<sub>60</sub>** and **DMEC<sub>70</sub>** yielded PCEs of 15.2% and 16.4% respectively, while the corresponding PCBM yielded 14.5% (**PC<sub>61</sub>BM**) and 15.1% (**PC<sub>71</sub>BM**). Several factors lie behind these results: more suitable energy levels, better electron mobility and charge extraction ability with respect to the PCBMs, thanks to favourable interactions between the perovskite structure and the new derivatives. Moreover, the pyrrolidine moieties make the molecule more hydrophobic, thus prone to rejecting water, with positive effects on the stability of the devices. Furthermore, all these great features make the layers strong enough to delay the migration of the metal contact into the light-harvesting layer.

In general, fullerene and its derivatives are considered for their ability to act as ETMs, and until very recently the contrary would have been considered weird. Nonetheless, a hole transporting fullerene hexakisadduct was successfully prepared and incorporated into PSCs.<sup>97</sup> This would be further discussed in chapter 3.3.

### 1.2.3 Fullerenes as Additives for PSCs

Another way to take advantage of the properties of the fullerenes is to incorporate them into the perovskite layer.<sup>132-135</sup>

Fan, Mai, and co-workers recently introduced C<sub>60</sub> in their PSCs, observing not only the passivation of the interfaces and reduction of the pinholes in perovskite, but also a protective action against moisture and oxygen from ambient atmosphere.<sup>136</sup> The interfacial passivation

increased the bulk and surface recombination lifetimes and decreased the charge trap-state density.

**PC<sub>61</sub>BM** plays an important role as an additive as well.<sup>96, 133, 137, 138</sup> Apparently, the presence of **PC<sub>61</sub>BM** close to perovskite grain boundaries makes a significant impact on the morphology, the electronic properties, the stability, and the hysteresis.

An interesting way to employ fullerenes as additives is presented by Dennis, Wang, Bi, Grätzel, and co-workers, which dissolved both **PC<sub>61</sub>BM** and  **$\alpha$ -bis-PCBM** (equatorial bisadduct) in the so-called “antisolvent”, a solvent that cannot attack perovskite, like chlorobenzene.<sup>96</sup>

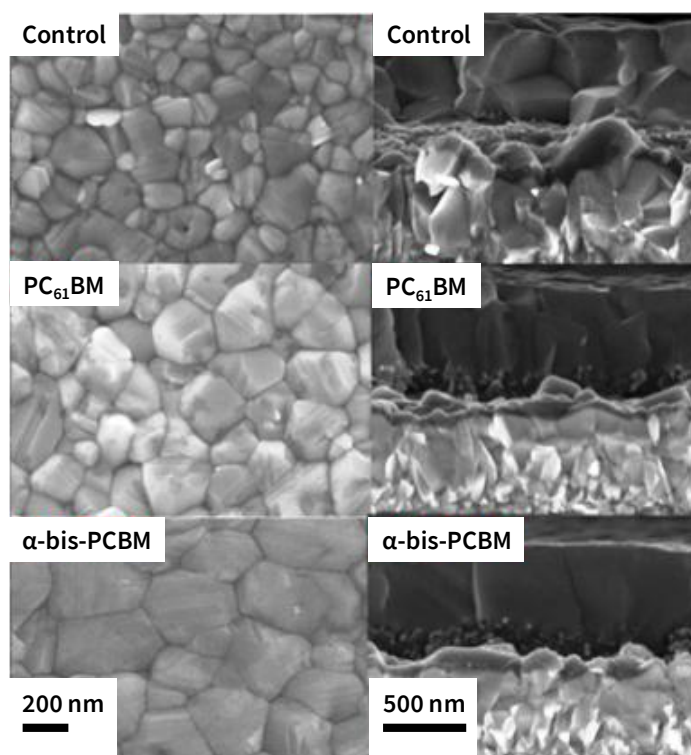


**Figure 1.12** SEM images: Top view (left) and cross section (right) of, from above to below, perovskite reference, perovskite treated with **PC<sub>61</sub>BM**-containing antisolvent, and perovskite treated with  **$\alpha$ -bis-PCBM**-containing antisolvent.

The antisolvent is dripped on the perovskite during the spin-coating deposition in order to improve the crystallization thanks to repulsive forces.<sup>139</sup> The group reported that  **$\alpha$ -bis-PCBM** creates a hydrophobic network which resists moisture incursion, thus preventing erosion of the perovskite, and passivating the voids or pinholes generated.  **$\alpha$ -bis-PCBM** also displayed higher electron extraction efficiency with respect to **PCBM**, and allowed better crystallization of perovskite. The considerably better films obtained through this technique are shown in Figure 1.12.

By incorporating fullerenes into the perovskite, the so-called “Fullerene Saturation Approach” was developed.<sup>122</sup> This strategy, whose main goal was to allow processing perovskite onto soluble ETLs, will be better explained in chapter 3.1 of this thesis.

This strategy led also to the preparation of ETL-free PSCs, incorporating pristine  $C_{70}$  directly into the perovskite.<sup>39, 140</sup> These cells were compared to both a regular planar PSC, with  $TiO_2$  as ETL, and an ETL-free solar cell without fullerene. In general, ETL-free solar cells presented reduced transport resistance, due to the absence of the ETL. Furthermore, comparing the two kinds of ETL-free solar cells, the  $C_{70}$ -containing cell presented significantly decreased recombination rate, probably due to the well-known passivating effect of the fullerene cage, which lowers the opportunities of recombination.<sup>141</sup> Moreover, the  $C_{70}$ -containing cells presented enhanced photostability, even if they were not encapsulated.

On the wave of these promising results, two isoxazolinofullerenes (**IS-1** and **IS-2**, Figure 1.13) and two pyrazolinofullerenes (**PI-1** and **PI-2**, Figure 1.13) were tried in the same cell configuration.<sup>142</sup> The results obtained with these molecules exceed in every case those obtained with both the fullerene-free reference and the **PC<sub>61</sub>BM** containing one. A remarkable result was obtained with fullerene **IS-2** containing devices, whose average PCE is 33% higher than that of the fullerene-free devices.

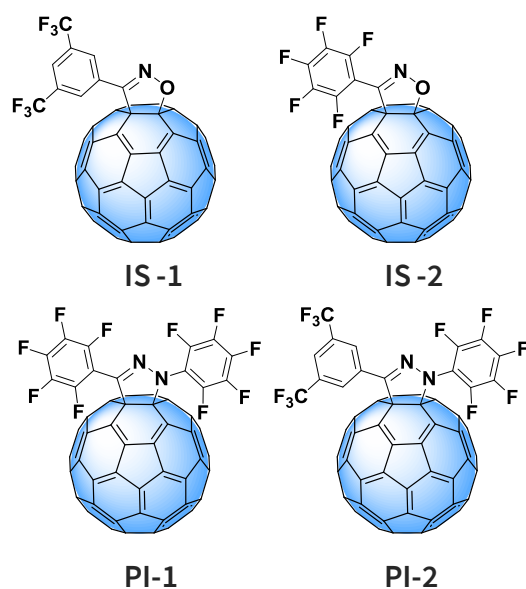


**Figure 1.13:** Structures of the derivatives **IS-1**, **IS-2**, **PI-1**, and **PI-2**.<sup>142</sup>

Moreover, polyethylene glycol-substituted fullerenes were recently incorporated into the light harvesting perovskite with remarkable effects on the stability against moisture. This will be the subject of chapter 3.2.

### 1.3 Conclusions

Despite their still short history, PSCs have crossed paths with fullerenes many times. The chemistry of these compounds makes them suitable for numerous applications concerning this new emerging photovoltaic technology. In this introduction, several examples of fullerenes used either as charge transporting materials or additives have been introduced. C<sub>60</sub> and derivatives showed beneficial effects against some of the biggest perovskite issues, such as stability and hysteresis.

In light of all these findings, fullerenes might play a key role for the future commercialization of PSCs.





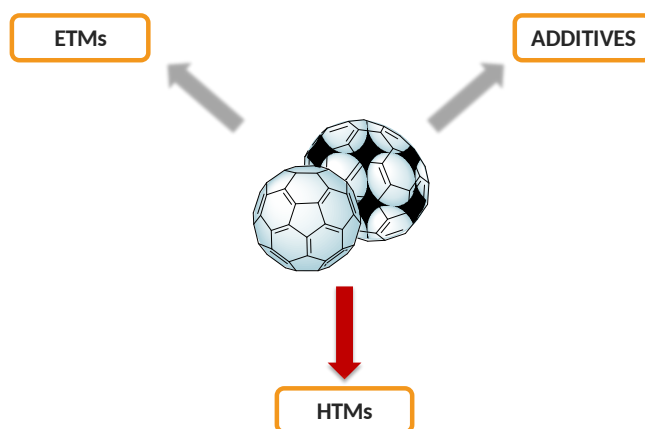
# Objective

---

In light of what reported in the introduction, the general aim of this thesis is to once more highlight the versatility of the fullerenes and, at the same time, try to overcome some of perovskite solar cells' mayor drawbacks, such as stability and hysteresis.

More specifically, new fullerenes are synthesized in order to adapt the fullerene structure to the specific aim, by for example attaching hygroscopic moieties or electron-donating ones. The newly synthesized structures, as well as the pristine fullerene cages, are exploited in the best possible way within the device structure in order to maximize their benefits.

In fact, in the following chapters fullerenes will play the roles of electron-transporting material, hole-transporting material, or additive for the perovskite layer. In each case, the introduction of the fullerenes in the cells showed some remarkable benefits.





## Results and Discussion

---



Pristine Fullerenes as Electron Transporting Materials in Regular, Compact PSCs



PEG-C<sub>60</sub>-based Materials for PSCs with Improved Moisture Resistance and Reduced Hysteresis



Innovative HTM with C<sub>60</sub> Core



### 3.1 Pristine Fullerenes as ETMs in Regular, Compact PSCs

#### 3.1.1 Preamble

Fullerene  $C_{60}$  and its derivatives play a fundamental role as ETMs in inverted PSCs.<sup>90, 143</sup> On the other hand, the amount of works considering fullerenes as ETMs in regular PSCs is considerably lower. Snaith and co-workers first replaced  $TiO_2$  with  $C_{60}$  in regular PSCs.<sup>76</sup> This finding paves the way to the development of plastic-based PSCs because, contrary to that generally reported for  $TiO_2$ , the integration of  $C_{60}$  as ETM in PSCs may be accomplished through spin-coating at ambient conditions and low annealing temperature (i.e.  $\leq 150^\circ C$ ). Furthermore, the evidence of the suitability of  $C_{60}$  as ETM for PSCs opens the way for many other fullerene derivatives to be used as ETMs. Among them,  $C_{70}$  is a viable alternative (Figure 3.1.1).

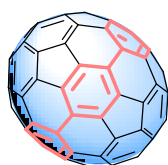


**Figure 3.1.1:** Structure of  $C_{70}$ . The belt of hexagonal rings that makes this molecule different from  $C_{60}$  is highlighted in pink.

$C_{70}$  is an oval-shaped molecule containing 70 carbon atoms; similarly to  $C_{60}$ , the cage is made of hexagonal and pentagonal rings. The difference lies in a belt of 5

hexagonal rings inserted at the equator, which made the molecule look more like a rugby than a soccer ball. The energy of the LUMO of  $C_{70}$  is nearly identical to that of  $C_{60}$ .<sup>144</sup> But the similarities stop here: in fact, the electron mobility of  $C_{70}$  is around two orders of magnitude lower than that of  $C_{60}$ ,<sup>145</sup> and its light harvesting properties are also notably different: in fact,  $C_{70}$  cage presents  $D_{5h}$  symmetry, and thanks to this feature the molecule is able to absorb sunlight in a large region of the visible spectrum.<sup>146</sup> Furthermore, its solubility is higher of that of  $C_{60}$ . According to these premises, it is not surprising that  $C_{70}$  was functionalized to obtain a **PC<sub>61</sub>BM** analogue, **PC<sub>71</sub>BM**, to be used use as ETM in OPV.<sup>147</sup> It is worth noticing that Lee, Heeger, and co-workers. prepared a device with 6.1% of PCE and an internal quantum efficiency of almost 100%, that means that virtually every absorbed photon led to the generation of a separated pair of carriers, which are all collected at the electrodes.<sup>148</sup>

The most noteworthy result achieved with a **PC<sub>71</sub>BM** derivative in OPV was obtained with a cyanovinylene 4-nitrophenyl substituent, that was previously employed to improve **PC<sub>61</sub>BM** performances,<sup>149</sup> and that allowed the PCE to increase from 3.23% of **PC<sub>71</sub>BM** to 5.83% for the novel fullerene derivative.<sup>150</sup>

Another interesting application of  $C_{70}$  in OPV is explained in the work of Dyakonov, Martín, and co-workers. The group investigated several different homo- and heterodimers of  $C_{60}$  and  $C_{70}$ <sup>146</sup> finding that the analyzed heterodimers presented lower charge transfer ability than the homodimers, which is also shown by the reduced

quenching of the photoluminescence. Among the analyzed dimers, C<sub>70</sub>-homodimer showed the best features for the application in OPV, thanks to the longer lifetime of the polaron states formed during photoinduced absorption.

It is important to remark that working with C<sub>70</sub> and derivatives requires much higher costs and efforts than those required for the C<sub>60</sub> analogues. This is due to the lack of symmetry of the C<sub>70</sub> cage, which makes the monoaddition result in three different isomers. Hence, the purification processes will be longer and trickier than those required for C<sub>60</sub> derivatives. Furthermore, the production techniques for the pristine C<sub>60</sub> and C<sub>70</sub> usually give higher amounts of the former.<sup>85</sup>

Even if favourable for OPV, the optical properties of C<sub>70</sub> should in principle limit the use of this fullerene in PSCs. Nonetheless, in the following chapter we will describe the successful incorporation of C<sub>70</sub> as ETL by spin-coating into regular PSCs.<sup>122</sup>

### 3.1.2 Morphology of the Fullerene Films

C<sub>60</sub> and C<sub>70</sub> were deposited by spin-coating 25 mg ml<sup>-1</sup> solutions in *o*-DCB onto FTO-glass substrates. A two-step protocol, with a first step of 1500 rpm for 60 s and a second step of 2700 rpm for 60 s, was followed. These conditions resulted in ~ 40 nm thick films (Figure 3.1.2), as estimated from a statistical evaluation of several cross section Field Emission Scanning Electron Microscopy (FE-SEM) micrographs of both fullerene films (Figure 3.1.2 B and D). Figure 3.1.3 shows the absorptance, the reflectance, and the transmittance of

the C<sub>60</sub> and C<sub>70</sub> films deposited on FTO/glass. The light harvesting properties in the UV region look quite similar

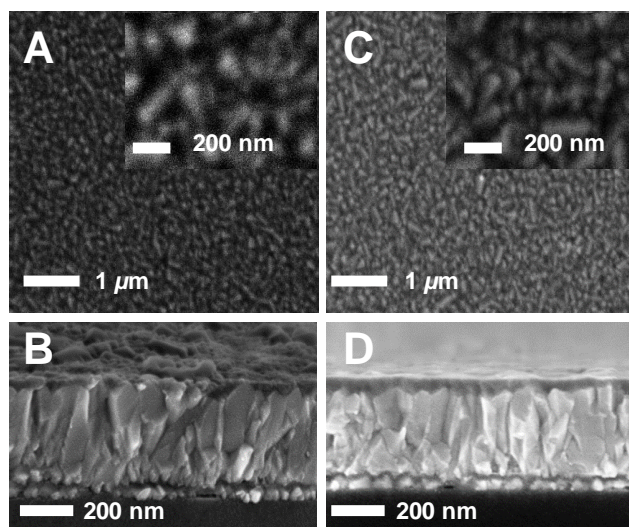


**Figure 3.1.2:** FE-SEM micrographs of the top views and cross sections of glass/FTO/fullerene samples, either containing C<sub>60</sub> (A, B) or C<sub>70</sub> (C, D)

between the two fullerenes. However, as expected, C<sub>70</sub> films exhibited higher absorptance in the visible range.

### 3.1.3 Preparation of PSCs

In order to study the application of fullerene films in PSCs, perovskite films were deposited on top of them. The deposition was performed using two different methods of solution deposition:

- MAPbI<sub>(3-x)</sub>Cl<sub>x</sub> films were deposited recurring to a commonly used 1-step spin coating method from a perovskite precursor solution.
- MAPbI<sub>3</sub> films were deposited through a 2-step procedure, i.e. the deposition of a PbI<sub>2</sub> layer by spin coating, subsequently treated by spin coating a solution of MAI on the top of it.<sup>151</sup>



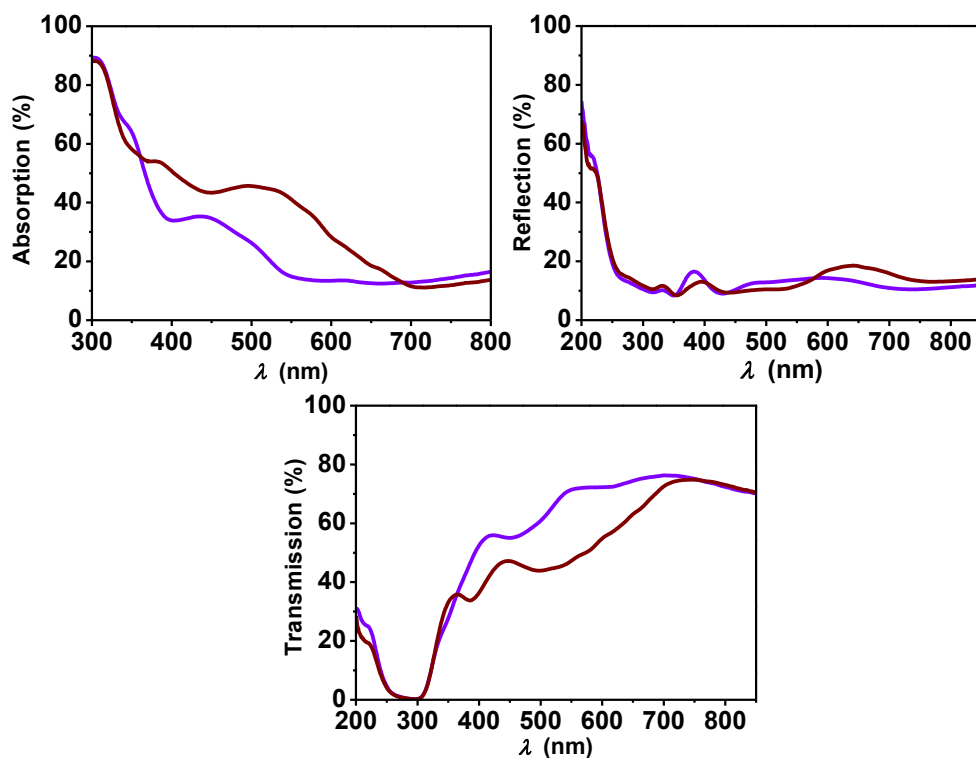


**Figure 3.1.3:** Absorbance, reflectance, and transmittance of the  $C_{60}$  (violet line) and  $C_{70}$  (maroon line) films deposited on FTO/glass.

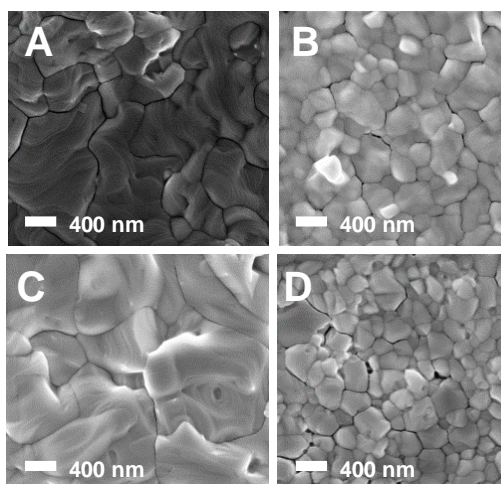


**Figure 3.1.4:** Top-view FE-SEM micrographs of the perovskite films processed by different methods on FTO glass/ $C_{60}$  (1-step: A, 2-step: B) and FTO glass/ $C_{70}$  (1-step: C, and 2-step: D).

Figure 3.1.4 shows the FE-SEM top view micrographs of the perovskite films deposited by either 1-step or 2-step methods on  $C_{60}$  (3.1.4 A and B) and  $C_{70}$  (3.1.4 C and D).

Each film deposited recurring to the same method looked like one another, highlighting

the reproducibility of both techniques. Regardless of the nature of the fullerene, the perovskite obtained through 1-step method presents a larger grain size compared to that deposited by the 2-step method. This may be attributed to the  $\text{PbCl}_2$  used in the 1-step method: this has been demonstrated to be an efficient precursor to promote grain growth in the perovskite films.<sup>152, 153</sup>

This was corroborated by monitoring the variation of the crystal size by X-Ray Diffraction (XRD): in fact, smaller crystals were detected in 1-step processed samples (Figure 3.1.5 A). Furthermore, the XRD patterns (Figure 3.1.5 B) pointed out relevant differences in the orientation degree of the perovskite films.

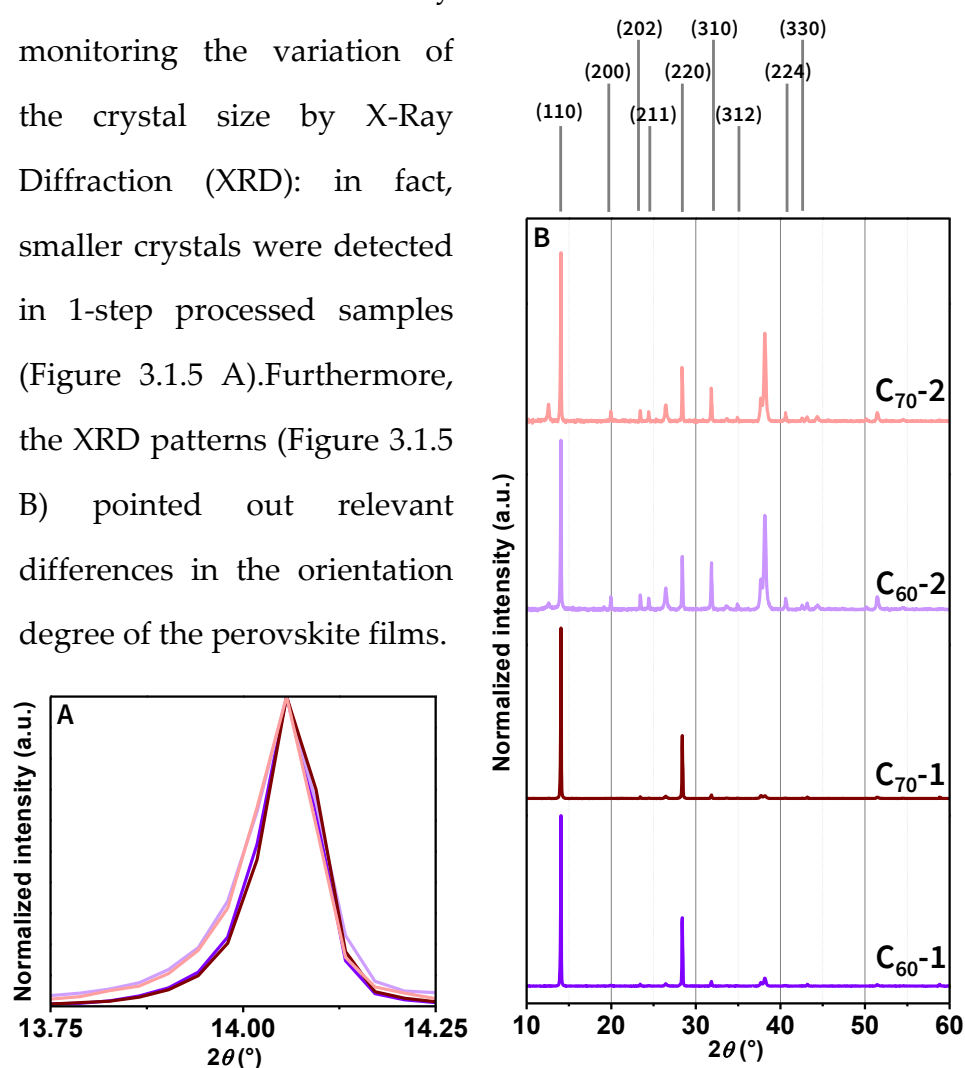
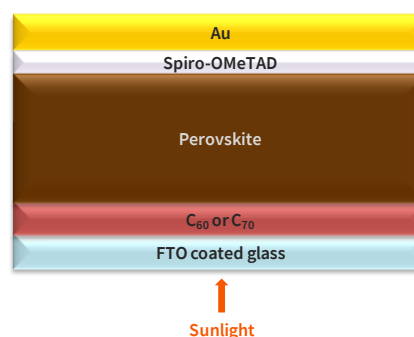


Figure 3.1.5: A) Magnified view of the (110) XRD peak of the fullerene/perovskite samples and B) XRD patterns and plane designations of each type of PSC. In violet, 1-step perovskite on  $\text{C}_{60}$  (C<sub>60</sub>-1); in maroon, 1-step perovskite on  $\text{C}_{70}$  (C<sub>70</sub>-1); in light violet, 2-step perovskite on  $\text{C}_{60}$  (C<sub>60</sub>-2); in pink, 2-step perovskite on  $\text{C}_{70}$  (C<sub>70</sub>-2).

Only features belonging to the (110) and (220) planes were detected in patterns registered from samples obtained by 1-step method, while 2-step-processed samples showed many features belonging to other planes (i.e. (200), (202), (211), and (310)). Additionally, in contrast to the 1-step-, 2-step-processed films show a minor feature at  $2\theta \sim 12.6^\circ$  suggesting the presence of  $\text{PbI}_2$  traces.

### 3.1.4 Photovoltaic characterization

The devices were completed with the standard Spiro-OMeTAD as HTM and a gold contact. Figure 3.1.6 shows the final device architecture. In accordance with the previous experiments, there were no big differences between the cells



**Figure 3.1.6:** Device architecture of the PSCs prepared in this study: FTO glass/fullerene/perovskite/Spiro-OMeTAD/Au

containing the two fullerenes; in fact, the most important role in determining the final performance seems to be played by the deposition method of the perovskite. 1-step processing resulted in devices with higher  $J_{sc}$ . This might be attributed to a stronger light harvesting ability of this kind of perovskite, as confirmed by the comparison of the optical absorptance of  $\text{C}_{70}$ -containing PSCs perovskite solar cells, prepared either through 1-step or 2-step method (Figure 3.1.7).

Another factor that might cause this difference is the stronger orientation of the 1-step perovskite film along the (110) direction.<sup>154</sup>

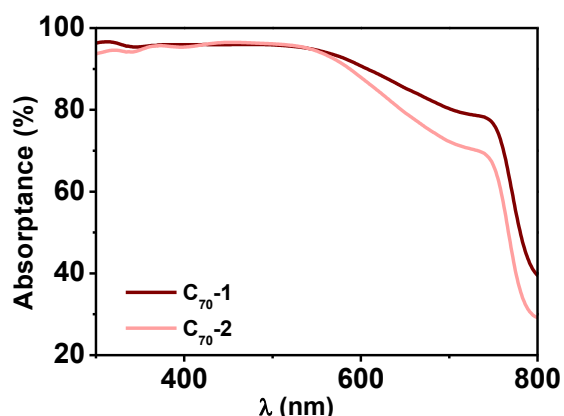


**Figure 3.1.7:** Optical absorbance of PSCs based on  $C_{70}$  as ETL either processed by 1-step ( $C_{70-1}$ , maroon line) or 2-step method ( $C_{70-2}$ , pink line).

On the other hand, 2-step processed devices presented higher  $V_{oc}$  and  $FF$  (respectively,  $\sim 40$  mV and  $\sim 8\%$  higher than those exhibited by 1-step processed perovskite). The improvement of both parameters may be related

to the presence of  $PbI_2$  traces, which has been proposed to passivate traps in the perovskite grains.<sup>155</sup>

Table 3.1.1 summarizes the photovoltaic parameters of the best devices, whose  $J$ - $V$  curves are showed in Figure 3.1.8. A statistic report of the PV parameters is shown in figure 3.1.9.

Since the obtained results do not seem to depend on the fullerene

	$J_{sc, eQE}$ ( $mA\ cm^{-2}$ )	$J_{sc}$ ( $mA\ cm^{-2}$ )	$V_{oc}$ (mV)	$FF$ (%)	PCE (%)
$C_{60-1}$	14.6	14.2	938	61	8.1
$C_{60-2}$	14.4	12.9	979	69	8.8
$C_{70-1}$	16.6	14.3	959	61	8.4
$C_{70-2}$	12.8	11.9	1003	66	7.9

**Table 3.1.1:** Photovoltaic parameters of the best solar devices with different fullerenes and processing methods. Together with the aforementioned parameters, integrated photocurrent from the external quantum efficiency spectra (eQE) is also given.

nature,  $C_{70}$  might be also used as ETM in efficient PSCs. In fact, the average  $V_{oc}$  obtained from  $C_{70}$ -containing devices is slightly higher ( $\sim 20$  mV) than that of  $C_{60}$ -containing devices. On the contrary, the former showed higher  $J_{sc}$ , maybe due to the more efficient solar light absorption operated by  $C_{70}$ .

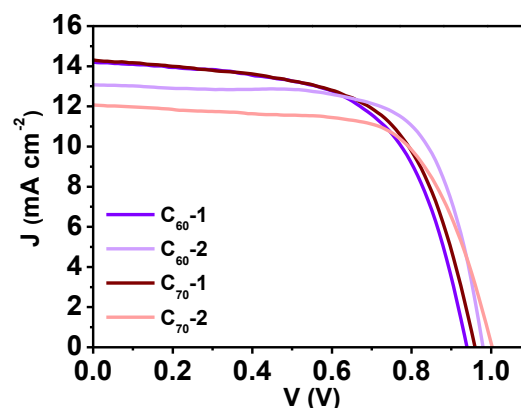


**Figure 3.1.8:**  $J$ - $V$  curves of the best solar devices with different fullerenes and processing methods. The curves are consistent with what discussed above, i.e. the higher  $J_{sc}$  in 1-step processed device and the higher  $V_{oc}$  and  $FF$  in the 2-step processed ones.

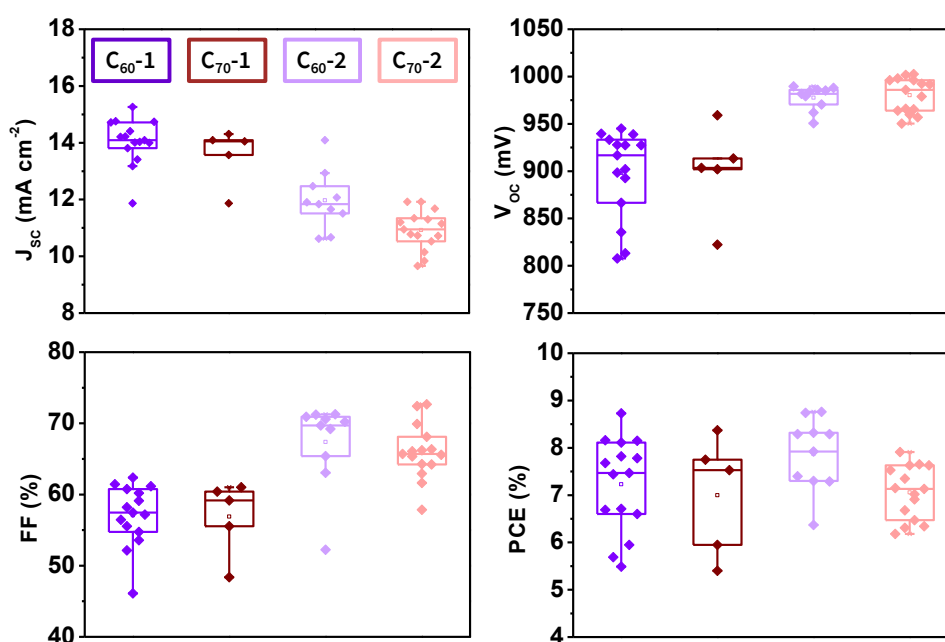


**Figure 3.1.9:** Statistics of the PV parameters of the different devices prepared for this study.

The external quantum efficiency (eQE) spectra, which show maximum values for wavelengths larger than 650 nm, seem to support this scenario (Figure 3.1.10).

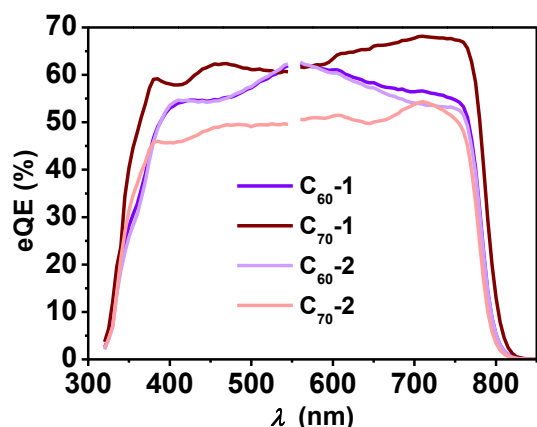


**Figure 3.1.10:** External quantum efficiency (eQE) of the best cells obtained in each processing condition.

Interestingly, in the FE-SEM micrographs of the cross sections of  $C_{70}$ -containing devices some island-like features were detected, meaning the film is not continuous.

Nevertheless, even if

$C_{60}$  films are known to be partially dissolved during the perovskite solution processing,<sup>76</sup> a rather homogeneous film was detected in PSCs containing this fullerene. All the FE-SEM micrographs can be seen in Figure 3.1.11.

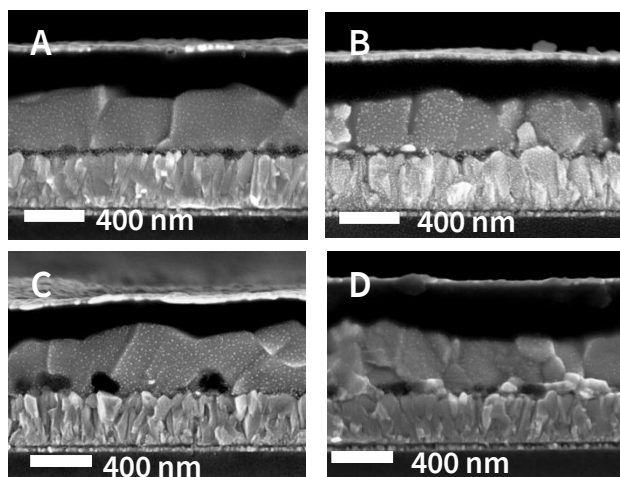


**Figure 3.1.11:** Cross section of the different devices. A)  $C_{60}$ -1, B)  $C_{60}$ -2, C)  $C_{70}$ -1, D)  $C_{70}$ -2. In both C and D the island-like pattern can be clearly appreciated.

### 3.1.5 Improving the fullerene film: the “Fullerene Saturation Approach”

In order to understand the effects of the processing solvent, a drop of DMF was deposited on the approximately 40 nm-thick fullerene films and held for one minute. The FE-SEM micrographs reported in Figure 3.1.12 show significant differences in the DMF treated samples. The  $C_{60}$  film was partially dissolved leaving lots of uncoated FTO areas (Figure 3.1.12 C).

Moreover, several crystal-like features were

detected in the  $C_{70}$  sample, which was highly affected (Figure 3.1.12 D). Hence it can be concluded that DMF affects both  $C_{60}$  and  $C_{70}$  films, even if to a different extent. The higher solubility of  $C_{70}$  in DMF was also proven by preparing saturated solutions (i.e.  $\sim 0.10 \text{ mg ml}^{-1}$  for  $C_{60}$  and  $\sim 0.25 \text{ mg ml}^{-1}$  for  $C_{70}$ , Figure 3.1.12 E).

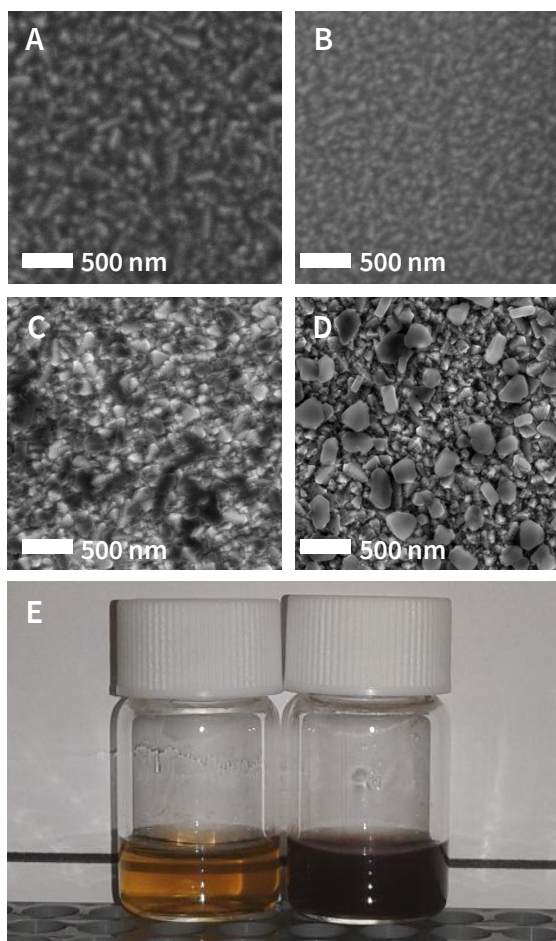


**Figure 3.1.12:** Top view FE-SEM micrographs of the 40 nm-reference films ( $C_{60}$ : A,  $C_{70}$ : B) and after 1 minute of exposure to pure DMF ( $C_{60}$ : C,  $C_{70}$ : D). E shows DMF solutions saturated with  $C_{60}$  (left) and  $C_{70}$  (right)

To try to minimize the effect of DMF on the fullerene films, a drop of either  $C_{60}$ - or  $C_{70}$ -saturated solution was deposited on the films and left for one minute. Interestingly, although some pinholes could still be observed, the morphology of the resulting films (Figure 3.1.13 A and B) was roughly comparable to that from the initial ones (Figure 3.1.12 A and B).

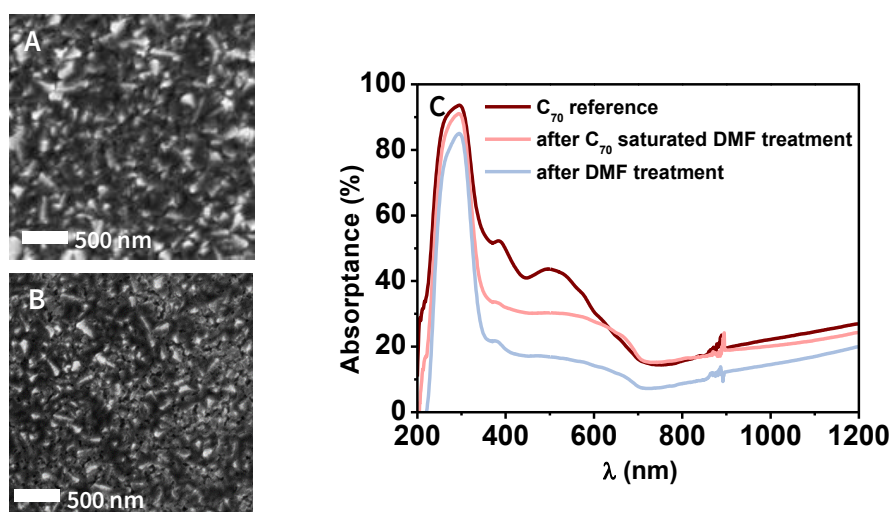


**Figure 3.1.13:** FE-SEM top views of  $C_{60}$  (A) and  $C_{70}$  (B) after treatment with the respective saturated DMF solutions. C: absorbance of the three differently treated 40 nm- $C_{70}$  films (maroon: reference, pink: treated with  $C_{70}$  saturated DMF, light blue: treated with pure DMF).

To support the hypothesis of the reduced dissolution, absorbance experiments were performed: the samples treated with fullerene-saturated solutions showed slightly higher absorbance than those treated with pure DMF, as can be observed in Figure 3.1.13 C.

Anyway, the thickness of the initial  $C_{70}$  film seems to play an important role. In fact, island-like features were also detected when treating very thin  $C_{70}$  films (i.e.  $\sim 20$  nm) with  $C_{70}$ -saturated DMF solution. However, the final samples showed slightly higher



absorptance with respect to those treated with pure DMF, suggesting decreased film dissolution.

In light of these findings, new series of PSCs were prepared by processing the perovskite films from fullerene-saturated DMF-based solutions (fullerene saturation approach). To perform these experiments, fullerenes were dissolved in the perovskite precursor for the 1-step process and in the  $\text{PbI}_2$  solution for the 2-step method. Figure 3.1.14 shows the back-scattered (i.e. chemically sensitive contrast) FE-SEM micrographs of the PSCs based on  $\text{C}_{70}$  as ETM and perovskite films processed from pure (A, C, and E) and  $\text{C}_{70}$ -saturated (B, D, and F) DMF.

As expected, a continuous  $\sim 40$  nm fullerene film was detected in devices based on perovskite films processed by 2-step method using a  $\text{C}_{70}$ -saturated  $\text{PbI}_2$  DMF solution (Figure 3.1.14 B). 20 nm thin films, however, still undergo some degradation, meaning this approach is not effective enough for such thin films (Figure 3.1.14 E and F).

However, island-like features were also detected in solar cells processed by the 1-step method, regardless of the fullerene presence in the processing solution (Figure 3.1.14 C and D). The reason of this stronger degradation could be the longer contact time between  $\text{C}_{70}$  and the DMF retained in the deposited film in perovskite-solvent intermediate phases.<sup>156</sup>

Furthermore, similarly to what observed through preliminary studies,  $\text{C}_{60}$  layer looks the same when treated with perovskite solutions in pure or  $\text{C}_{60}$ -saturated DMF (Figure 3.1.14 G-J).

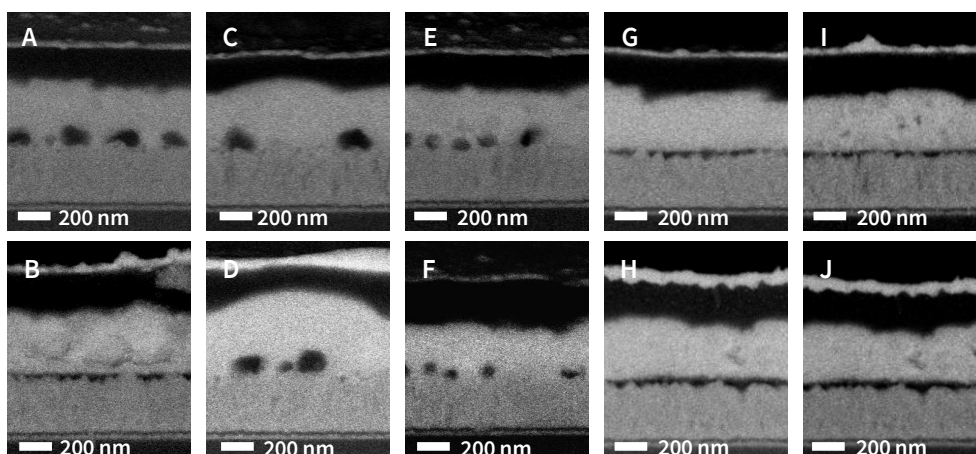


**Figure 3.1.14:** A-F: Back-scattered FE-SEM micrographs of PSCs with  $C_{70}$  as  $\sim 40$  nm ETL (A, B, C, and D) and  $\sim 20$  nm initial film thickness (E and F) with perovskite films processed by different methods: 2-step from  $PbI_2$  deposited from either pure (A, E) or  $C_{70}$ -saturated (B, F) DMF, 1-step using either pure (C) or  $C_{70}$ -saturated (D) DMF. G-J: Back-scattered FE-SEM micrographs of PSCs with  $C_{60}$  as  $\sim 40$  nm ETL with perovskite films processed by different methods: 2-step from  $PbI_2$  deposited from either pure (I) or  $C_{60}$ -saturated (J) DMF, 1-step using either pure (G) or  $C_{60}$ -saturated (H) DMF.

Table 3.1.2 shows the photovoltaic parameters extracted from the  $J$ - $V$  curves of the best devices of the series. The statistics of the different photovoltaic parameters are summarized in Figure 3.1.15 for  $C_{70}$  and 3.1.16 for  $C_{60}$ .

Interestingly, devices presenting a continuous-like  $C_{70}$  film offered the poorest performance. The limitations might be due to an excessively resistive  $C_{70}$  film, caused by its reduced electron mobility. This implies that devices that still present some island-like features showed better performance.

Nonetheless, a positive effect of adding  $C_{70}$  to the formulation of the perovskite processing solutions can be concluded, since it helped modulating and improving the morphology of the underlying ETL.

	$J_{sc}$ ( $\text{mA cm}^{-2}$ )	$V_{oc}$ (mV)	FF (%)	PCE (%)
$C_{70}$ -1	13.8	947	62	8.1
$C_{70}$ -1 (saturated)	15.1	995	69	10.4
$C_{70}$ -2	11.9	1003	66	7.9
$C_{70}$ -2 (saturated)*	10.9	966	58	6.1
$C_{70}$ -2 (saturated)	14.5	1005	69	10.0
$C_{60}$ -1	14.7	923	65	8.8
$C_{60}$ -1 (saturated)	15.4	993	75	11.4
$C_{60}$ -2	12.9	979	70	8.8
$C_{60}$ -2 (saturated)	14.5	1010	69	10.1

**Table 3.1.2:** Photovoltaic parameters of best solar cells including perovskite films processed from pure (reference) and fullerene-saturated DMF. \*Refers to the device with continuous-like  $C_{70}$  film.

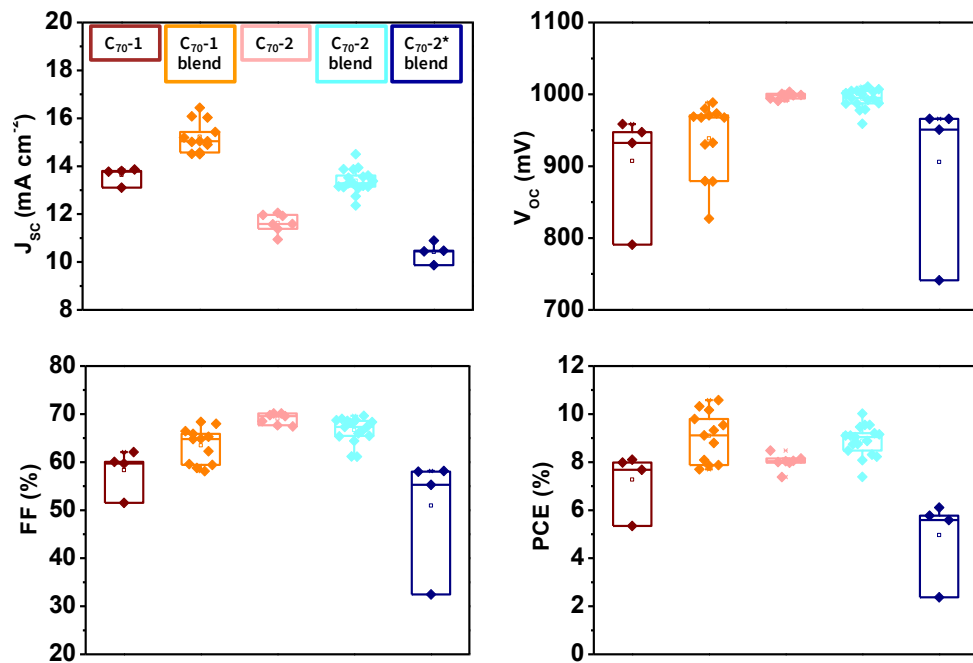


**Figure 3.1.15:** Statistics related to  $C_{70}$ -based PSCs.  $C_{70}$ -2\* Refers to the device with continuous-like  $C_{70}$  film.

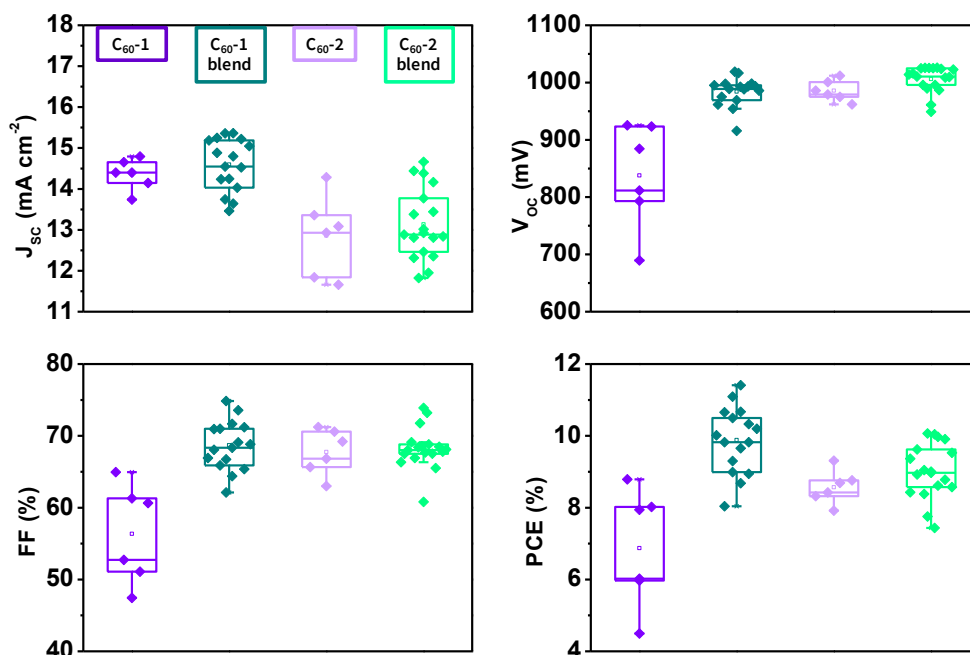


Figure 3.1.16: Statistics related to C<sub>60</sub>-based PSCs.

Alongside the experiments with C<sub>70</sub>, a similar study was carried out on PSCs with C<sub>60</sub> films as ETLs in order to prove the effectiveness of the fullerene saturation approach. The photovoltaic parameters of the best C<sub>60</sub>-containing solar cells are also shown in Table 3.1.2. A very significant improvement of the performances was observed for devices including perovskite films processed from C<sub>60</sub>-saturated solutions, reaching PCE of 11.4 % for 1-step processing. There is an interesting difference between the behaviour of C<sub>60</sub> and C<sub>70</sub> films that is worth pointing out: the thickness of the C<sub>60</sub> films does not seem to be a critical parameter, as can be seen in Table 3.1.3. This differs from the behaviour reported in literature for very thin (< 20 nm) thermally evaporated C<sub>60</sub> films.<sup>157</sup>

	$J_{sc}$ ( $\text{mA cm}^{-2}$ )	$V_{oc}$ (mV)	$FF$ (%)	$PCE$ (%)
$C_{60}$ (20 nm)-2 (saturated)	13.4	1009	74	10.0
$C_{60}$ (60 nm)-2 (saturated)	14.8	962	70	9.9

**Table 3.1.3:** Photovoltaic performances of PSCs with  $C_{60}$  as ETL with different thickness (~20 and ~60 nm).

It is clear that even if the solubility, and consequently the effect on the deposited films, of  $C_{60}$  and  $C_{70}$  in DMF are different, the use of fullerene-saturated perovskite processing solutions is beneficial. In support of this, some PCE improvement was also obtained in planar  $TiO_2$ -based solar cells when the perovskite film was deposited from  $C_{60}$ -saturated solutions (Table 3.1.4).

	$J_{sc}$ ( $\text{mA cm}^{-2}$ )	$V_{oc}$ (mV)	$FF$ (%)	$PCE$ (%)
$TiO_2$ reference	13.1	997	73	9.6
$TiO_2/(C_{60}$ -saturated)	13.9	1008	73	10.2

**Table 3.1.4:** Photovoltaic performances of PSCs with  $TiO_2$  as ETL and perovskite films deposited from pure (black) and  $C_{60}$ -saturated DMF.

The higher results might be due to the passivating effect of the fullerenes on some defects in perovskite.<sup>137</sup> This is also linked to the reduction of hysteresis; this well-known effect of fullerenes is here reconfirmed.

It is very common for PSCs to present batch to batch variations. For this reason, a batch of cells containing each one of the ETMs discussed in this chapter:  $C_{60}$ ,  $C_{70}$ , or compact  $TiO_2$  was prepared. In this case it is clear that the good results obtained do not depend on

batch-to-batch variation, being highly comparable to the reference performances. Figure 3.1.17 shows the best curves obtained with each one of the ETLs and the corresponding device parameters are reported in Table 3.1.5.

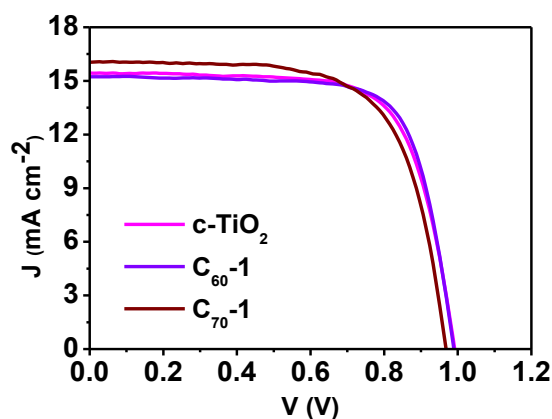


Figure 3.1.17:  $J$ - $V$  curves of devices using different ETMs (compact  $\text{TiO}_2$ ,  $\text{C}_{60}$ ,  $\text{C}_{70}$ ). In the case of fullerene-including devices, the perovskite processing solution was saturated with the corresponding fullerene.

	$J_{sc}$ ( $\text{mA cm}^{-2}$ )	$V_{oc}$ (mV)	FF (%)	PCE (%)
$\text{TiO}_2$	14.8	984	71	10.4
$\text{C}_{60}$ -1 (saturated)	15.2	988	74	11.1
$\text{C}_{70}$ -1 (saturated)	16.1	968	68	10.6

Table 3.1.5: PV performances of the devices whose  $J$ - $V$  curves are depicted in Figure 3.1.18.

To sum up, in this work two important targets have been achieved. First, the possibility to use solution-processed  $\text{C}_{70}$  as ETM in efficient regular PSCs is demonstrated; the obtained PCE is comparable to that registered with  $\text{C}_{60}$  reference devices. Anyway, the higher solubility of  $\text{C}_{70}$  in DMF has to be taken into consideration while preparing the perovskite films. Another important difference that should be kept in mind is that the relatively reduced electron mobility in  $\text{C}_{70}$  makes the PCE much more sensitive to film thickness

than in C<sub>60</sub>-containing solar cells. As a consequence, C<sub>70</sub>-containing solar cells show much better performances when the fullerene films possess an island-like morphology. This finding leads to the conclusion that a potential ETM candidate should not be excluded just because of low electron mobility or absorption in the visible region. Second, the use of fullerene saturation approach is proposed as an innovative strategy to improve the performance of PSCs. The improvement shown by solar cells based on different ETLs (C<sub>60</sub>, C<sub>70</sub>, and TiO<sub>2</sub>), including perovskite films processed by different methods (1-step and 2-step) points towards the universality of the proposed approach. Hence, the fullerene saturation approach could allow the exploration of new ETLs which are partially soluble in the perovskite processing solvent.

Moreover, this approach paved the way to a whole new field of ETL-free PSCs with fullerene-perovskite blend films directly deposited onto FTO/glass. It is noted that this innovative solar cell architecture has been developed ulteriorly in the research group.<sup>39, 140, 142</sup>

### 3.1.6 Materials and Methods

#### Reagents, Solvents, and Other Materials

All chemicals were obtained from commercial suppliers in high purity degree and used without further purification: glass/FTO substrates (TEC15, Hartford Glass), C<sub>60</sub> (99.9%, Sigma-Aldrich), C<sub>70</sub> (99%, SES Research), *ortho*-dichlorobenzene (*o*-DCB, Chromasolv© 99%, Sigma Aldrich), CH<sub>3</sub>NH<sub>3</sub>I (DYESOL), PbCl<sub>2</sub> (98%, Sigma Aldrich), DMF (extra pure, Scharlab), PbI<sub>2</sub> (99%, Sigma Aldrich), *iso*-propanol (synthetic grade, Scharlab), Spiro-OMeTAD (99%, Feiming Chemicals Limited), LiTFSI (lithium bistrifluoromethanesulfonimide, 99.9%, Solvionic), TBP (96%, Sigma Aldrich), CB (99.8%, Sigma Aldrich), ACN (UV HPLC grade, Scharlab).

#### Device Fabrication

Glass/FTO samples were cleaned following the procedure: sonication in distilled water with soap for 5 min, thorough rinsing with distilled water and drying, sonication in acetone, ethanol, and *iso*-propanol for 15 min in each solvent. The C<sub>60</sub> and C<sub>70</sub> *o*-DCB solutions (i.e. ~ 25 mg ml<sup>-1</sup>) were prepared by applying sonication during 30 min. The fullerene films were deposited by spin-coating in an argon-filled glove box. A two-step protocol, with a first step of 1500 rpm for 60 s and a second step of 2700 rpm for 60 s, was followed. These conditions resulted in ~ 40 nm thick films (Figure 2). Thicker and thinner films were also deposited by decreasing and increasing, respectively the spin



rate. Subsequently, the prepared films were submitted to a process of thermal annealing at 150°C for 1 h.

The halide perovskite films were deposited by two different approaches named “1-step” and “2-step”. In the former, the perovskite solution was prepared dissolving 5.25 mol of CH<sub>3</sub>NH<sub>3</sub>I and 1.75 mol of PbCl<sub>2</sub> (molar ratio 3:1) in 2 ml DMF and stirred overnight. The perovskite was deposited by spin-coating following a two-part protocol, which consists of a first step of 500 rpm for 5 s followed by a second step of 2000 rpm for 45 s. Subsequently the samples were annealed at 100°C for 2 h in order to ensure complete perovskite formation.

In the 2-step deposition, a solution of PbI<sub>2</sub> 30%wt in DMF was first spin-coated at 2300 rpm for 30 s. In the second step, the conversion was performed by depositing a solution of CH<sub>3</sub>NH<sub>3</sub>I of 50 mg ml<sup>-1</sup> in *iso*-propanol. After 20 s, the samples were spin-coated at 4000 rpm for 20 s. Subsequently the samples were annealed at 100°C for 2 h to complete the perovskite conversion.

On top of the perovskite layer, the Spiro-OMeTAD hole selective contact was deposited from a solution which contained 108.4 mg of Spiro-OMeTAD in 953.43 μl of chlorobenzene, 17.17 μl of a LiTFSI solution (520 mg ml<sup>-1</sup>) in ACN, and 29.4 μl *tert*-butylpyridine. The HTM layer was deposited by spin-coating the solution at 4000 rpm for 60 s. The samples were left in the desiccator overnight. Finally, an array of round Au back contacts (~ 0.07 cm<sup>-2</sup>) was deposited by thermal evaporation at > 5 × 10<sup>-6</sup> Torr in a NANO38 (Kurt J. Lesker) apparatus using a shadow mask.

### Device Characterization

The morphology and structural properties of the films were analysed using an ULTRA plus ZEISS field emission scanning electron microscope (FE-SEM) and a Bruker AXS-D8 Advance X-ray diffractometer using Cu K $\alpha$  radiation. The absorptance spectra were obtained from the transmittance and reflectance spectra, which were measured using a JASCO V-570 spectrophotometer with integrating sphere.

The current-voltage ( $J$ - $V$ ) characteristics of the solar cells were measured using a xenon arc lamp simulator equipped with an AM 1.5 G spectral filter (Sun 2000, ABET Technologies). The intensity was adjusted to provide 1 sun ( $100 \text{ mW cm}^{-2}$ ) using a calibrated silicon solar cell. The  $J$ - $V$  characteristics were recorded scanning the potential from potentials higher than the open circuit voltage to zero (i.e. “reverse mode”) at  $\sim 300 \text{ mV s}^{-1}$ . Prior to the measurement, a voltage of  $\sim 1.2 \text{ V}$  was applied to the devices for 1 minute.

## 3.2 PEG-C<sub>60</sub>-based Materials as additives for PSCs

### 3.2.1 Preamble

Hybrid organic-inorganic perovskites used in solar cells show instability in presence of light, oxygen, excessive heat, and moisture.<sup>67</sup> In particular, when exposed to an humid environment, MAPbI<sub>3</sub> tends to decompose into methylammonium iodide (MAI) and lead(II) iodide (PbI<sub>2</sub>), the reactants used in its formation.<sup>73</sup> Hence, a possible strategy to overcome this issue could be resorting to chemical strategies to prevent water molecules to get close to the perovskite crystals. This could be accomplished recurring to appropriate structures which could bind water molecules by terms of coordination.

Following this idea, Zhao, Wei, Li, and co-workers added a simple polymeric framework to the perovskite solution.<sup>158</sup> In fact, resorting to polyethylene glycol (PEG) of molecular weights within a range of 12000-100000 Da, the group fabricated a series of solar cells which showed remarkable resistance against ambient moisture. The PEG solution (20 or 40 mg ml<sup>-1</sup>) was added to the perovskite solution in order to get a molar ratio of 1:1 between perovskite and the ethylene glycol (EG) monomer units. The high hygroscopicity of PEG, which

can coordinate several water molecules, seems to be at the root of this effect. In the same work, a mechanism of interaction between PEG and MAPbI<sub>3</sub> is proposed: the formation of hydrogen bonds

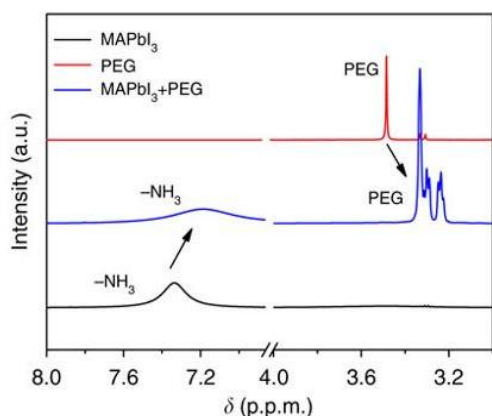


**Figure 3.2.1:** A comparison of NMR spectra of three deuterated DMSO solutions with MAPbI<sub>3</sub>, mixture of MAPbI<sub>3</sub>+PEG, and PEG, respectively.

between the ammonium part and the several PEG oxygens seems to be at the heart of this interaction, as seen through <sup>1</sup>H-NMR experiments (Figure 3.2.1)

The merging of this PEG approach and the use of fullerenes, with all their aforementioned benefits towards PV performances, is the foundation of this work. A series of C<sub>60</sub> derivatives with covalently bound PEG chains is presented as a novel elegant approach to create moisture resistant and hysteresis-free PSCs.

### 3.2.2 Synthesis and Characterization of the Fullerene Materials

A family of PEG-C<sub>60</sub> monoadducts was synthesized and characterized, each one bearing either one or two PEG chains linked to the cage through different bridges. The chosen PEG chain is PEG<sub>350</sub>-OMe, which is a polydisperse PEG mixture, capped on one side by a methoxy group, with an average molecular weight of 350 a.m.u. The structure of the three derivatives can be found in Figure 3.2.2.

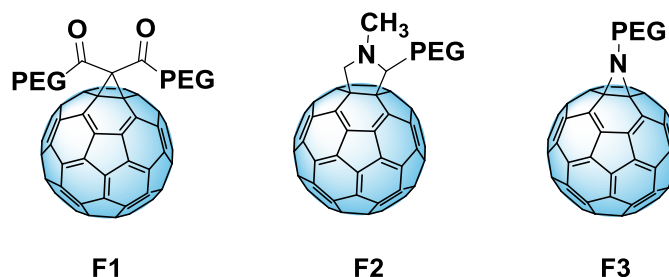


Figure 3.2.2: Structure of the three PEG-fullerenes (F1-F3), PEG denotes PEG<sub>350</sub>-OMe

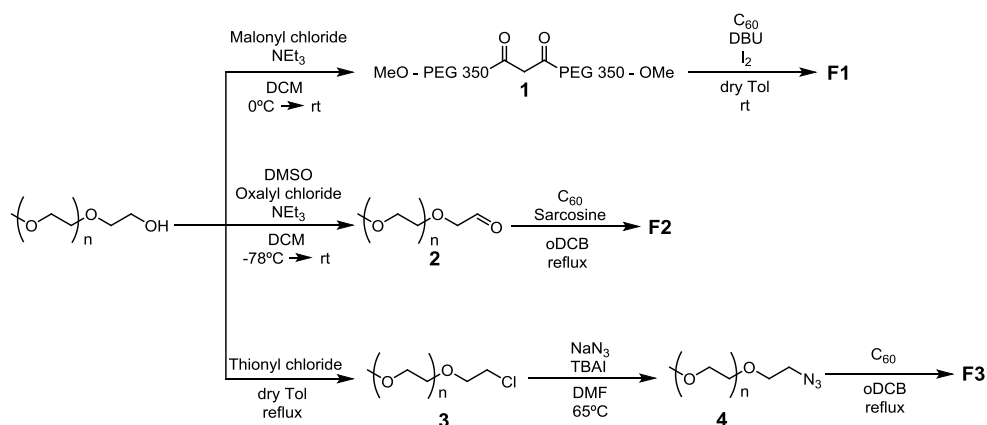
- In **F1**, two units of PEG were linked to C<sub>60</sub> through a *Bingel* reaction of the latter and a purposely tailored PEG-malonate **1**, which was synthesized from the reaction of PEG with malonyl chloride.<sup>159</sup>
- C<sub>60</sub> derivative **F2** was synthesized through a 1,3-dipolar cycloaddition.<sup>160</sup> In this reaction, an azomethine ylide is generated *in situ* by the reaction of the chosen PEG-aldehyde **2** and the alpha-amino acid sarcosine, and reacts with C<sub>60</sub> to form the characteristic pyrrolidinic linker.

PEG-aldehyde **2** was previously synthesized by the reaction of PEG and oxalyl chloride.

- In **F3** PEG and C<sub>60</sub> are linked through an aziridino moiety obtained by reaction between terminal azide-functionalized PEG **4** and C<sub>60</sub>.<sup>161</sup>

PEG-azide **4** was obtained from functionalization with sodium azide of product **3**, synthesized through a reaction of PEG with thionyl chloride.

Scheme 3.2.1 summarizes the syntheses of the three compounds. Due to the polydispersity of the starting material PEG<sub>350</sub>-OMe, the novel



**Scheme 3.2.1:** Syntheses of the three fullerene derivatives **F1**, **F2**, and **F3**.

PEG- $C_{60}$  derivatives **F1-F3** were obtained as polydisperse mixtures. The nature and the purity of the monoadduct mixtures were identified and confirmed using several characterization techniques, such as  $^1\text{H-NMR}$ ,  $^{13}\text{C NMR}$ , high-resolution mass spectrometry, and UV-Vis spectroscopy.

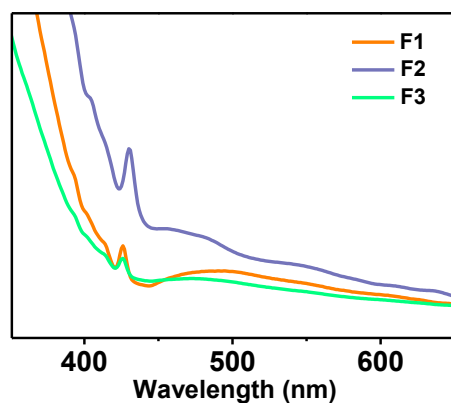


**Figure 3.2.3:** UV-Vis spectra of  $C_{60}$  derivatives **F1**, **F2**, and **F3**. The typical peak at around 430 nm is clearly visible for **F1** and **F2**.

The monoadducts **F1** and **F2** show a very typical UV-Vis absorption pattern, with a sharp peak at around 430 nm, as it can be seen in Figure 3.2.3.<sup>162</sup> This is due to the saturation of a single double bond of a [6,6] junction and confirms

the monoaddition of the PEG derivatives to the fullerene cage. In the case of **F3**, the aziridine ring can be located in both [6,6] and [5,6] junctions, which makes the typical peak less sharp (Figure 3.2.3).

Interestingly, in the case of **F1**, high resolution mass spectrometry (HRMS, Figure 3.2.4 A) and <sup>1</sup>H-NMR assign around 12 ethylene glycol (EG) units, that is lower than what is showed for the starting material **1**. In fact, **1** contained around 16 EG units, according to both

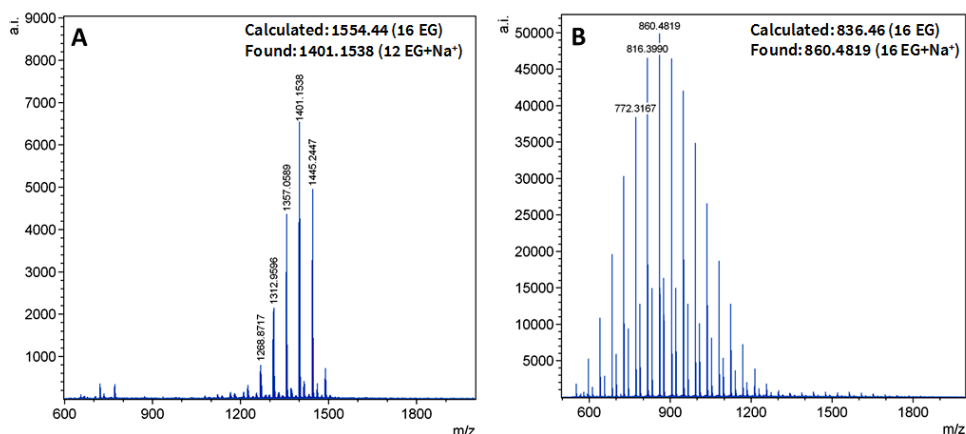


Figure 3.2.4: HRMS of **F1** (A) and the corresponding PEG-Malonate **1** (B).

mass spectrometry (Figure 3.2.4 B) and <sup>1</sup>H-NMR. The lower number of registered EG units with respect to the starting material is suspected to be due to difficulties during the separation process.

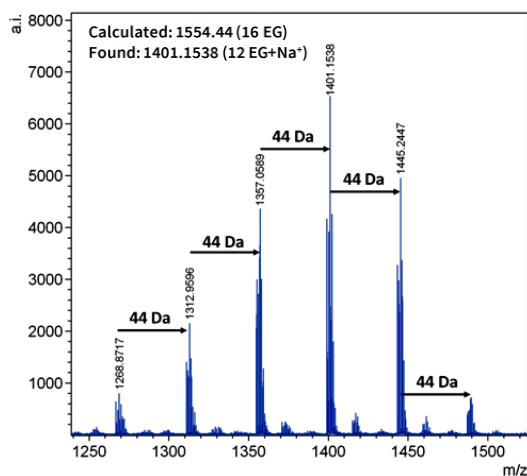
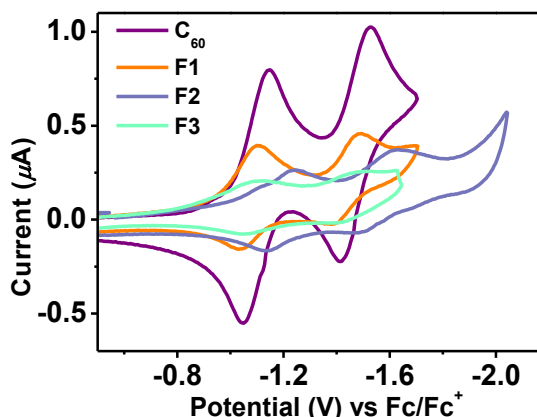


Figure 3.2.5: Magnification of the highest HRMS peaks of the compound **F1**. The pattern with the peaks equally differing of an unit of EG (~44 Da) is appreciable.

This entailed that only the less polar, namely the lightest, could be properly separated from the reaction mixture. In each case, HRMS shows a series of peaks in the shape of a bell curve in which the peaks differ from each other by a value ascribable to the EG fragment (~44 Da, Figure 3.2.5).

The electrochemical properties of the three derivatives F1, F2, and F3 were determined by means of cyclic voltammetry in *o*-DCB/ACN (4:1) at room temperature and the potentials were referenced to ferrocene/ferrocenium (Fc/Fc<sup>+</sup>) redox couple.



**Figure 3.2.6:** Cyclic voltammogram for the several PEG-fullerenes compared to that of pristine C<sub>60</sub>. Reduction potentials were measured in *o*-DCB/ACN (4:1) solution (TBAHFP 0.1M as supporting electrolyte) at room temperature. All potentials are reported with reference to an internal standard of the ferrocene/ferrocenium couple (Fc/Fc<sup>+</sup> = 0.00 V).

The voltammogram of the novel fullerenes and C<sub>60</sub> is shown in Figure 3.2.6. Table 3.2.1 shows the obtained half-wave potentials  $E^{1/2}_{red}$  of the 1<sup>st</sup> reductions, the LUMO and HOMO energies, and the bandgap of the C<sub>60</sub> derivatives. LUMO energies were obtained from the half-wave potentials calculated from the voltammogram, which were subtracted to a standard value of -5.16 eV.

This value can be explained considering that the potential of Fc/Fc<sup>+</sup> in TBAHFP/DCM is 0.46 eV *vs* the saturated calomel electrode SCE,<sup>163</sup> whose potential is 0.244 V *vs* the normal hydrogen electrode (NHE).<sup>164</sup> This has an absolute potential of 4.46 eV *vs* vacuum, which leads to the applied equation:

$$E(\text{HOMO/LUMO}) = -5.16 \text{ eV} - E(\text{oxidation/reduction}).^{165}$$



	$E^{1/2}_{red}$ (eV)	LUMO (eV)	HOMO (eV)	Bandgap (eV)
F1	-1.08	-4.08	-6.93	2.85
F2	-1.16	-4.00	-6.79	2.79
F3	-1.11	-4.05	-6.88	2.83
C <sub>60</sub>	-1.14	-4.02	-7.00	2.98

**Table 3.2.1:** Energy levels and bandgap of PEG-C<sub>60</sub> derivatives

The complete characterization and synthetic procedures of the fullerenes and their precursors can be found at the end of this chapter (Figures 3.2.18-3.2.30).

### 3.2.3 Incorporation of the materials in PSCs

These PEG-C<sub>60</sub> materials are incorporated as additives in regular PSCs in the FTO / compact TiO<sub>2</sub> / mesoporous TiO<sub>2</sub> / MAPbI<sub>3</sub>:fullerene / Spiro-OMeTAD/Au architecture to verify their suitability to both improve the stability and reduce the hysteresis of PSCs.

The perovskite solution was prepared dissolving 1 mmol of PbI<sub>2</sub> in 0.77 ml of DMSO (1.3M), which were then poured into a vial with 1 mmol of MAI (MAI:PbI<sub>2</sub>=1:1 mol/mol).

Additional DMSO was added to obtain a final concentration of 1.2M. The fullerene derivatives were dissolved in DMSO to obtain 0.5 mM solutions, which were added to the MAPbI<sub>3</sub> solution in 9:1 perovskite/PEG-fullerene v/v ratio prior to deposition. The films were deposited through a one-step spin-coating method recurring to an antisolvent, which is one of the most effective strategies so far.<sup>26, 166</sup>

Further characterization of the cells can be found in the last section of this chapter (Figures 3.2.31-3.2.32).

### 3.2.4 PV characterization

The devices were measured using a 450 W xenon light sun simulator under AM 1.5. Figure 3.2.7 shows a summary of the PV parameters obtained with the different MAPbI<sub>3</sub>:PEG-fullerene devices.

While there is just a small variation in both the  $V_{oc}$  and the  $FF$ ,  $J_{sc}$  is rather affected when a fullerene is blended with perovskite (17.8 mA cm<sup>-2</sup> for **F2** and 21.2 mA cm<sup>-2</sup> for the reference device without fullerene additive, respectively), likely due to an increased dilution of the perovskite solution, which led to a difference

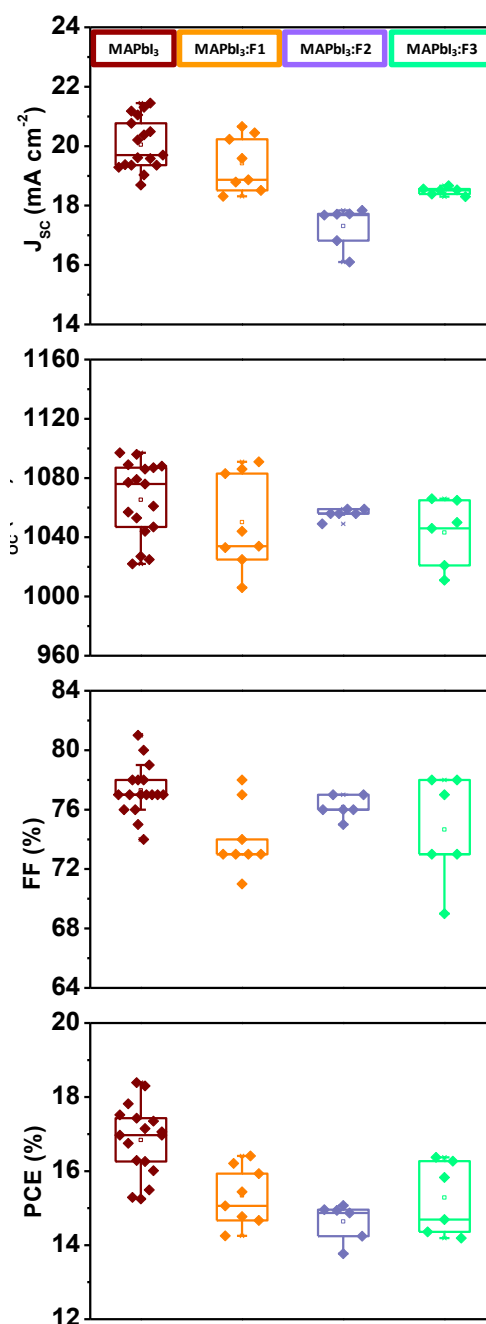


Figure 3.2.7: Statistic of the PV performances of MAPbI<sub>3</sub>:F1 devices (orange), MAPbI<sub>3</sub>:F2 devices (lilac), MAPbI<sub>3</sub>:F3 devices (turquoise), and MAPbI<sub>3</sub> reference (wine).

in crystallization and therefore in the resulting film morphology. The small decrease of  $J_{sc}$  is confirmed by EQE measurements, thus corroborating this hypothesis (Figure 3.2.8 and Table 3.2.2).

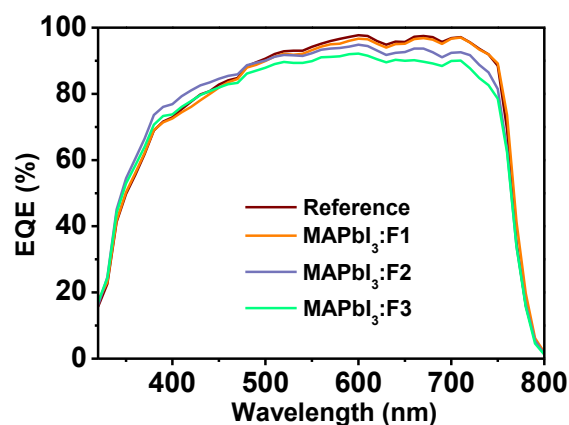


Figure 3.2.8: EQE of the different devices.

Device	$J_{sc}$ (mA cm <sup>-2</sup> )	$J_{sc-EQE}$ (mA cm <sup>-2</sup> )	$V_{oc}$ (V)	$FF$ (%)	$PCE$ (%)
MAPbI <sub>3</sub>	21.2	22.4	1.10	79	18.39
MAPbI <sub>3</sub> :F1	20.7	22.3	1.09	73	16.41
MAPbI <sub>3</sub> :F2	17.8	21.9	1.06	76	15.07
MAPbI <sub>3</sub> :F3	18.5	21.8	1.07	78	16.37

Table 3.2.2: PV parameters of the best devices

Table 3.2.2 shows also the best performances obtained with each one of the different PEG-fullerenes, while the corresponding J-V curves can be seen in Figure 3.2.9). It is worth noting that, even though MAPbI<sub>3</sub>:F2 devices have

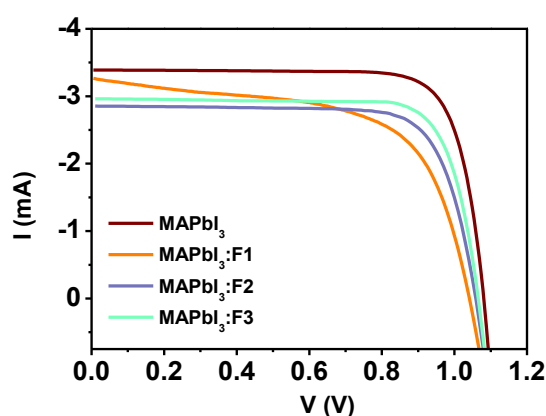


Figure 3.2.9: Best J-V curves of the different fullerene-containing perovskite compared to the fullerene-free reference.

lower efficiencies, they present less spread amongst the considered devices, as shown in Figure 3.2.7. Assuming that the amount of PEG is the reason that leads to the improvement of the performances in Zhao, Wei, Li and co-workers' aforementioned work,<sup>158</sup> it is understandable that this result is not reflected in our study, due to the large difference in concentration. In fact, one of the main differences between the present study and the forerunner lies in the amount of PEG used, which is about 4 orders of magnitude lower in our work. This difference makes a direct comparison quite challenging and complicates the observation of this phenomenon by <sup>1</sup>H-NMR in the present study.

Once it was clear that the introduction of the novel PEG-fullerenes in the perovskite layer did not produce large variation in the PV performances, we evaluated the long-term stability of the devices under different conditions.

### 3.2.5 Stability measurements

As mentioned in the premise, one of the goals of this study was to prove the role of PEG-fullerenes in the protection of the PSCs against humidity.

A preliminary test was performed leaving the cells in a drawer for several days with ambient air and with a relative humidity of ~50%.

The cell performances were measured at the beginning of the experiment and after several days. To avoid the problem of batch-to-batch variations, cells were compared to references belonging to their respective batches (Figure 3.2.10).

The MAPbI<sub>3</sub>:PEG-fullerene cells showed increased stability. In fact, devices containing F1 (Figure 3.2.10 A), F2, and F3 (Figure 3.2.10 B) maintain respectively 97, 81, and 94% of their initial PCE after 13 days.

This is a clear indicator of the effect that these PEG-fullerenes have on MAPbI<sub>3</sub> stability when used as additives, as the reference device experienced a higher drop in efficiency in each and every case. With the purpose to exclude the possibility that the beneficial effect could be just due to the fullerene cage, a saturated solution of C<sub>60</sub> in DMSO was prepared (~0.06 mM) and added to the perovskite solution before processing. The final perovskite solution contained either 5 or 10% v/v of this saturated solution. The extent of the

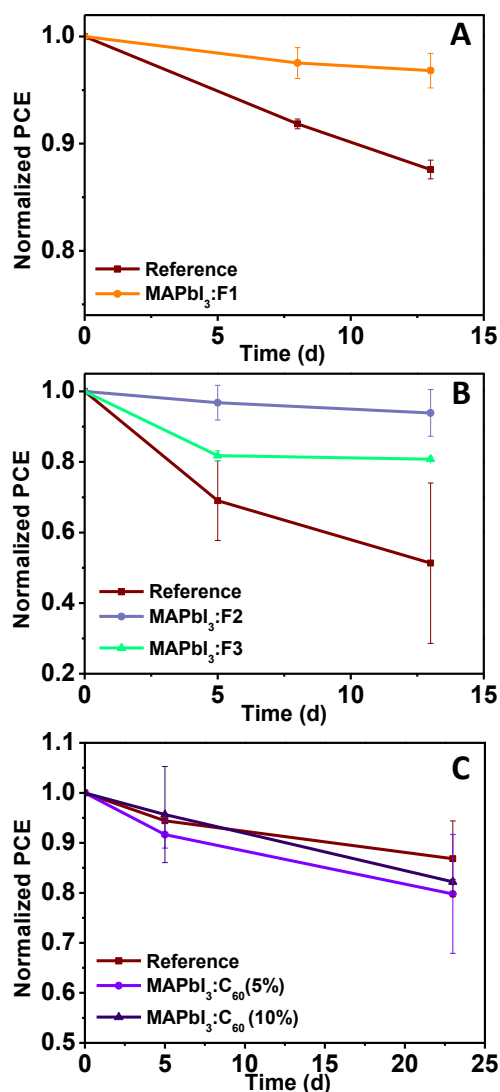
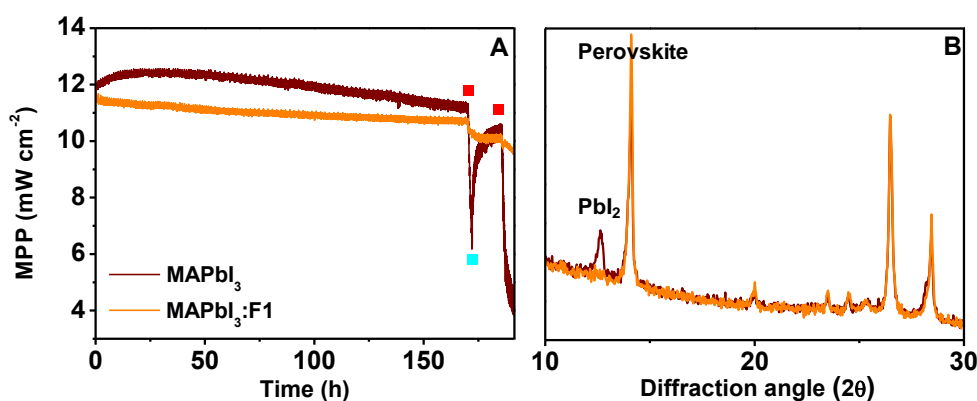


Figure 3.2.10: Normalized PCE of several fullerene-containing devices aged in a drawer. A) F1; B) F2 and F3; C) C<sub>60</sub> 5% and 10%.

degradation while kept in the drawer was almost the same for  $C_{60}$ -containing cells and the reference (Figure 3.2.10 C), most probably because the quantity of  $C_{60}$  was not enough to have a visible effect, even though the difference in concentration was just one order of magnitude lower as in our previous work, where fullerene-containing solar cells showed increased stability.<sup>39</sup>

In light of these preliminary however promising studies, different experiments were planned in order to evaluate the effect of these materials under a more controlled environment, while constantly monitoring maximum power point (MPP) to have a more realistic view of the cell behaviour.

In the first of these studies,  $MAPbI_3:F1$  and  $MAPbI_3$  reference solar cells were left approximately 200 hours under 1 sun, at room temperature, under nitrogen flow, and with constant MPP measurement (Figure 3.2.11 A).



**Figure 3.2.11:** A) MPP trend for  $MAPbI_3:F1$  device with corresponding reference. The red squares indicate the interruption of nitrogen flow, the cyan one shows when the  $N_2$  flow was turned on again. B) X-Ray diffractogram of  $MAPbI_3:F1$  device and corresponding reference after aging experiment.

After 170 hours, when both cells showed good stability, the N<sub>2</sub> flow was interrupted, letting ambient air with ~60% relative humidity diffusing slowly into the chamber. The efficiency of the reference device drastically dropped, while the MAPbI<sub>3</sub>:F1 cell was barely affected. Interestingly, the reintroduction of the N<sub>2</sub> flow allowed the reference to recover, but another cycle led to a non recoverable damage of the cell.

Presumably, this effect is due to the reversible nature of the degradation operated by moisture: with the first interruption of the flow, the volatile degradation products did not have the chance to form and be removed; afterwards, maybe due to the rising temperature, these compounds leave the chamber more easily, thus impeding the recovery. In contrast with what is observed in MAPbI<sub>3</sub> reference solar cells, the MAPbI<sub>3</sub>:F1 device still retains almost its initial efficiency.

Figure 3.2.11 B shows X-Ray diffractograms of the MAPbI<sub>3</sub> reference and the MAPbI<sub>3</sub>:F1 device after the aging experiment. The diffractogram of the reference presents a peak at 12°, typical of PbI<sub>2</sub>, indicating the degradation of the cell while there is no such peak visible in the case of the MAPbI<sub>3</sub>:F1 device, confirming its higher moisture resistance.

A deeper look into the cell parameters revealed that the key parameter in the behaviour of the MAPbI<sub>3</sub>:F1 device is *FF*. In fact, interruption of N<sub>2</sub> flow entails a significant increase in *FF* (Figure 3.2.12 A). Alongside, the hysteresis of the MAPbI<sub>3</sub> reference device

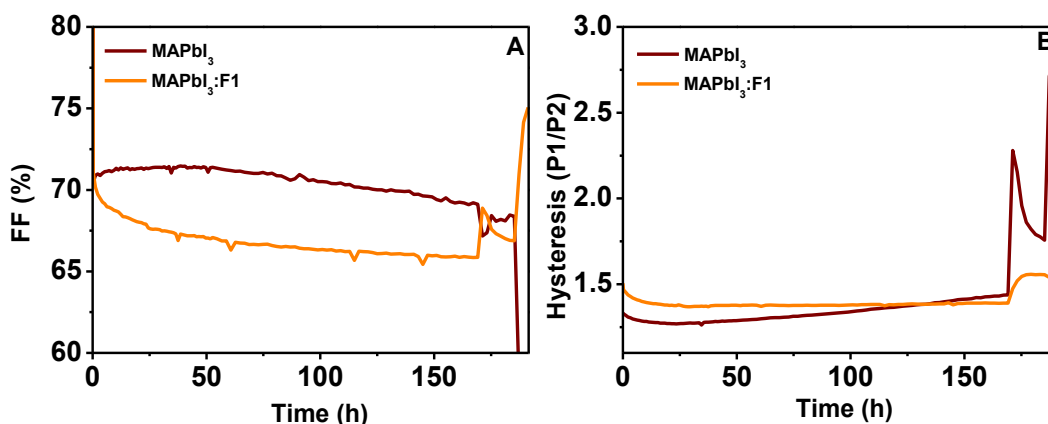


Figure 3.2.12: A) FF trend for MAPbI<sub>3</sub>:F1 device with corresponding reference throughout the aging test. B) Hysteresis trend for MAPbI<sub>3</sub>:F1 device with corresponding reference throughout the aging test.

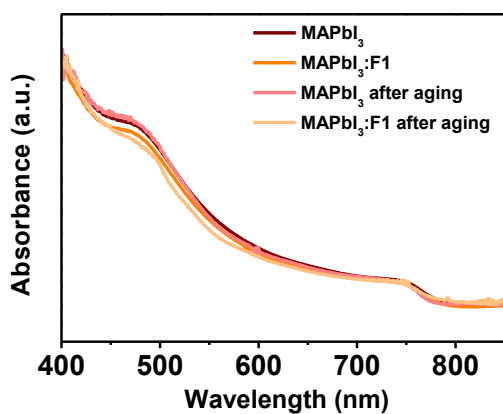


Figure 3.2.13: UV-Vis spectra of MAPbI<sub>3</sub> and MAPbI<sub>3</sub>:F1 before and after aging.

increases abruptly when the N<sub>2</sub> flow is interrupted (Figure 3.2.12 B). When hysteresis is considered as the ratio between the backward scan P1 and the forward scan P2,

a value the closest to 1 is highly desirable, meaning the lowest difference between the two registered curves.

Finally, UV-Vis spectra of the cells after and before the aging process show that the absorption remains quite unmodified (Figure 3.2.13). A similar study was performed on MAPbI<sub>3</sub>:F2 devices, again compared to a MAPbI<sub>3</sub> reference. Both underwent several cycles of N<sub>2</sub> flow / no flow / air with 5% relative humidity, while laying under 1 Sun at room temperature. Also in this case, their parameters were



monitored constantly (Figure 3.2.14 A). Every N<sub>2</sub> flow interruption meant a strong decrease in the performance of the reference, intensified by the introduction of air. Also the MAPbI<sub>3</sub>:F2 device

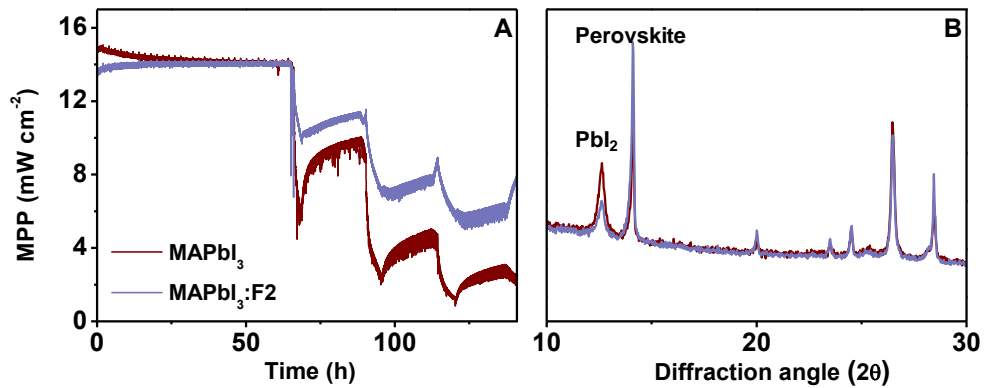


Figure 3.2.14: A) MPP trend for MAPbI<sub>3</sub>:F2 device with corresponding reference. B) X-Ray diffractogram of MAPbI<sub>3</sub>:F2 device and corresponding reference after aging experiment.

suffered from the introduction of air, however to a lesser extent. The subsequent introduction of N<sub>2</sub> flow partially restored the cells' performances. At the end of the experiment, MAPbI<sub>3</sub>:F2 still retained half of the original efficiency at the end of these cycles (140h), unlike the reference, which was strongly affected by the process.

In contrary to the prior experiment, the X-Ray diffractograms of the aged devices of both the reference and MAPbI<sub>3</sub>:F2 perovskite have a PbI<sub>2</sub> peak at 12°, even though with different intensity with respect to the corresponding perovskite peak at 14°. This confirmed once more that the reference degraded more than the MAPbI<sub>3</sub>:PEG-fullerene device (Figure 3.2.14 B).

Also in this case, *FF* plays a leading role. The drop in the *FF* of MAPbI<sub>3</sub> reference is more relevant than that of MAPbI<sub>3</sub>:F2 device (Figure 3.2.15 A). Hysteresis, as before, increases faster in the MAPbI<sub>3</sub> reference (Figure 3.2.15 B).

The lower stability of the MAPbI<sub>3</sub>:F2 device with respect to MAPbI<sub>3</sub>:F1 one might be due to the different amount of oxygen

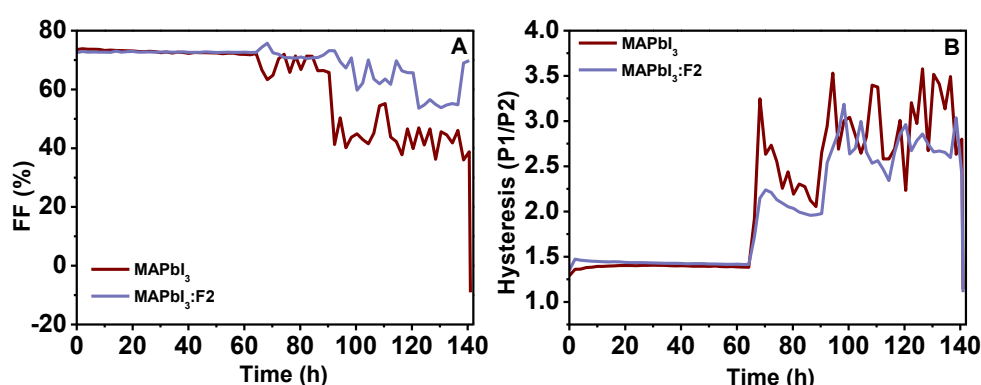


Figure 3.2.15: A) *FF* trend for MAPbI<sub>3</sub>:F1 device with corresponding reference throughout the aging test. B) Hysteresis trend for MAPbI<sub>3</sub>:F1 device with corresponding reference throughout the aging test.

introduced (induced flow in the case of MAPbI<sub>3</sub>:F2 *vs* spontaneous diffusion as in the case of MAPbI<sub>3</sub>:F1) but it might also be due to the

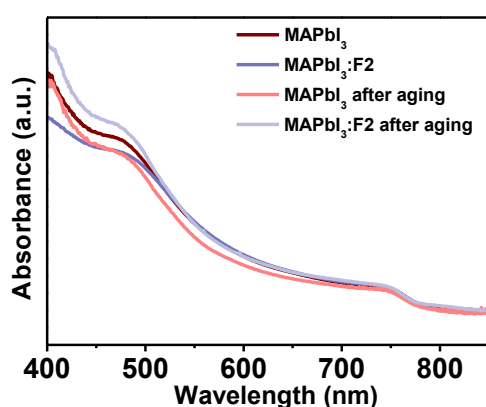


Figure 3.2.16: UV-Vis spectra of MAPbI<sub>3</sub> and MAPbI<sub>3</sub>:F2 before and after aging.

dissimilar amount of PEG chains per mole, as F1 carries two PEG chains instead of one like in the case of F2. Figure 3.2.16 shows the UV-Vis spectra of the cells after and before aging. In similarity to the prior experiment the absorption remains the same

for both devices. In each of the analyzed cases, we noticed an increase of the stability of the perovskite devices once the PEG-C<sub>60</sub> is incorporated. This effect should not be attributed to the fullerene cage only, because the same stabilizing effect was not observed in preliminary tests considering C<sub>60</sub>-containing devices.

This means that even a low-MW PEG chain as the one considered in this study can potentially improve the long-term performances of PSCs. The fact that mainly the *FF* and hysteresis are affected, while the absorption remains rather unmodified, indicates that the stabilizing effect of the PEG involves mainly the charge extraction processes. Presumably, the recombination rate increases to a greater extent for MAPbI<sub>3</sub> devices than for MAPbI<sub>3</sub>:PEG fullerene ones, and this is known to affect fill factor. The raise of the concentration of trap states could explain the drop in *FF* and the exacerbation of the hysteresis.<sup>167</sup> It is possible that the insulating nature of PEG delays the formation of these trap states, in addition to the blocking of the H<sub>2</sub>O molecules within its branches.

### 3.2.6 Hysteresis measurements

The phenomenon of hysteresis is one of the major drawbacks of PSCs. A large hysteresis leads to errors in the evaluation of PV performance and this could jeopardize industrial applications. Studies involving C<sub>60</sub> showed a beneficial effect towards the phenomenon, due to passivation of trap states.<sup>62, 63, 92</sup> Hysteresis was studied measuring current density-voltage (*J-V*) curves forwards and backwards under the same conditions (AM 1.5, 10 mV s<sup>-1</sup>).

The hysteresis phenomenon is notably reduced in every MAPbI<sub>3</sub>:PEG-fullerene device, as can be seen in Figure 3.2.17, where the statistics of hysteresis measurements for several MAPbI<sub>3</sub> references and MAPbI<sub>3</sub>:PEG-fullerene devices are reported.

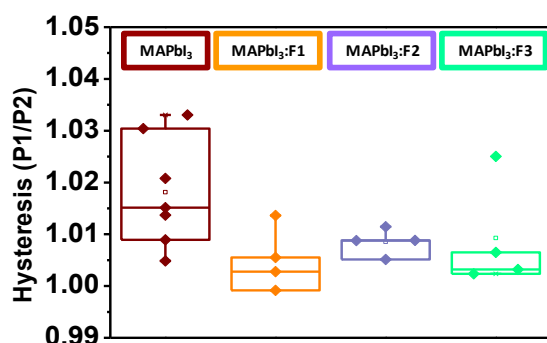


Figure 3.2.17: Statistics of hysteresis of different MAPbI<sub>3</sub>:PEG-fullerene devices. P1 is the efficiency of the backward scan and P2 of the forward scan with a scan rate of 10 mV s<sup>-1</sup>.

The degree of reduction of hysteresis is highly comparable to what could be found in literature.<sup>168, 169</sup> In particular, with respect to the latter, the amount of fullerene used is notably lower ( $\sim 10^{-5}$

mol/mol with respect to perovskite). We also analyzed the hysteresis of devices containing 5% or 10% of pristine C<sub>60</sub>. In similarity to the moisture stability experiments it seems that concentration of C<sub>60</sub> is not high enough to show a significant effect on the hysteresis, even though the saturated solution concentration is just one magnitude lower compared to the PEG-fullerene concentrations. Examples of the hysteresis curves of devices containing all the considered fullerenes can be found at the end of this chapter.

To sum up, a family of three novel PEG-fullerenes (**F1**, **F2**, and **F3**) was successfully synthesized and characterized. These molecules were introduced into PSCs in small amounts ( $\sim 10^{-5}$  mol/mol with

respect to perovskite) without resorting to co-solvents, which help solubilising the fullerene into the perovskite solution, but could affect the way perovskite crystallizes. MAPbI<sub>3</sub>:PEG-fullerene devices showed increased stability with respect to reference devices, retaining 97, 81 and 94% of the original performances respectively after 13 days of exposure to ambient atmosphere, outperforming the reference in every case. This is most likely due to the hygroscopicity of PEG chains, which help with retention of water, thus preventing perovskite from degrading. In addition, the phenomenon of hysteresis is reduced due to the presence of the fullerene cage.

### 3.2.7 Materials and Methods

#### Reagents, Solvents, and Other Materials

Chemicals and reagents for synthesis were purchased from commercial suppliers and used as received. Air-sensitive reactions were carried out under argon atmosphere. Flash chromatography was performed using silica gel (40-60 $\mu$ , Acros Organics). Analytical thin layer chromatography (TLC) was performed using aluminum coated Macherey Nagel<sup>TM</sup> Standard SIL G Silica Layers on Alugram<sup>TM</sup> Aluminum Sheets UV254. The materials used in the PV study were obtained from commercial suppliers in high purity and used without further purification: glass/FTO (Nippon Sheet Glass), methylammonium iodide (MAI, DYESOL), PbI<sub>2</sub> (99.99%, TCI chemicals), spiro-OMeTAD (Solarpur), lithium bis(trifluoromethane) sulfonimide (LiTFSI, 99.9%, Sigma-Aldrich), *tert*-butylpyridine

(96%, Sigma–Aldrich), tris(2-(1*H*-pyrazol-1-yl)-4-*tert*-butylpyridine)cobalt(III) tri[bis(trifluoromethane)sulfonimide] (FK 209, Dyenamo), TiO<sub>2</sub> paste (Dyesol 30 NR-D), titanium diisopropoxide bis(acetylacetonate) (Acros Organics), acetylacetone (Acros Organics), DMSO (extra dry, Acros Organics), acetone (technical grade, Scharlab), chlorobenzene (extra dry, Acros Organics) and acetonitrile (extra dry, Acros Organics), DMF (extra dry, Acros Organics), EtOH (Acros Organics).

### Material Characterization

NMR spectra were recorded on a Bruker Advance 300 (<sup>1</sup>H: 300 MHz; <sup>13</sup>C: 75 MHz) spectrometer at 298 K using partially deuterated solvents as internal standards. Chemical shifts ( $\delta$ ) are denoted in ppm. Multiplicities are denoted as follows: s = singlet, d = doublet, t = triplet, m = multiplet, dd = doublet of doublets.

UV-Vis spectra were recorded in a Varian Cary 50 spectrophotometer. High Resolution Matrix Assisted Laser Desorption Ionization (coupled to a Time-Of-Flight analyzer) experiments (MALDI-TOF) were performed on a Bruker Ultraflex III. Electrochemical measurements were carried out on a Princeton Applied Research Parstat 2273 in a 3-electrode single compartment cell with platinum working electrode ( $\varnothing = 0.5$  mm), a platinum wire counter electrode ( $\varnothing = 0.5$  mm) and a Ag/AgNO<sub>3</sub> wire pseudoreference electrode.

Cyclic voltammograms were recorded at a scan rate of 100 mV s<sup>-1</sup>. Reduction potentials were measured in o-DCB/ACN (4:1) solution

(Bu<sub>4</sub>NPF<sub>6</sub> 0.1M as supporting electrolyte) at room temperature. All potentials are reported with reference to the internal standard of the ferrocene/ferrocenium couple (Fc/Fc<sup>+</sup> = 0.00 V).

#### Device Fabrication

FTO/Glass 10 Ω/sq was cleaned by sonication in 2% Hellmanex water solution for 15 minutes. After rinsing with deionised water, the substrates were further sonicated with ethanol for another 15 minutes and, after drying, with acetone for the same amount of time. After a 15-minute UV-ozone treatment, a TiO<sub>2</sub> compact layer was deposited on FTO via spray pyrolysis at 450 °C from a precursor solution of titanium diisopropoxide bis(acetylacetonate) and acetylacetonate in ethanol. After spraying, the substrates were left at 450 °C for 30 minutes and left to cool down to room temperature. Then, mesoporous TiO<sub>2</sub> layer was deposited by spin coating for 10 s at 4000 rpm with a ramp of 2000 rpm s<sup>-1</sup>, using 30 nm particle paste diluted in ethanol (150 mg ml<sup>-1</sup>) to achieve 150-200 nm thick layer. After the spin coating, the substrates were sintered with a heating ramp up to 450 °C, at which they were left for 30 minutes under dry air flow. Li-doping of mesoporous TiO<sub>2</sub> is obtained by spin coating a 10 mg ml<sup>-1</sup> solution of Li-TFSI in acetonitrile at 3000 rpm for 10 s. The substrate with Li-doped mesoporous TiO<sub>2</sub> was completed with a second sintering process, the same as before. After cooling down to 150 °C the substrates were immediately transferred in a nitrogen atmosphere glove box for deposition of the perovskite films.

The perovskite films were deposited from a freshly prepared precursor solution, containing  $\text{PbI}_2$ :MAI, 1:1 mol/mol, 1.2 M in anhydrous DMSO, and either 0 or 10% v/v of each fullerene (0.5 mmol in anhydrous DMSO). The perovskite solution was spin coated using a two-part program at 1000 and 6000 rpm for 10 and 30 s respectively. During the second part, 150  $\mu\text{l}$  of chlorobenzene were dripped onto the spinning substrate 5 s prior the end of the program. The substrates were then annealed at 100°C for 30 minutes in a nitrogen filled glove box.

After the perovskite annealing the substrates were cooled down for few minutes and 50  $\mu\text{l}$  Spiro-OMeTAD solution (70 mmol in chlorobenzene) were spun at 4000 rpm for 20 s. The HTM solution was doped with *tert*-butyl pyridine (3.3 mol/mol with respect to Spiro), LiTFSI (1.8 M in acetonitrile, 0.5 mol/mol with respect to Spiro) and FK209 (0.25 M in acetonitrile, 0.05 mol/mol with respect to Spiro). Finally, a 80 nm gold top electrode was thermally evaporated using a Leica EM MED020 evaporator, under around  $2 \cdot 10^{-5}$  Torr, through an appropriate shadow mask (0.25  $\text{cm}^2$  pixel).

### Device Characterization

X-Ray diffraction measurements have been performed on an Empyrean system (Theta-Theta, 240mm) equipped with a PIXcel-1D detector, Bragg-Brentano beam optics and parallel beam optics. The Reflection-Transmission spinner is combined with a sample changer with a maximum of 45 samples.



Scanning electron microscopy (SEM) was performed on a ZEISS Merlin HR-SEM.

UV/Vis absorption data was collected using a Perkin-Elmer Lambda 950 spectrophotometer.

Steady-state photoluminescence spectra were recorded by exciting the samples at 450 nm with a 450-W Xenon CW lamp. The signal was recorded with a spectrofluorometer (Fluorolog; Horiba Jobin Yvon Technology FL1065).

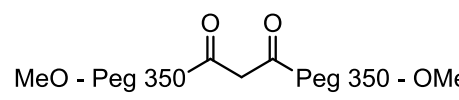
The solar cells performances were measured using a 450 W xenon light source (Oriel). The light intensity was calibrated with a Si photodiode equipped with an IR-cutoff filter (KG3, Schott) and it was recorded during each measurement. Current-voltage characteristics of the cells were obtained by applying an external voltage bias while measuring the current response with a digital source meter (Keithley 2400). The employed voltage scan rate was 10 mV s<sup>-1</sup> and no device preconditioning was applied before starting the measurement, such as light soaking or forward voltage bias applied for long time. The starting voltage was determined as the potential at which the cells furnish 1 mA in forward bias. No equilibration time was used. The cells were masked with a black metal mask (0.16 cm<sup>2</sup>) to estimate the active area and reduce the influence of the scattered light.

Aging under maximum power point tracking was carried out on masked devices which were mounted on a temperature controlled plate. The aging was mainly performed under nitrogen atmosphere,

sometimes alternating with dry air or spontaneous flow of ambient air, and 1-Sun equivalent illumination provided by an array of white LEDs. The devices were aged keeping them under maximum load under illumination. The maximum power point was updated every 10 s by measuring the current response to a small perturbation in potential. Additionally, a full  $J$ - $V$  scan was taken every 120 minutes (at a scan rate of  $100 \text{ mV s}^{-1}$  starting from forward bias) which was used to extract the displayed parameters for the aging data.

### Synthetic procedures and compound characterization

#### 1


 350K-PEG methyl ether (1.68 g, 4.80 mmol) was dissolved in DCM (10 ml). Malonyl chloride (280  $\mu\text{l}$ , 2.30 mmol) was added and the mixture was cooled to  $0^\circ\text{C}$ .  $\text{NEt}_3$  (800  $\mu\text{l}$ , 5.75 mmol) was then added. The mixture was left to warm to room temperature and stirred for 72 h.  $\text{H}_2\text{O}$  (5 ml) was added and the mixture was extracted with DCM ( $5 \times 10 \text{ ml}$ ). The mixture was purified by column chromatography (DCM:MeOH 15:1 + 1%  $\text{NEt}_3$ ) to obtain the final product **1** (orange oil, 1.37 g, 1.74 mmol, yield: 76%).

$^1\text{H NMR}$  (300.2 MHz,  $\text{DCM-}d_2$ ):  $\delta$  [ppm] = 4.26 (m, 4H), 3.67 (m, 4H), 3.62–3.54 (PEG chain), 3.49 (m, 4H), 3.44 (s, 2H), 3.32 (s, 6H).

$^{13}\text{C NMR}$  (75.5 MHz,  $\text{DCM-}d_2$ )  $\delta$  [ppm] = 166.9, 72.2, 70.8, 70.7, 69.1, 65.0, 58.9, 41.6.

**HRMS** [m/z] = 772.3167, 816.3990 (Main peak: M+Na<sup>+</sup>, 15 EG units. Peaks with more or less EG units are observable, being the gap between the peaks of 44 Da), 860.4819.

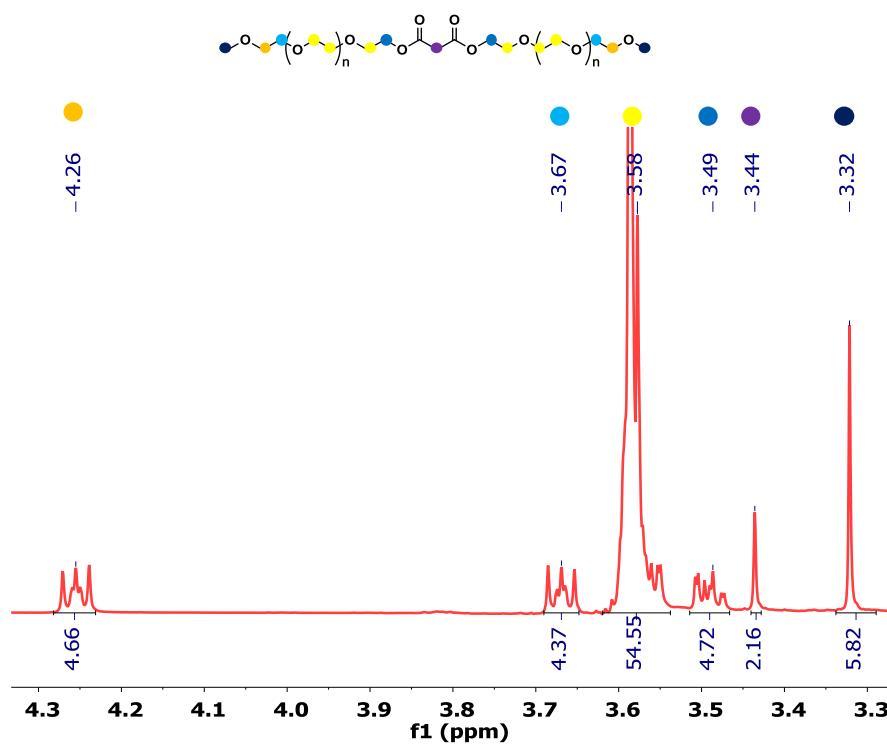
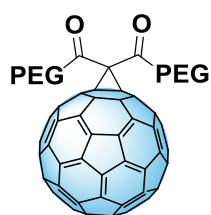


Figure 3.2.18: <sup>1</sup>H NMR spectrum of 1 in DCM

**F1**



1 (157mg, 0.200 mmol), C<sub>60</sub> (144.0 mg, 0.200 mmol) and I<sub>2</sub> (51.0 mg, 0.200 mmol) were dissolved under inert atmosphere in dry Tol (5 ml) and 1, 5-

diazabicyclo[5.4.0]undec-5-ene (DBU, 76.1 mg, 0.500 mmol) was added dropwise. The mixture was left stirring for 12 h at room temperature and was then purified by column chromatography (Tol:*i*-PrOH, 1:0→1:1) to obtain product F1 (dark red solid, 42.9 mg, 0.030 mmol, yield: 14%).

**<sup>1</sup>H NMR** (300.2 MHz, DCM-*d*<sub>2</sub>):  $\delta$  [ppm] = 4.63 (m, 4H), 3.85 (m, 4H), 3.68–3.45 (PEG chain), 3.32 (s, 6H).

**<sup>13</sup>C NMR** (75.5 MHz, DCM-*d*<sub>2</sub>):  $\delta$  [ppm] = 164.0, 146.0–139.7 (fullerene cage), 72.5, 71.3, 71.2, 71.1, 69.3, 67.0, 59.2, 52.8.

**IR** (neat):  $\tilde{\nu}$  [cm<sup>-1</sup>] = 1743, 1452, 1229, 1098, 702, 524.

**UV-Vis** [nm] = 426, 686.

**HRMS** [m/z]: 1268.8717, 1312.9596, 1357.0589, 1401.1538 (Main peak: M+Na<sup>+</sup>, 12 EG units), 1445.2447. Peaks with more or less EG units are observable, being the gap between the peaks of 44 Da.

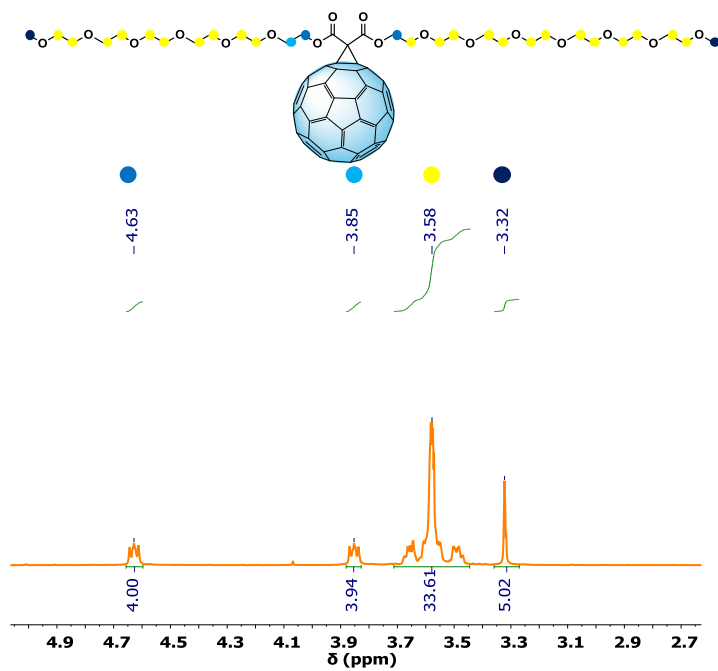


Figure 3.2.19: <sup>1</sup>H NMR spectrum of F1 in DCM

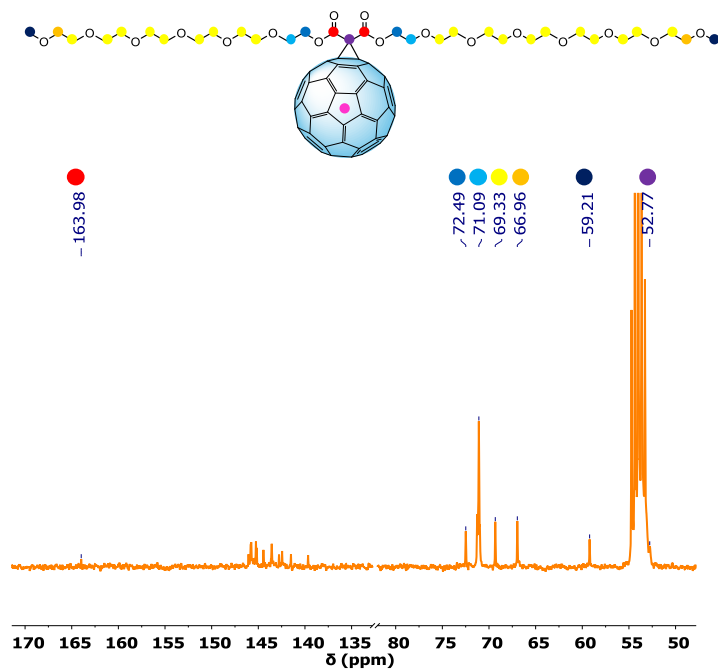


Figure 3.2.20: <sup>13</sup>C NMR spectrum of F1 in DCM

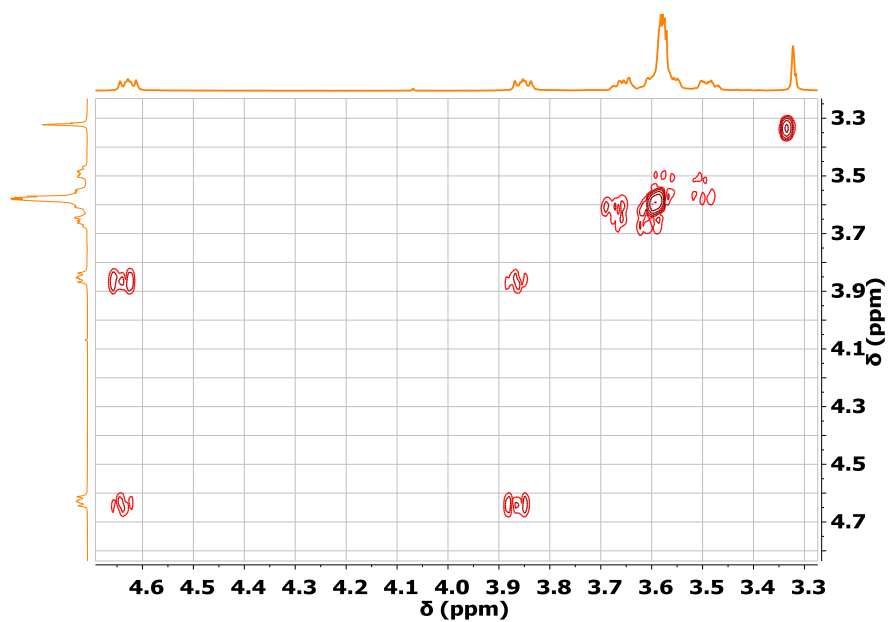


Figure 3.2.21:  $^1\text{H}$ - $^1\text{H}$  COSY spectrum of F1 in DCM

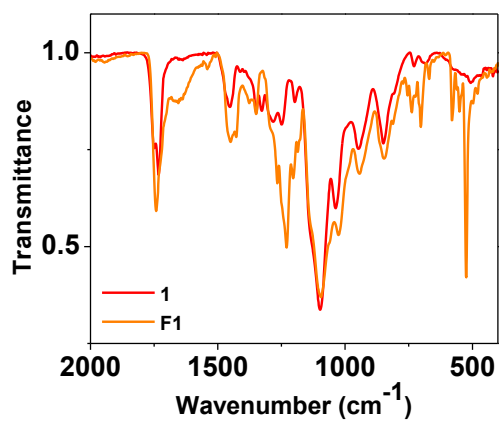
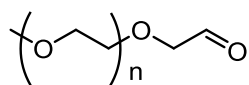


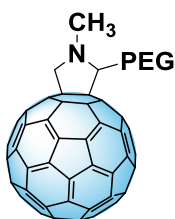
Figure 3.2.22: ATR spectra of F1 vs 1

**2**

Oxalyl chloride (940  $\mu$ l, 11.0 mmol) was dissolved in DCM (25 ml) and the solution was cooled to  $-78^{\circ}\text{C}$ . A mixture of DMSO (1.7 ml) and DCM (5 ml) was added dropwise and the resulting mixture was stirred for 30 minutes. 350K-PEG methyl ether (3.50 g, 10.0 mmol) was dissolved in DCM (10 ml) and added dropwise to the previous mixture, which was left stirring for further 15 minutes at  $-78^{\circ}\text{C}$ . Subsequently,  $\text{NEt}_3$  (7 ml, 50.0 mmol) was added dropwise and the mixture was left warming up to room temperature.  $\text{H}_2\text{O}$  (30 ml) was added and the water phase was extracted with DCM ( $2 \times 20$  ml). The resulting mixture was washed with diluted HCl (20 ml),  $\text{H}_2\text{O}$  (20 ml),  $\text{Na}_2\text{CO}_3$  (20 ml), and again with  $\text{H}_2\text{O}$  (20 ml). After drying over  $\text{Na}_2\text{SO}_4$ , the solvent was evaporated and the mixture was further purified by column chromatography (EtOAc:MeOH 9:1) to get product **2** (pale yellow oil, 647 mg, 1.78 mmol, yield: 18%).

$^1\text{H NMR}$  (300.2 MHz,  $\text{DCM-}d_2$ ):  $\delta$  [ppm] = 9.70 (s, 1H), 4.49 (s, 2H), 3.70–3.45 (PEG chain), 3.38 (s, 3H).

Complete characterization can be found in literature.<sup>170</sup>

**F2**

**2** (91.0 mg, 0.250 mmol) and C<sub>60</sub> (180 mg, 0.250 mmol) were dissolved in *o*-DCB (130 ml). Sarcosine (89.1 mg, 0.500 mmol) was added to the mixture, which was then heated to reflux for 30 minutes, while monitoring by thin layer chromatography. The mixture was then separated by column chromatography (Tol:MeOH, 1:0→95:5) to get the product **F2** (dark brown solid, 124 mg, 0.110 mmol, yield: 42%).

<sup>1</sup>H NMR (300.2 MHz, DCM-*d*<sub>2</sub>): δ [ppm] = 4.78 (d, 1H), 4.54–4.48 (dd, 1H), 4.38–4.33 (1H), 4.13 (d, 1H), 4.08 (t, 1H), 3.72–3.45 (PEG chain), 3.32 (s, 3H), 2.96 (s, 3H).

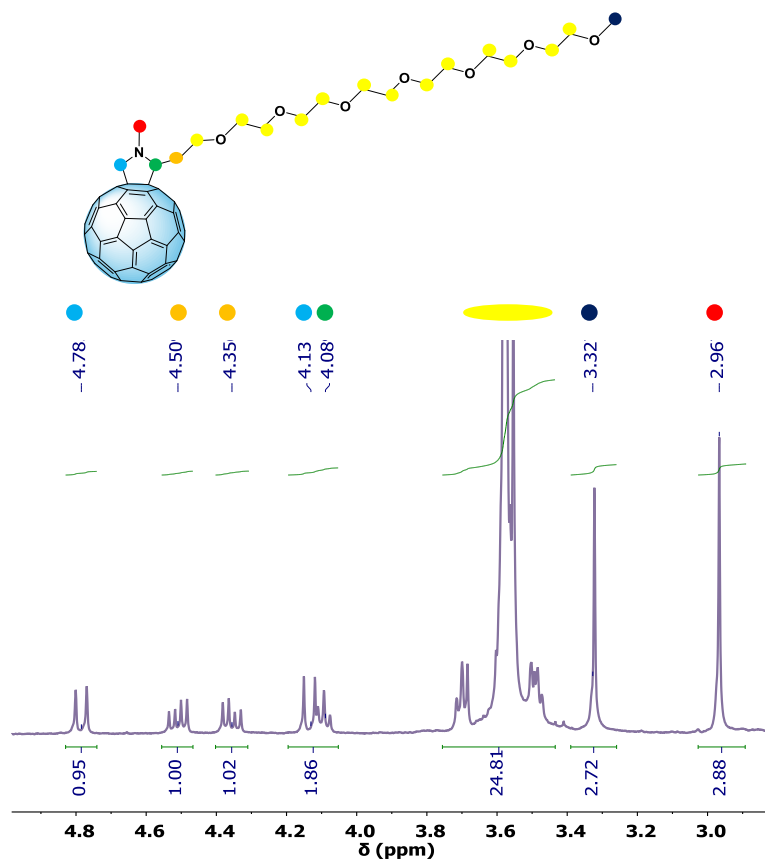
<sup>13</sup>C NMR (75.5 MHz, DCM-*d*<sub>2</sub>): δ [ppm] = 147–140 (fullerene cage), 76.8, 72.5, 72.3, 71.6, 71.1, 59.2, 40.7.

IR (neat):  $\tilde{\nu}$  [cm<sup>-1</sup>] = 1671, 1093, 766, 524.

UV-Vis [nm] = 431, 701.

HRMS (m/z) = 1041.7779, 1085.8716, 1129.9612 (Main peak, M<sup>+</sup>), 1174.0597.



Figure 3.2.23: <sup>1</sup>H NMR spectrum of F2 in DCM

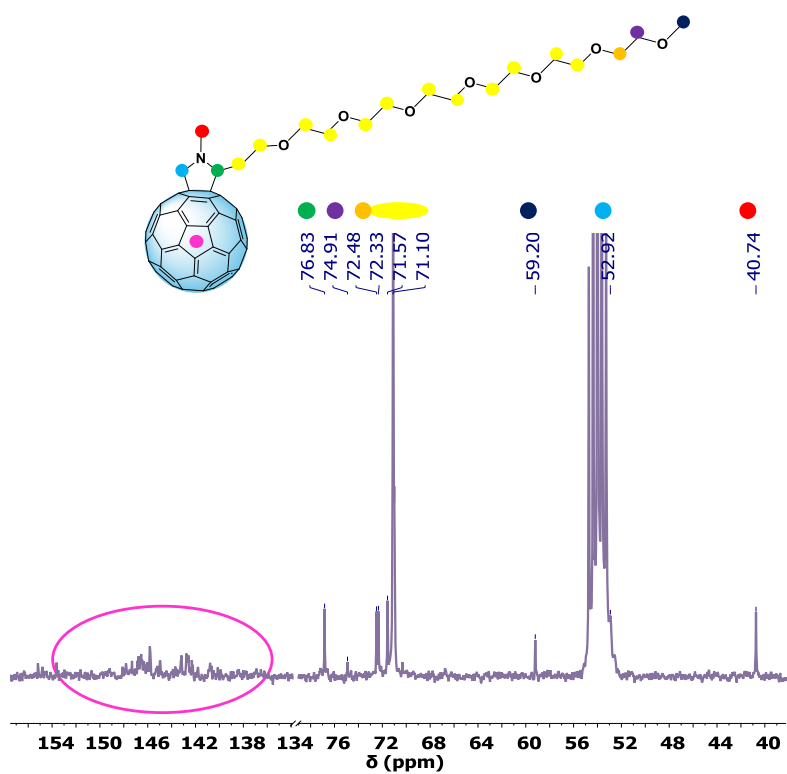


Figure 3.2.24:  $^{13}\text{C}$  NMR spectrum of F2 in DCM

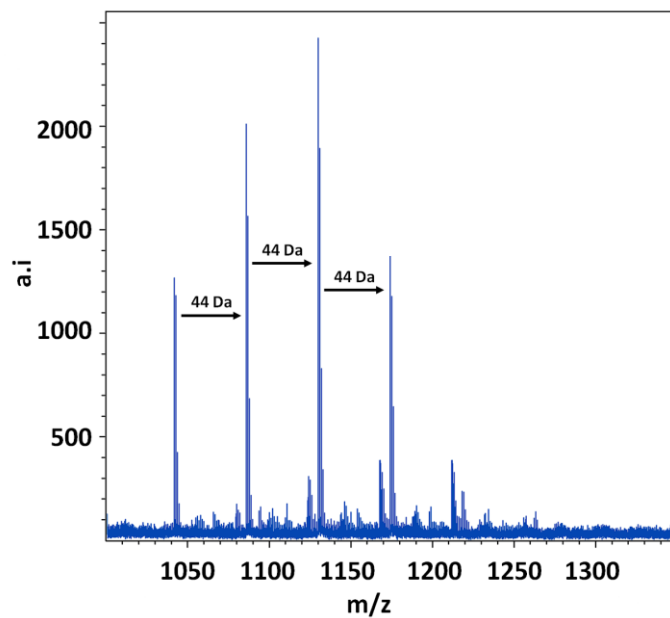


Figure 3.2.25: High Resolution MALDI-TOF for F2

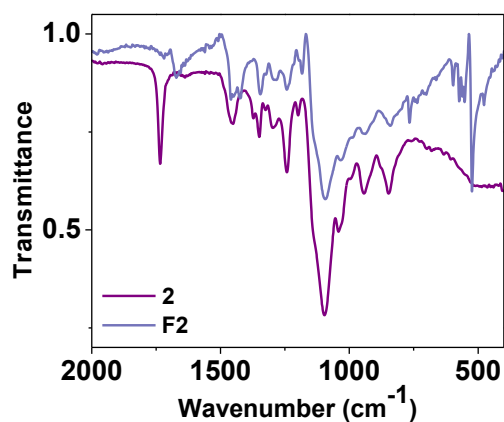
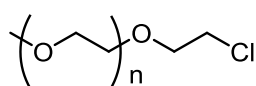


Figure 3.2.26: ATR spectra of F2 vs 2

3

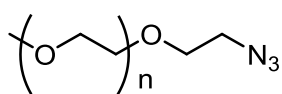


A solution of thionyl chloride (363  $\mu$ l, 5.00 mmol) in dry Tol (2 ml) was added dropwise to a solution of 350K-PEG methyl ether (1.05 g, 3.00 mmol) in dry Tol (50 ml) under N<sub>2</sub> atmosphere. The reaction mixture was refluxed for 6 h, after which the mixture was cooled and evaporated to dryness under reduced pressure to remove residual traces of thionyl chloride. Dry Tol (20 ml) was added to completely dissolve the product, which was then precipitated in excess Et<sub>2</sub>O to obtain product **3** (pale yellow oil, 1.00 g, 2.73 mmol, yield: 91%).

<sup>1</sup>H NMR (300.2 MHz, DCM-*d*<sub>2</sub>):  $\delta$  [ppm] = 3.97 (t, *J* = 7.1 Hz, 2H), 3.79 (t, *J* = 7.1 Hz, 2H) 3.76–3.42 (PEG chain), 3.34 (s, 3H).

Complete characterization can be found in literature.<sup>171</sup>

4

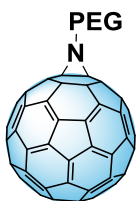


**3** (184 mg, 0.500 mmol), NaN<sub>3</sub> (218 mg, 3.35 mmol), and TBAI (11 mg, 0.030 mmol) were dissolved in DMF (5 ml) under inert atmosphere. The mixture was heated to 65°C and left stirring for 12 h. After the solvent was removed under reduced pressure, the remaining solid was washed first with CHCl<sub>3</sub> (10 ml) and then with Tol (10 ml) to obtain product **4** (pale yellow oil, 132 mg, 0.350 mmol, yield: 70%).

<sup>1</sup>H NMR (300.2 MHz, DCM-*d*<sub>2</sub>): δ [ppm] = 3.76–3.42 (PEG chain), 3.40 (t, *J* = 7.0 Hz, 2H), 3.34 (s, 3H), 1.98 (t, *J* = 6.9 Hz, 2H).

Complete characterization can be found in literature.<sup>172</sup>

F3



A solution of **4** (127 mg, 0.340 mmol) in *o*-DCB (5 ml) was added dropwise to a solution of C<sub>60</sub> (269 mg, 0.370 mmol) in *o*-DCB (75 ml). The mixture was refluxed for 24 h, after which the solvent was removed under reduced pressure. The residue was dissolved in THF (15 ml) and the mixture was further stirred for further 12 hours at room temperature. Product **F3** (dark brown solid, 68.1 mg, 0.060 mmol, yield: 19%) was isolated through column chromatography (Tol:MeOH, 1:0→9:1).

<sup>1</sup>H NMR (300.2 MHz, DCM-*d*<sub>2</sub>): δ [ppm] = 3.85–3.38 (PEG chain), 3.32 (s, 3H).

<sup>13</sup>C NMR (75.5 MHz, DCM-*d*<sub>2</sub>):  $\delta$  [ppm] = 149–142 (fullerene cage)  
72.5, 71.1, 59.2, 30.3.

IR (neat):  $\tilde{\nu}$  [cm<sup>-1</sup>] = 3300, 1676, 1447, 1094, 728, 522.

HRMS [m/z] = 1113.7874, 1157.8837 (Main peak), 1201.9371. Several groups of signals with the typical PEG pattern can be identified, due to the equilibrium between open and closed forms of this compound and the high reactivity of the open one.

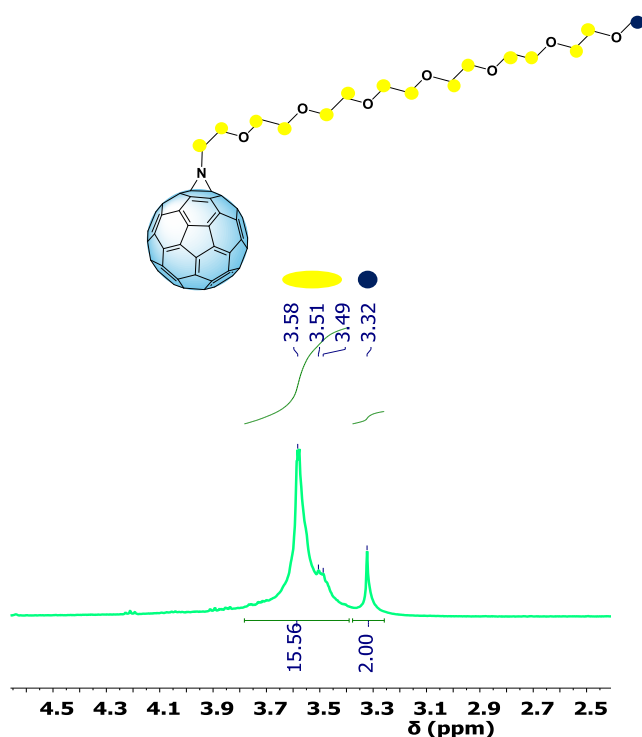


Figure 3.2.27: <sup>1</sup>H NMR spectrum of F3 in DCM

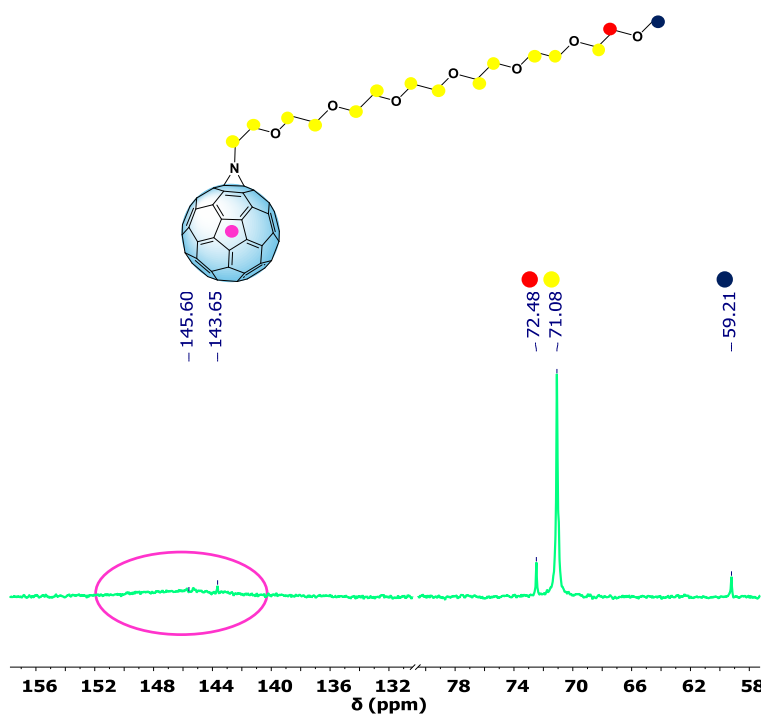


Figure 3.2.28:  $^{13}\text{C}$  NMR spectrum of F3 in DCM

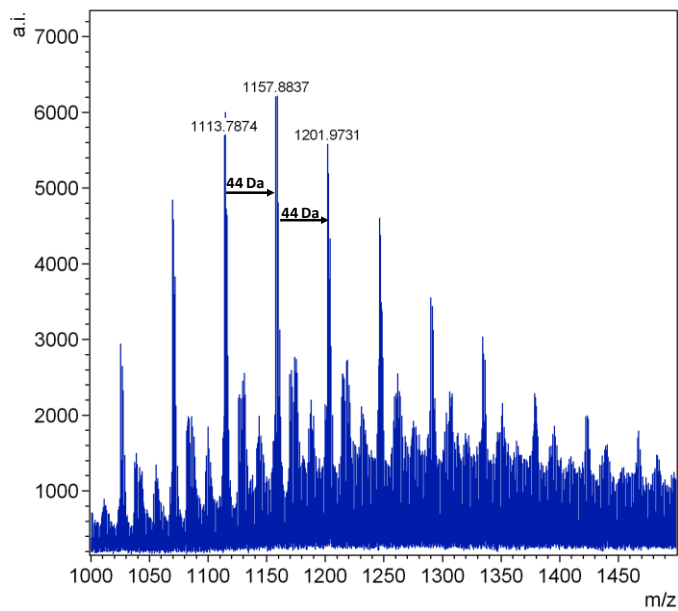


Figure 3.2.29: HRMS-F3 High Resolution MALDI-TOF for F3

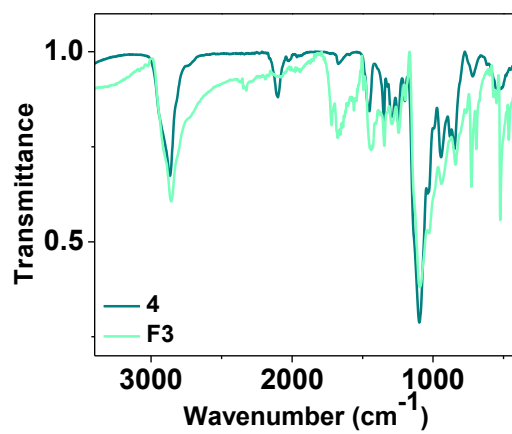


Figure 3.2.30: ATR spectra of F3 *vs* 4

Device characterization: additional graphs

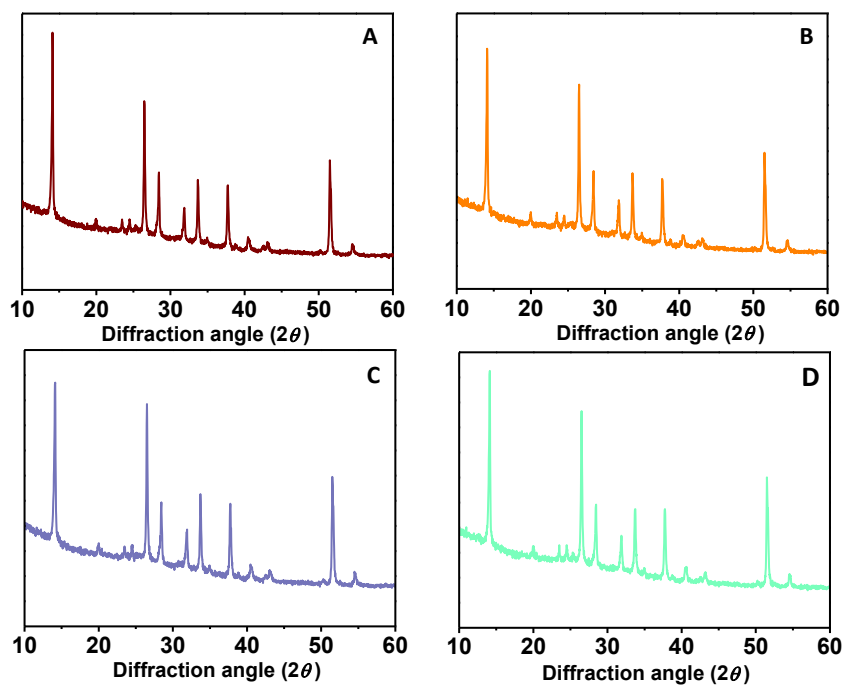


Figure 3.2.31: X-Ray Diffractograms of: A) MAPbI<sub>3</sub> reference device, B) MAPbI<sub>3</sub>:F1 device, C) MAPbI<sub>3</sub>:F2 device, D) MAPbI<sub>3</sub>:F3 device.

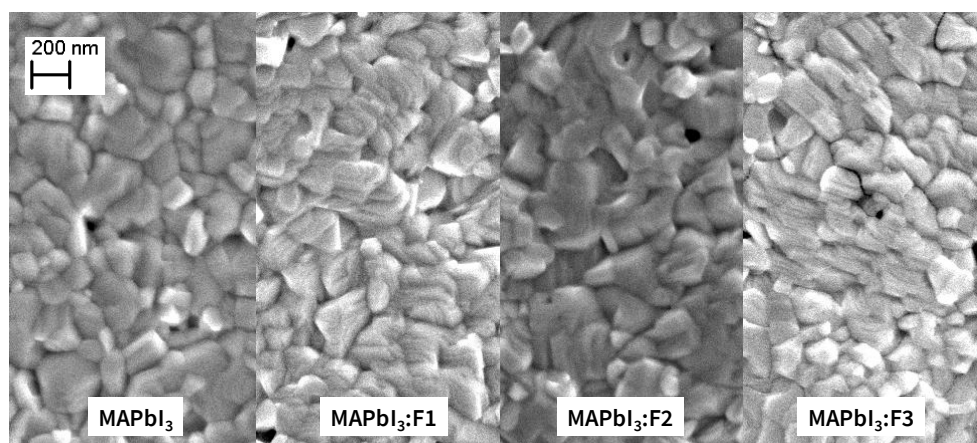


Figure 3.2.32: Top View SEM images of the different devices.



### 3.3 Innovative HTMs containing a C<sub>60</sub> core

#### 3.3.1 Preamble

Fullerenes and their monoadduct derivatives, such as **PC<sub>61</sub>BM**, display a suitable LUMO level (−4.3 for C<sub>60</sub> and −4.2 eV for **PC<sub>61</sub>BM**) to act as good ETMs in PSCs.<sup>173, 174</sup> Moreover, their easy processability, good thermal stability, and impressive ability to transport charge made these materials ideal for their inclusion in low-cost solar devices.

For all these reasons, fullerenes are reputed to be exceptional electron transporters and great hole blockers. Anyway, this well-known fact should not limit the creativity of the scientist investigating the properties of fullerenes. In fact, a proper tuning of the electronic features of the fullerene material could be obtained through an adjusted chemical design. Considering the extensive research on fullerenes and their broad list of applications as ETMs, the possibility of extending this performance also to HTMs based on them is undoubtedly appealing.

In this regard, in literature it is possible to find a few studies on OPV devices prepared with fullerene derivatives as HTMs.<sup>175</sup> Wang and co-workers, for example, performed studies on all-fullerene OPV

devices, where the C<sub>70</sub> acceptor is blended with either **PC<sub>61</sub>BM** or **ICBA** as supposed electron donors.<sup>176</sup> The group wanted to take advantage of the difference between the electron accepting ability of pristine C<sub>70</sub> and the aforementioned C<sub>60</sub> derivatives. However, the obtained PCEs were extremely low, mainly due to the scarce hole transfer ability of the C<sub>60</sub> derivatives.

Hence, there are still no successful works in which a fullerene derivative is used as donor in OPV so far. Nonetheless, a proper chemical functionalization of the fullerene sphere could address this issue.

The addition of six organic addends to the fullerene cage yields the so-called fullerene hexakis adducts.<sup>177, 178</sup> The LUMO energy levels of these compounds differ to those of the corresponding monoadducts by up to one volt.<sup>144, 179</sup>

As for now, several fullerene hexakis adducts have been synthesized for practical applications.<sup>180, 181</sup> Hexakis fullerenes have often been investigated for their activity as potential drug carriers. For example Nierengarten, Martín, Rojo, Vidal, and co-workers prepared fullerene hexakis adducts containing twelve carbohydrate moieties.<sup>182</sup> The authors investigated how these sugar moieties interact with proteins, being this kind of interaction at the basis of most biological processes.<sup>183, 184</sup> These glyco-hexakis adducts showed an interesting antiviral activity in an Ebola pseudotyped infection model.<sup>185, 186</sup> Similarly, hexakis adducts of fullerene have been studied as gene-transfection vectors.<sup>187</sup>

Furthermore, energy transfer between the cage and the substituents has been investigated, finding a clear light-harvesting activity when C<sub>60</sub> is properly substituted (C<sub>60</sub>(A)<sub>12</sub>, Figure 3.3.1).<sup>188</sup>

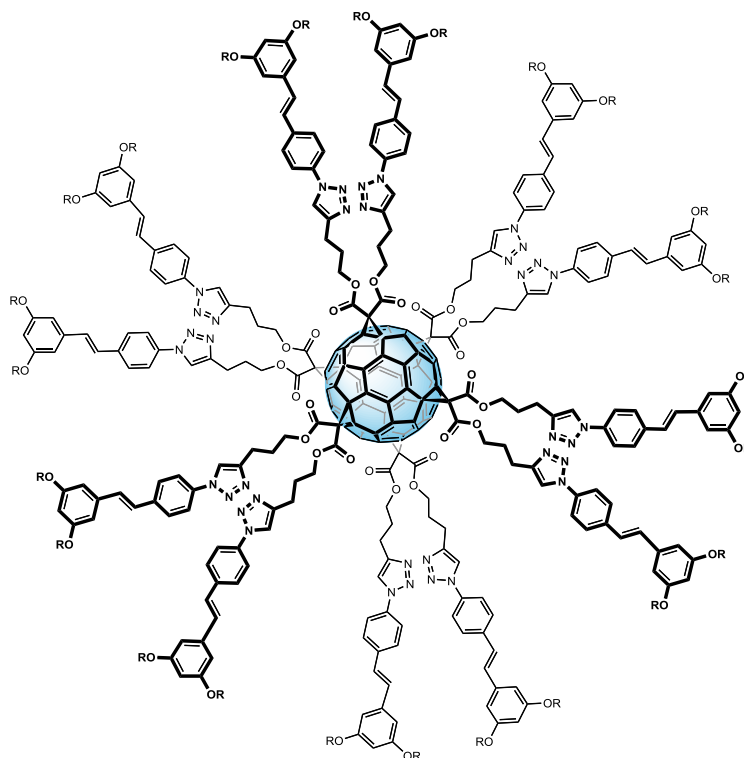


**Figure 3.3.1:** Structure of C<sub>60</sub>(A)<sub>12</sub>. R stands for -C<sub>12</sub>H<sub>25</sub>

In light of all this information, a novel C<sub>60</sub> fullerene hexakis adduct (FU7, Figure 3.3.2) was prepared through the functionalization of the fullerene cage with twelve Oligotriarylamine fragments, in order to make this new material able to transport holes.

### 3.3.2 Synthesis and Characterization of the novel C<sub>60</sub> hexakis adduct

FU7 was obtained through a 12-fold Cu-catalyzed alkyne-azide “click” reaction (Scheme 3.3.1).

The synthesis of the final product comes after the preparation of two reagents, namely the triarylamine substituent and the fullerene cage (Schemes 3.3.2 and 3.3.3).

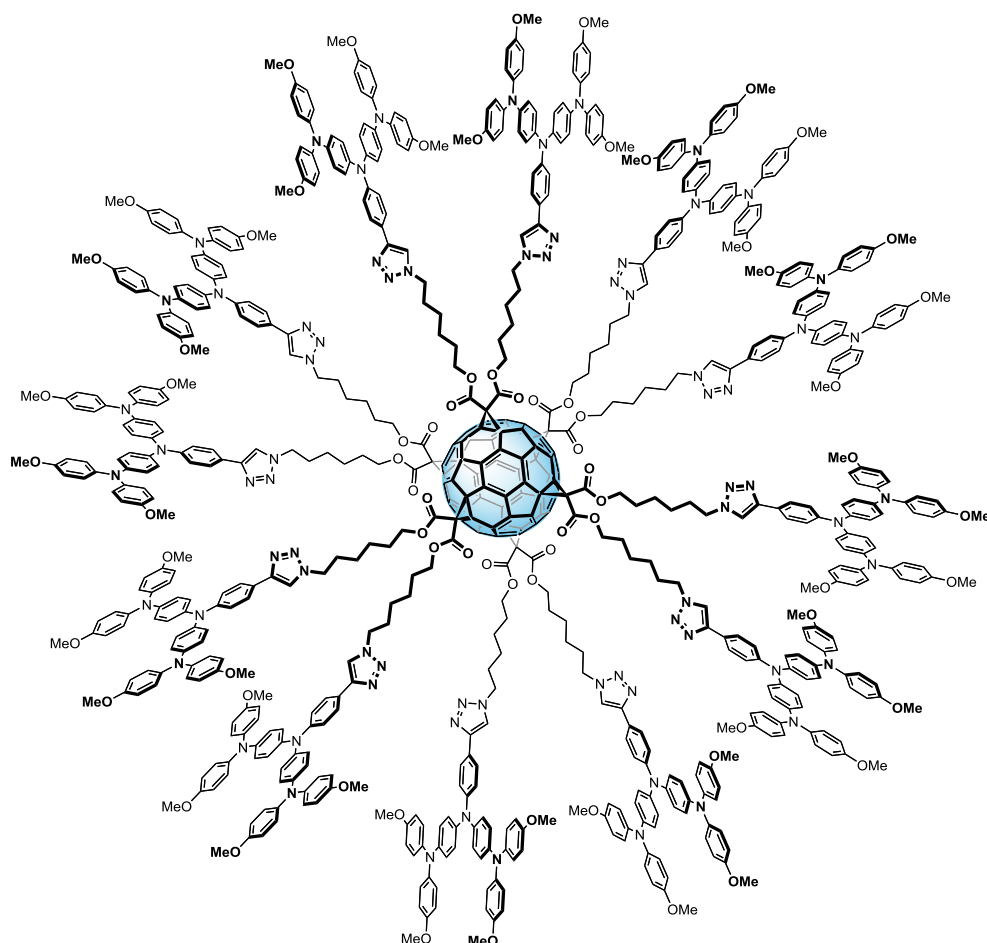
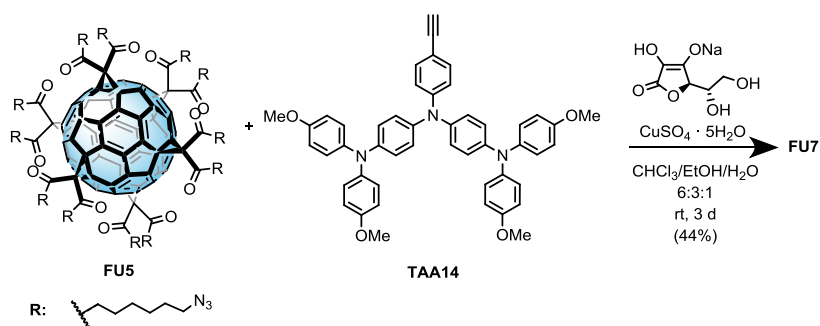
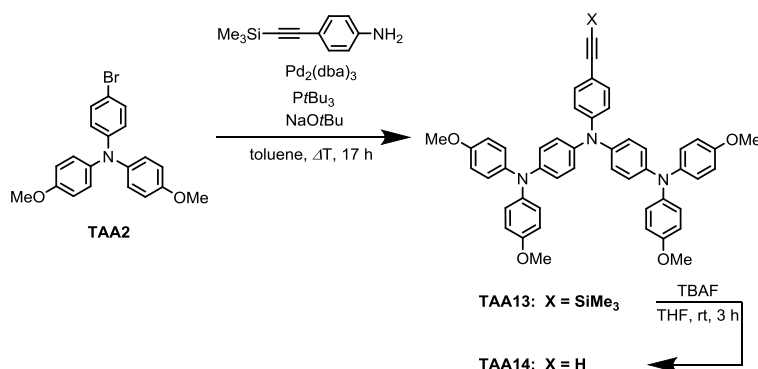


Figure 3.3.2: Structure of the  $C_{60}$  hexakis adduct FU7



Scheme 3.3.1: Synthesis of FU7 starting from precursors FU5 and TAA14

- The triarylamine substituent (Scheme 3.3.2) was synthesized through a *Buchwald-Hartwig* coupling of 4-bromo-*N,N*-bis(4-methoxyphenyl)aniline and 4-((trimethylsilyl)ethynyl)aniline, followed by deprotection of the terminal alkyne.

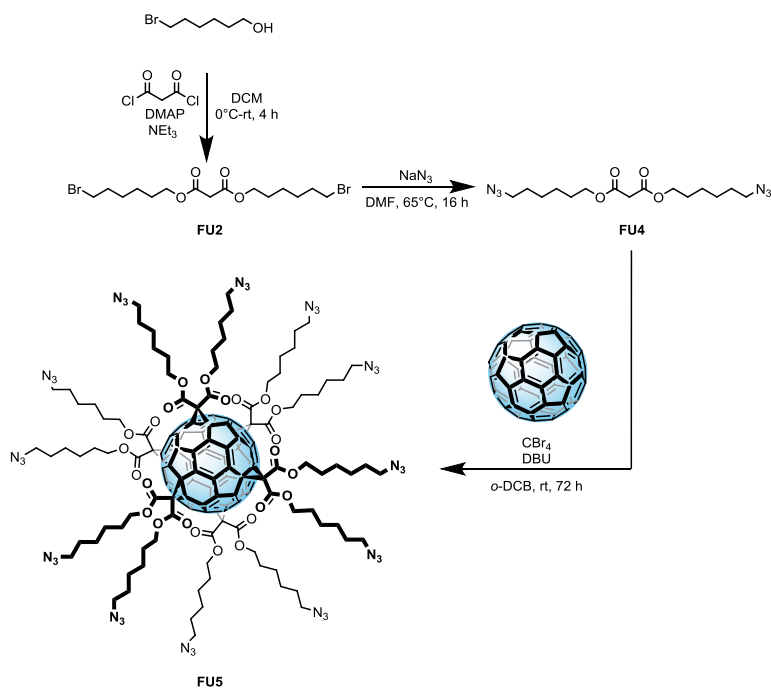


**Scheme 3.3.2:** Synthesis of FU7's precursor TAA14.

- The fullerene core (Scheme 3.3.3) was synthesized through multiple cyclopropanation of the fullerene cage, starting from bis(6-azidohexyl) malonate (FU4). This was prepared starting from 6-bromohexan-1-ol and malonyl chloride, which reacted to give bis(6-bromohexyl) malonate (FU2).

The success of the reaction was confirmed by several spectroscopic techniques, such as <sup>13</sup>C-NMR, MALDI-TOF, and <sup>1</sup>H-NMR. The latter can be observed in Figure 3.3.3, together with the spectra of the precursors **TAA14** and **FU5** for a proper comparison and demonstration.

The complete characterization of the compound is reported at the end of this chapter (Figures 3.3.21-3.3.28)



Scheme 3.3.3: Synthesis of FU7's precursor FU5.

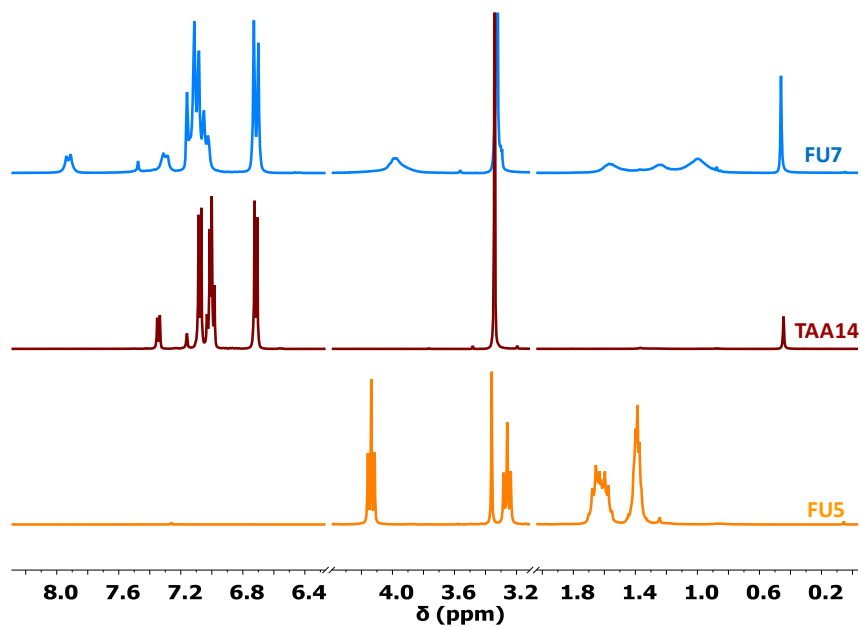
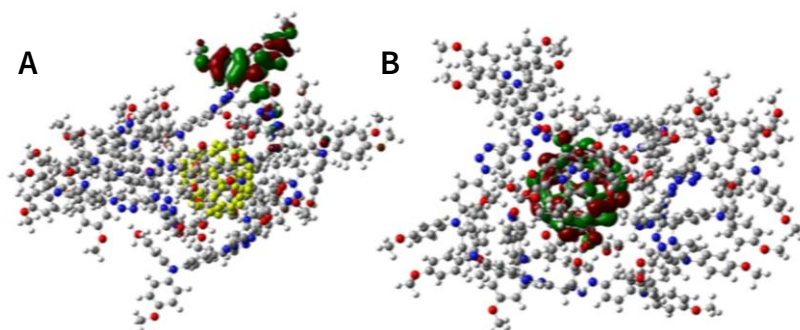


Figure 3.3.3: <sup>1</sup>H-NMR spectra of the derivative FU7 (light blue) and the precursors TAA14 (red) and FU5 (orange). It is appreciable how the precursors' signals are still present in the final product.

Resorting to density functional theory (DFT) calculations allowed the location of the HOMO and the LUMO to be detected. The simulation, carried out with Gaussian 09,<sup>189</sup> indicated that the HOMO is located on the Oligotriarylamine hole-transporting fragments and the LUMO is located on the fullerene cage (Figure 3.3.4). Interestingly, the HOMO orbital comes out as located in one of the Oligotriarylamine moieties instead of being delocalized in all the Oligotriarylaminines.



**Figure 3.3.4:** HOMO (A) and LUMO (B) of FU7 estimated by DFT with the Gaussian 09 suite of programs. Structure optimization was performed in gas phase using the B3LYP functional and the 3-21G basis set. Note that the HOMO orbital is located in one of the Oligotriarylamine moieties instead of being delocalized in all the Oligotriarylaminines. This is a consequence of the lack of symmetry in the molecule, which breaks the expected degeneracy of the HOMO in a set of molecular orbitals, very close in energy, corresponding to each Oligotriarylamine branch. In practice, each of them could be the HOMO, but we have selected this particular one for the sake of clarity in the figure.

The electronic properties of FU7 were investigated through cyclic voltammetry (Figure 3.3.5.A) and ossteryoung square-wave voltammetry in DCM (Figure 3.3.5.B), allowing to estimate a HOMO value of  $-5.04$  eV and a LUMO value of  $-3.50$  eV. This is linked to a significant reduction in electron affinity with respect to the well-known fullerene-based ETMs.<sup>190</sup>

To avoid an overlap of the high oxidation potential of **FU7** and ferrocene, the chosen reference was decamethylferrocene/decamethylferrocenium, which in an additional experiment was calculated to have an oxidation potential of  $-555\text{ mV}$  *vs* ferrocene/ferrocenium ( $\text{Fc}/\text{Fc}^+$ ). HOMO and LUMO energy levels were obtained from the half-wave potentials of the cyclic voltammetry or the peak potentials of the osteryoung square-wave voltammetry measurements, and from the UV-Vis absorption spectra. The HOMO level was calculated according to the following equation, previously explained in section 3.2.2:

$$E(\text{HOMO/LUMO}) = -5.16\text{ eV} - E(\text{oxidation/reduction}).^{165}$$

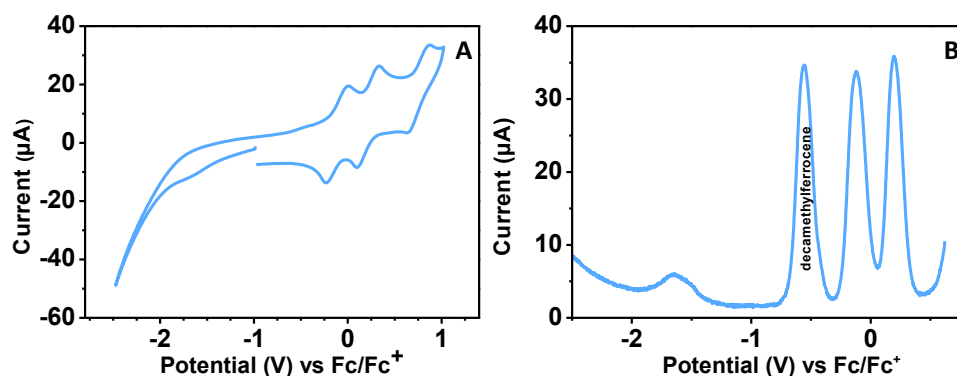


**Figure 3.3.5:** A) Cyclic voltammogram of **FU7** in DCM/TBAHFP (0.1 M) at a scan rate of  $250\text{ mV s}^{-1}$ . B) Osteryoung square-wave voltammogram of **FU7** in DCM/TBAHFP (0.1 M) at a scan rate of  $50\text{ mV s}^{-1}$ .

Furthermore, the study of non-optimized organic field effect transistor (OFET) devices constituted of  $\text{Si}/\text{SiO}_2$  (150 nm)/HMDS/Ti



(5 nm)/Au (35 nm)/FU7 allowed to confirm that FU7 is a p-type semiconductor, which displays lower hole mobility than reference Spiro-OMeTAD (Figure 3.3.6).

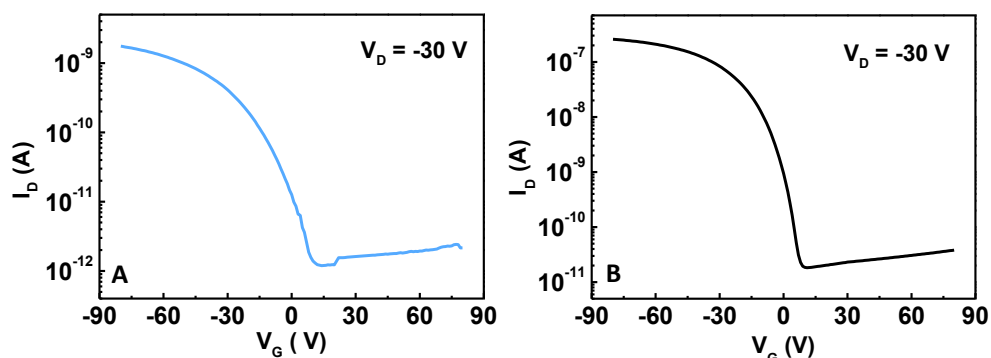


**Figure 3.3.6:** A) Representative transfer curve of a bottom-gate, bottom-contact field-effect transistor with a FU7 channel. B) Representative transfer curve of a bottom-gate, bottom-contact field-effect transistor with a Spiro-OMeTAD channel. In both A) and B), the p-type semiconducting behaviour of the molecular layer can be directly extracted from the behaviour of the drain current *vs* the gate voltage. Both molecules were used without additives for the preparation of the OFETs.

The LUMO level of FU7 (-3,5 eV) is comparable to that of other HTMs which have been described as efficient electron blocking materials.<sup>191-193</sup>

All these properties indicate FU7 might be the first fullerene derivative with the ability to behave as an electron-blocking/hole-transporting material in optoelectronic devices.

### 3.3.3 Incorporation of the materials in PSCs

PSCs containing FU7 as HTM were prepared and compared with standard reference cells with Spiro-OMeTAD.

For the device fabrication, glass coated with FTO as transparent conductive contact was used. As ETM, a compact layer of TiO<sub>2</sub> was

deposited by spray pyrolysis, to get a thickness of  $\sim 50$  nm, with a  $\sim 200$  nm-mesoporous  $\text{TiO}_2$  layer subsequently spin-coated on the top of it. A  $\sim 300$  nm- $\text{MAPbI}_3$  perovskite layer was deposited in air conditions on the top of mesoporous  $\text{TiO}_2$ .<sup>194</sup> A detailed description of each step is reported at the end of this chapter.

The optimal concentration for FU7 was investigated. The results, reported in Table 3.3.1, show that the highest efficiencies were obtained within a concentration range of 8-9 mg  $\text{ml}^{-1}$ . Such concentrations yielded FU7 layers of  $\sim 40$  nm thickness (Figure 3.3.7.B), sensibly smaller than the standard  $\sim 200$  nm Spiro-OMeTAD (Figure 3.3.7.A).

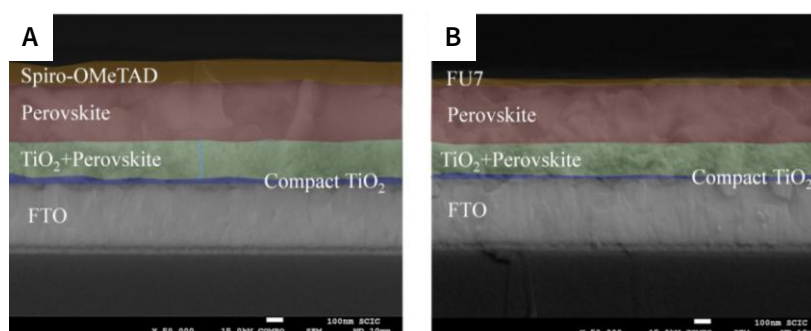


**Figure 3.3.7:** Cross section of PSCs containing either A) Spiro-OMeTAD or B) FU7 as HTM, with compact  $\text{TiO}_2$  as ETM and meso- $\text{TiO}_2$  scaffold. Scale bar indicates 100 nm.

Higher concentrations generated thicker films, with the result of increasing the hole transport resistance at the HTM, as it was detected through impedance spectroscopy (Figure 3.3.8).<sup>195</sup> On the other hand, an excessive reduction of the concentration led to layers with too low thickness and containing pinholes.

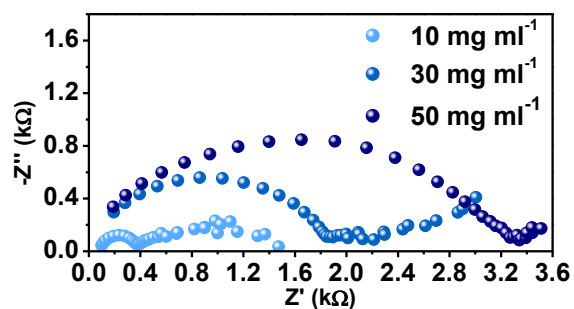


**Figure 3.3.8.** Nyquist plot of PSCs using FU7 as HTM under 1 sun illumination at 0.4 V DC forward applied bias. Different concentrations were used for the deposition of the FU7 film (10, 30, and 50 mg ml<sup>-1</sup>). A clear increase of the size of the high frequency arc with the concentration can be appreciated. This is affected by the charge transport at the ETLs, increasing with the transport resistance, whose increment at the contacts affects negatively the cell performances.<sup>195, 196</sup>

FU7	Scan	$J_{sc}$ (mA cm <sup>-2</sup> )	$V_{oc}$ (V)	FF(%)	PCE (%)
5 mg ml <sup>-1</sup>	backward	17.8	0.954	63	10.7
	forward	19.3	0.958	51	9.3
7 mg ml <sup>-1</sup>	backward	19.5	0.985	65	12.4
	forward	20.2	0.988	60	11.9
8 mg ml <sup>-1</sup>	backward	20.4	0.976	68	13.6
	forward	21.4	0.970	54	11.3
9 mg ml <sup>-1</sup>	backward	20.8	0.985	67	13.7
	forward	22.1	0.980	53	11.4
10 mg ml <sup>-1</sup>	backward	21.1	0.943	64	12.7
	forward	21.5	0.953	56	11.4
30 mg ml <sup>-1</sup>	backward	16.0	0.881	29	4.1
50 mg ml <sup>-1</sup>	backward	9.3	0.822	22	1.7

**Table 3.3.1:** PV performances of the best PSCs prepared with different concentrations of FU7 in CB as HTM. Both forward and backward scans are considered.

The maximum efficiency obtained for a FU7-containing PSC was 13.7% using a concentration of  $9 \text{ mg ml}^{-1}$  of FU7. With this concentration, the perovskite layer is coated as a uniform and smooth layer covering the perovskite film (Figure 3.3.9).

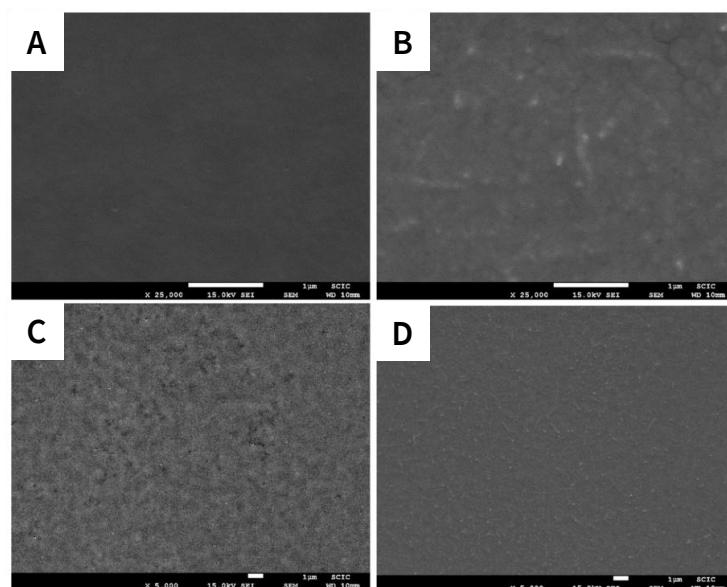


**Figure 3.3.9:** Top view of HTM film deposited on top of perovskite. A and C) Spiro-OMeTAD, and B and D) FU7. In each case, the scale bar indicates  $1 \mu\text{m}$ . This implies that A and B are a magnification of, respectively, C and D.

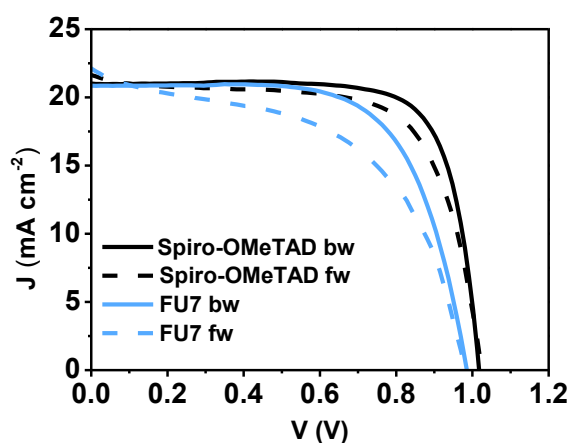


**Figure 3.3.10:** Current-potential ( $J$ - $V$ ) curves of the best cells containing either FU7 or Spiro-OMeTAD as HTM. Curves at forward (fw) and backward (bw) scans are plotted.

Table 3.3.2 summarizes the PV parameters obtained with each different device. Both best cells' parameters and the average are reported.  $J$ - $V$  curves for champion cells prepared with FU7 and

Spiro-OMeTAD are depicted in Figure 3.3.10.

The stabilized PCE of the best FU7-containing device was very close to the one obtained through *J-V* backward measurements (Figure 3.3.11).

It is important to remark

once again that Spiro-OMeTAD needs additives to work properly as HTM. However, no additive was employed for the preparation of FU7-containing cells, whose performances were instead undermined by the introduction of additives (Table 3.3.2).

As already pointed out in the introduction of this thesis, the use of additives to increase the conductivity of HTM has some relevant drawbacks, with the reduction of long-term stability being the most important one.<sup>58, 59</sup> Despite the intensive research focused on additive-free HTMs, no system has overcome the performance obtained with doped Spiro-OMeTAD-containing cells yet. As for today, the highest efficiency reported for an additive-free HTM (18.9%) has been obtained with a molecularly engineered star-shaped D- $\pi$ -A molecule incorporating a rigid quinolizino acridine.<sup>197</sup>

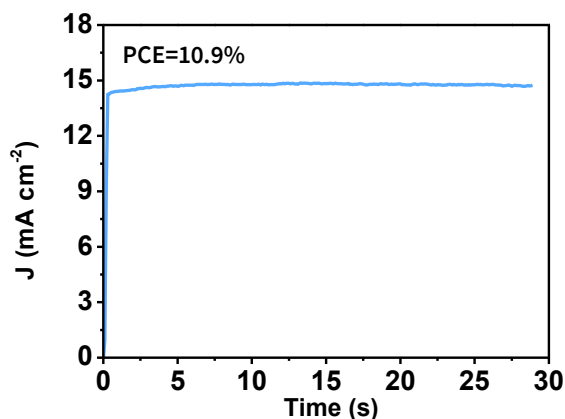
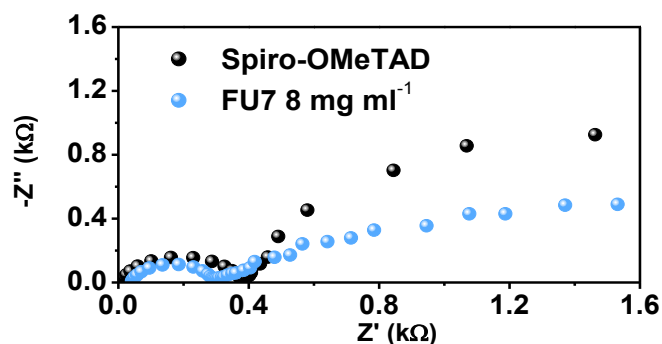


Figure 3.3.11: A stabilized PCE of 10.9% was obtained measuring the stabilized current of the best FU7-containing device at  $V_{MP}$ . The reported PCE is very similar to the PCE obtained through *J-V* measurement of the best cell with the same conditions (5 mg ml<sup>-1</sup> of FU7, 10.7%).

Sample	Scan	$J_{sc}$ (mA cm <sup>-2</sup> )	$V_{oc}$ (V)	FF(%)	PCE (%)
Spiro-OMeTAD	backward	20.8±0.5	1.04±0.010	74±5	16.0±1.2
	forward	20.7±0.5	1.04±0.011	71±5	15.3±1.0
	backward	21.7	1.04	75	16.9
	forward	21.6	1.05	68	15.4
FU7	backward	20.6±0.7	0.948±0.026	64±3	12.5±0.8
	forward	21.5±0.6	0.950±0.026	52±2	10.5±0.6
	backward	20.8	0.985	67	13.7
	forward	22.0	0.980	53	11.4
FU7+additives	backward	13.1±1.4	0.802±0.114	67±12	7.2±2.2
	forward	13.7±1.9	0.850±0.041	60±3	7.1±1.4
	backward	15.1	0.909	71	9.7
	forward	16.8	0.900	57	8.6

**Table 3.3.2:** PV performances of PSCs prepared with Spiro-OMeTAD and FU7 as HTMs. Average results and the best cell's parameters are reported for each condition. Champion cell with FU7 was obtained with 9 mg ml<sup>-1</sup> concentration in CB. Both forward and backward scans are considered.

In order to better understand the behaviour of FU7 with respect to that of Spiro-OMeTAD, impedance spectroscopy analysis was carried out. The Nyquist plot for both HTMs is depicted in Figure 3.3.12. It can be clearly appreciated that the low frequency arc is bigger for the reference sample. The extent of this arc is associated with recombination resistance,<sup>195, 198, 199</sup> since it is inversely proportional to recombination rate. Consequently, impedance spectroscopy points towards a higher recombination rate occurring in FU7-containing cells, with a consequent reduction of photovoltage. This point is



**Figure 3.3.12:** Nyquist plot of Spiro-OMeTAD- and FU7-containing cells under 1 sun illumination at 0.6 V DC forward applied bias.

confirmed by time-resolved photoluminescence (TRPL) measurements (Figure 3.3.13). The pattern obtained with TRPL was fitted using a biexponential decay, as it has been previously reported in the literature.<sup>31, 200, 201</sup> The obtained characteristic times are depicted in Table 3.3.3. A faster decay of PL was observed when FU7

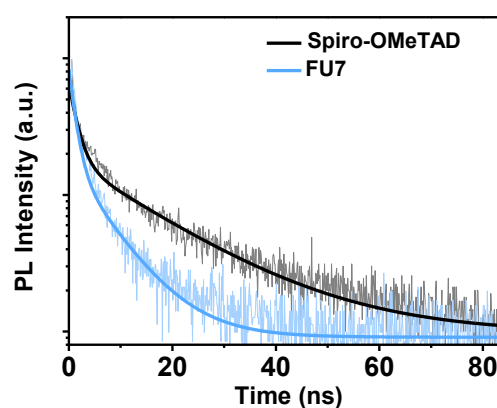


**Figure 3.3.13:** TRPL response acquired using time-correlated single-photon counting (TCSPC) technique, 456 nm was used as excitation wavelength and signal was detected at 770 nm, maximum of the detected PL for the perovskite layer. The decays were fitted with double exponential functions, which are plotted as solid lines.

was deposited on top of the perovskite layer. Two characteristic times,  $\tau_1$  and  $\tau_2$ , were obtained from the fitting. The fastest one,  $\tau_1$ , is associated with the charge carrier injection into the HTM, while the

slowest one,  $\tau_2$ , is related to recombination. Deposition of **FU7** layer on the top of perovskite reduces  $\tau_1$  significantly, indicating an

Sample	$\tau_1$ (ns)	$\tau_2$ (ns)
Perovskite	2.8	20.7
Perovskite+FU7	1.2	7.4

**Table 3.3.3:** TRPL lifetimes obtained fitting the data in Figure 3.3.13 to a biexponential decay. Perovskite layer was deposited on glass and **FU7** was deposited on the top of the perovskite layer.

efficient hole transfer.

However, recombination is also faster as it can be deduced by the decrease of  $\tau_2$ . This analysis indicates interfacial recombination of fullerene-based HTMs has to be reduced

in the future in order to improve the performances here reported.<sup>202</sup>

Another important aspect that needs further analysis is the real role of fullerenes in the hole-transporting properties of **FU7**. Figure 3.3.4 clearly shows that holes at HOMO are localized in the Oligotriarylamine (TAA) moieties covalently connected to the fullerene. The TAA fragment presents by itself a hole-scavenging effect in accordance to the low  $\tau_1$  measured through TRPL (Table 3.3.4). **TAA14** is the non-fullerene precursor of **FU7** (Scheme 3.3.2). Devices with pinhole-free **TAA14** films (Figure 3.3.14) as HTM were

Sample	$\tau_1$ (ns)	$\tau_2$ (ns)
Perovskite+TAA14	0.5	5.0

**Table 3.3.4:** TRPL lifetimes obtained when **TAA14** was deposited on the top of the perovskite layer

prepared. However, the performances obtained with **TAA14** are significantly lower than those observed with **FU7** as HTM (Table 3.3.5).

Two different aspects could contribute to the higher performance of **FU7** in comparison to **TAA14**. First, a higher recombination rate is



measured for **TAA14** HTM by means of TRPL (Tables 3.3.3 and 3.3.4).

Sample	Scan	$J_{sc}$ (mA cm <sup>-2</sup> )	$V_{oc}$ (V)	FF(%)	PCE (%)
TAA14	backward	14.25±1.3	0.866±0.105	48±6	6.0±1.4
	forward	14.3±1.2	0.866±0.092	39±4	4.8±1.0
	backward	15.8	0.925	52	7.6
	forward	15.6	0.917	42	6.1

**Table 3.3.5:** PV performances of PSCs prepared with **TAA14** as HTMs. Average results and the best cell's parameters are reported.

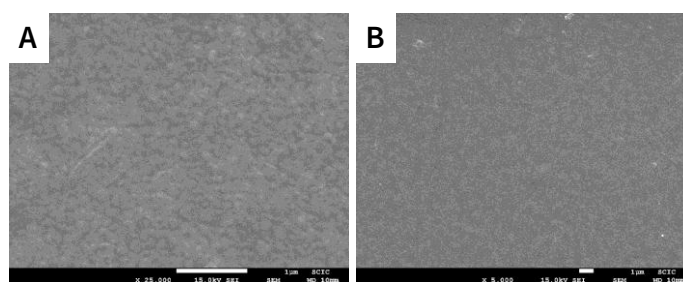


**Figure 3.3.14:** Top view of **TAA14** film deposited on top of perovskite layer. In each case, the scale bar indicates 1 μm. This implies that A is magnification of B.

Moreover, the presence of the fullerene core confers **FU7** a spherical shape (Figure 3.3.2), allowing a favourable connection of HOMO within surrounding molecules and a good separation of LUMO, centred on fullerene (Figure 3.3.4). In addition, the spherical shape permits the preparation of more ordered layers. In the case of **PC<sub>61</sub>BM** layers it has been observed that higher structural order leads to lower energy disorder and higher splitting of the Fermi level, hence to improved photovoltages.<sup>88, 114, 143, 173</sup>

This fact indicates that the fullerene core plays a key role in fullerene-based HTMs, leading to improved charge separation, simplified transport pathway, and increased structural order.

### 3.2.4 Stability measurements

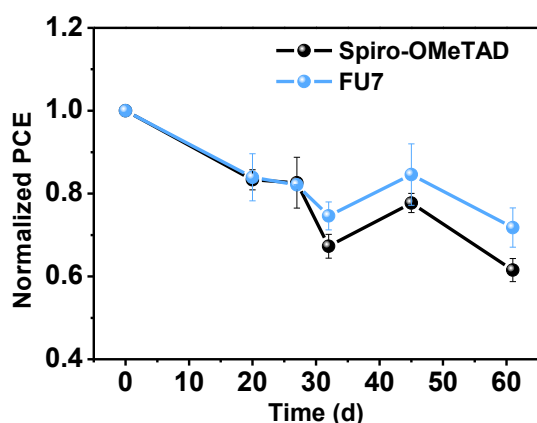


Figure 3.3.15: Normalized PCE obtained from the average of three cells for each condition (using Spiro-OMeTAD and FU7 as HTM). Cells without any encapsulation were stored in the dark, under dry air atmosphere.

PSCs.<sup>75</sup> Three cells of each type, with Spiro-OMeTAD and FU7 as HTMs, were measured over two months; the obtained PCE are plotted in Figure 3.3.15.

During the first month, the efficiency of the samples decreased to 0.85 times the initial value for both Spiro-OMeTAD and FU7-containing samples. However, during the second month, the PCE of Spiro-OMeTAD-containing devices fell down to 0.61 times the original value, whereas the efficiency of FU7 samples decreased just until 0.72 times the initial PCE. This loss in performance is due to a different evolution of the cell parameters (Figure 3.3.16).

The potential effect on the stability of the device conferred by the additive-free nature of the layers was investigated. In chapter 3.2 it was already pointed out how fullerenes contribute to increase long-term stability of

The  $V_{oc}$  of reference cells remained quite constant during the first month of the experiment, whereas in the case of FU7-containing samples it increased to 1.05 times the initial value, to remain constant afterwards (Figure 3.3.16.B). Regarding  $FF$ , the loss was higher for reference samples than for FU7-containing cells (Figure 3.3.16.C). Finally,  $J_{sc}$  of FU7-containing samples fell down to 0.81 times the starting value in the first ten days, to stabilize afterwards (Figure 3.3.16 A). On the contrary, the decrease in  $J_{sc}$  registered for reference cells is more progressive, but attains the same value of FU7-containing cells after two months.

This analysis indicates that, similarly to

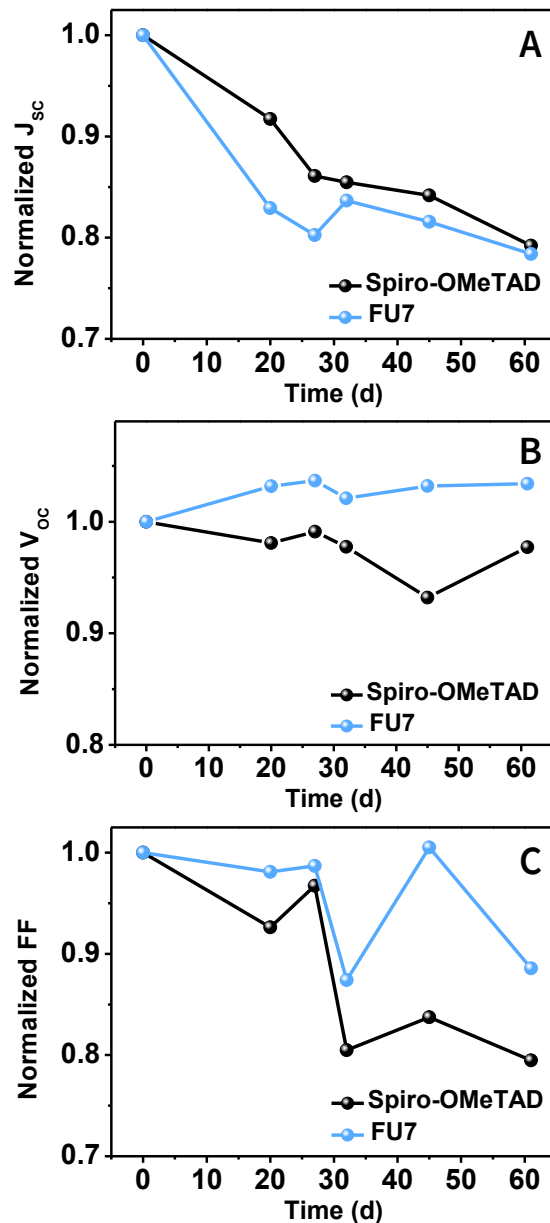


**Figure 3.3.16:** Normalized cell parameters of the aged cells containing either Spiro-OMeTAD or FU7 as HTMs. A)  $J_{sc}$ , B)  $V_{oc}$ , C)  $FF$ .

fullerene-based ETMs, fullerene-based HTMs have positive effects on PSC stability

### 3.2.5 Fullerene Sandwich PSCs

The good performances shown by FU7 as HTM paved the way to the preparation of innovative all-fullerene PSCs. Devices in which both selective contacts are fullerene-based layers were developed.

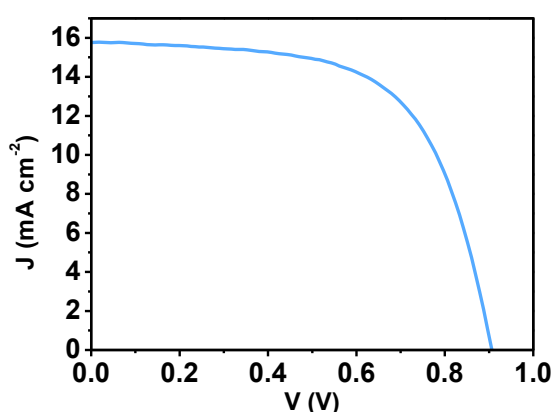


Figure 3.3.17:  $J$ - $V$  curve for best cell device with fullerene sandwich architecture.

In these fullerene sandwich PSCs,  $C_{60}$  and FU7 were used as ETM and HTM, respectively. In addition,  $C_{60}$  was used as additive for the perovskite layer to avoid  $C_{60}$  film degradation during

device fabrication (fullerene saturation approach, as explained in section 3.1.5).<sup>122</sup> The non-optimized fullerene sandwich device presents good efficiencies, close to 9% (Figure 3.3.17).

In order to avoid unwanted batch-to-batch variations, reference devices with Spiro-OMeTAD as HTM were prepared in the same series. The maximum  $J_{sc}$  ( $15.8 \text{ mA cm}^{-2}$ ) of fullerene sandwich PSCs was comparable to that of reference devices. However,  $FF$  (63.3%) and  $V_{oc}$  (0.92 V), were lower than those obtained from the reference (Table 3.3.6).

HTM	$J_{sc}$ (mA cm <sup>-2</sup> )	$V_{oc}$ (V)	FF(%)	PCE (%)
Spiro-OMeTAD	15.7	1.030	75	12.1
FU7 (sandwich)	15.7	0.919	63.3	8.9

**Table 3.3.6:** Device parameters of best reference Spiro-OMeTAD-containing device and fullerene sandwich PSC obtained within the same device series.

FE-SEM cross-section (Figure 3.3.18) shows that no levelling effect occurs for FU7 film. This differs from the efficient levelling showed by the Spiro-OMeTAD layer.<sup>122</sup>

Considering that the glass/FTO/C<sub>60</sub>/perovskite samples prepared in this study presented notable

roughness, the HTL-levelling effect may be crucial for the solar cell performance, hence leaving wide room for improvement in the  $J_{sc}$  of yet non-optimized sandwich devices. However, the reached PCE can be considered as a first proof-of-concept of fullerene sandwich PSC. Indeed there is plenty of room for further optimization, for example resorting on more suitable deposition processes for novel synthesized fullerene-based HTMs, with enhanced properties with respect to the novel FU7. In this regard, the rich chemical versatility of C<sub>60</sub> will allow the preparation of hexakis adducts bearing a great

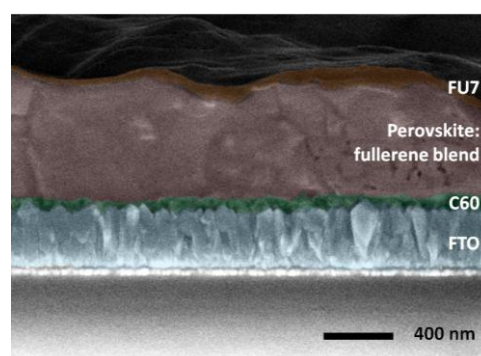


**Figure 3.3.18:** Cross-section FE-SEM micrograph of a fullerene sandwich PSC with architecture FTO/C<sub>60</sub>/MAPbI<sub>3</sub>:C<sub>60</sub>/FU7/Au. The thickness of the fullerene layers is strongly related to the roughness of the underlying layer, resulting in thickness ranges of 10-40 nm for C<sub>60</sub> and 10-50 nm for FU7.

variety of hole transporting moieties, such as phthalocyanines, porphyrins, or exTTF, which could improve and surpass the photovoltaic performance reported here for **FU7**.<sup>203, 204</sup> In addition, a proper evaluation of oxidizing additives for **FU7** could help to improve conductivity with a positive effect in the performance.

### 3.3.6 What now? The merging of concepts

In chapter 3.2, we discussed how hydrophilic PEG chains could help the stability of perovskite solar cells. Now, we demonstrated the viability of PSCs containing a fullerene HTM, whose globular nature given by the fullerene core seems to play an important role on the proper formation of the film.

Taken this information into consideration, the next logical step cannot be but the fusion of these two concepts. Following this idea, a novel fullerene HTM bearing several external PEG chains was synthesized and characterized. The structure of this novel compound is depicted in Figure 3.3.19. The complete characterization is reported at the end of this chapter (Figures 3.3.29-3.3.33).

Similarly to what reported for **FU7**, the new fullerene hexakis adduct **FU26** was obtained through a 12-fold Cu-catalyzed alkyne-azide “click” reaction (Scheme 3.3.4). The synthesis of **FU26** comes after the preparation of two reagents, i.e. the triarylamine substituent **TAA40** and the fullerene cage **FU25**.

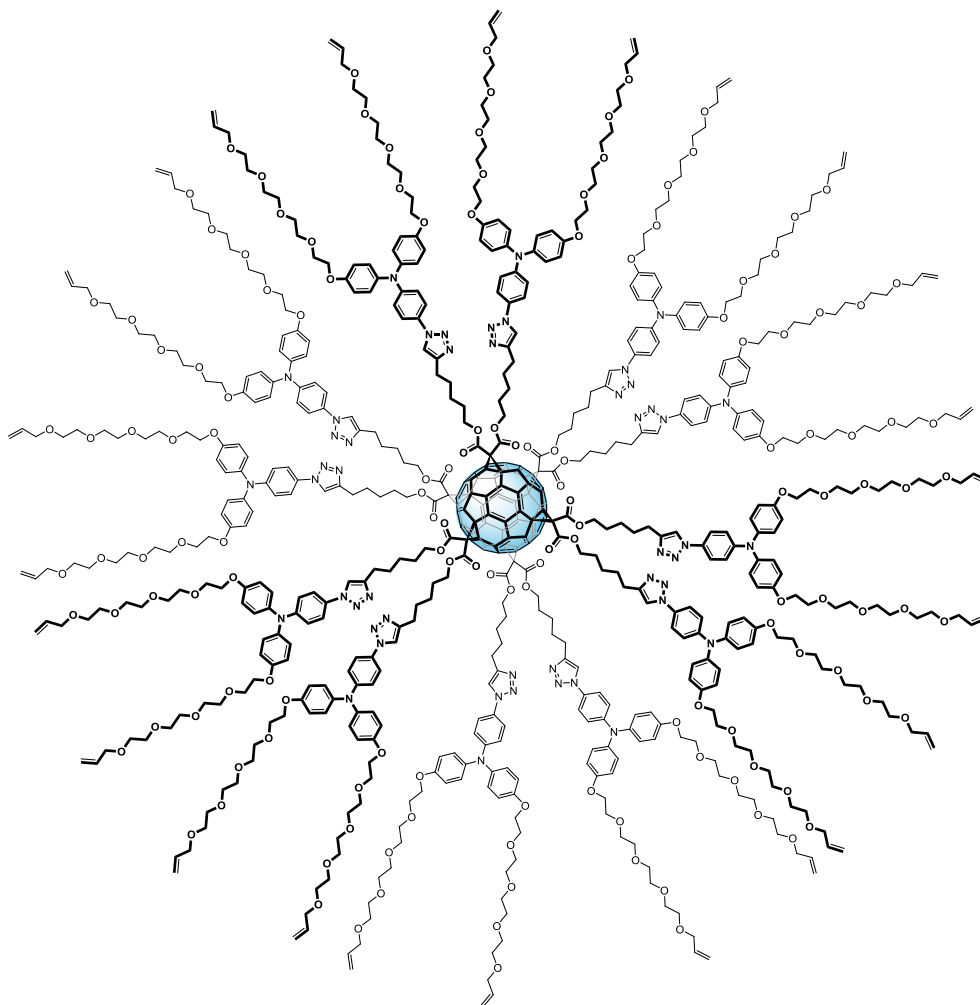
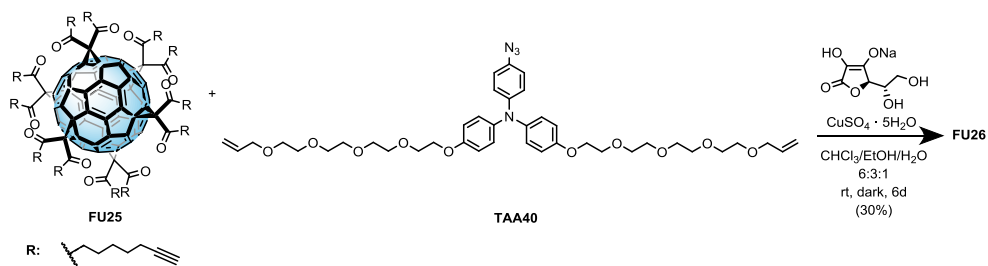
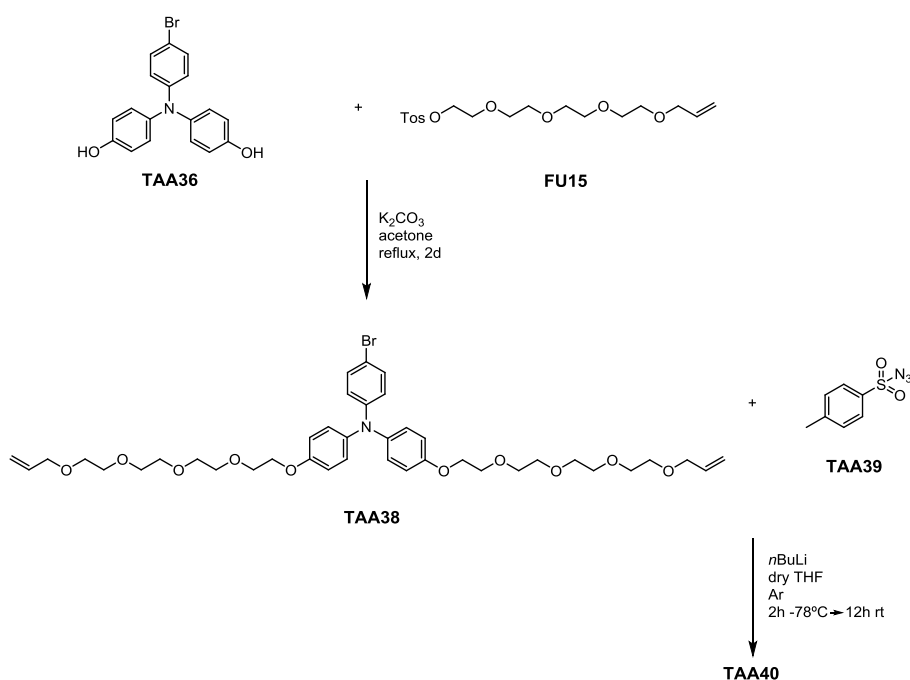


Figure 3.3.19: Structure of the novel derivative FU26



Scheme 3.3.4: Synthesis of FU26 starting from precursors FU25 and TAA40

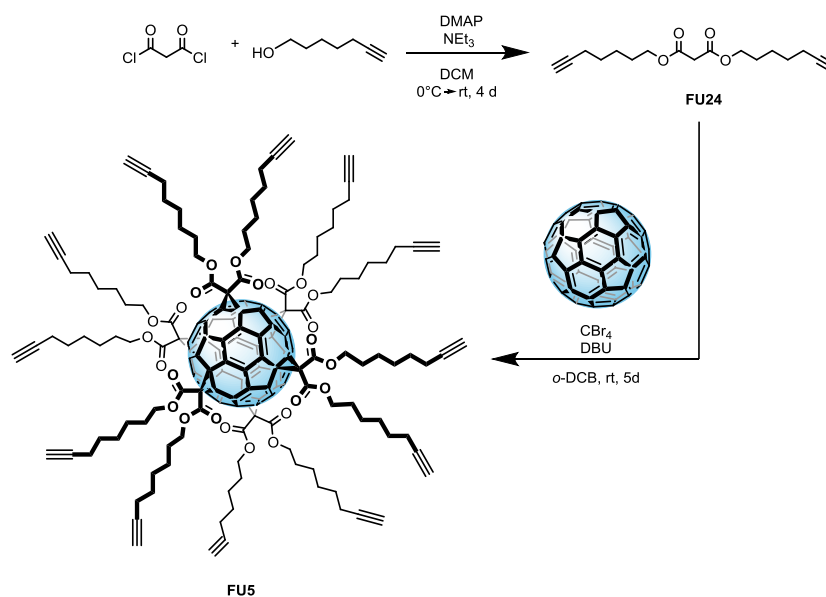
- The triarylamine moiety (Scheme 3.3.5) was synthesized through azidation of the brominated compound TAA38, which was prepared starting from 4-bromo-*N,N*-bis(4-hydroxyphenyl)aniline.



Scheme 3.3.5: Synthesis of FU26's precursor TAA40.

- The fullerene core (Scheme 3.3.6) was synthesized through multiple *Bingel* cyclopropanation of the fullerene cage, starting from bis(hept-6-yn-1-yl) malonate (FU24). This was prepared starting from 6-heptyn-1-ol and malonyl chloride.





**Scheme 3.3.6:** Synthesis of FU26's precursor FU5.

The HOMO level was calculated following the same equation applied for FU7 (Section 3.3.2) and are reported in Table 3.3.6. The voltammogram from which  $E^{1/2_{ox}}$  was extrapolated can be observed in figure 3.3.20. The LUMO level was calculated after the obtention of the bandgap from the UV-Vis absorption spectra.

	$E^{1/2_{ox}}$ (eV)	LUMO (eV)	HOMO (eV)	Bandgap (eV)
C <sub>60</sub>	0.255	-2.18	-5.41	3.23

**Table 3.3.6:** Energy levels and bandgap of FU26.

The calculated HOMO is very similar to that reported for perovskite; nonetheless the much higher LUMO makes this molecule a very

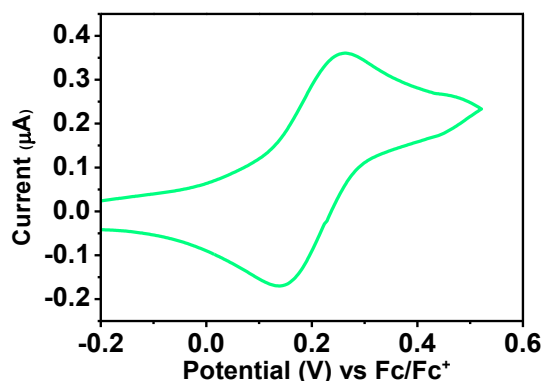


**Figure 3.3.20:** Cyclic voltammogram of FU26 in DCM/TBAHFP (0.1 M) at a scan rate of 100 mV s<sup>-1</sup>

good candidate for electron blocking.

Further experiments are required in order to demonstrate the ability of this molecule to act as an HTM and its effects on stability.

In principle, this novel molecule should be able to guarantee proper charge transport and enhance the device stability against moisture. Furthermore, the terminal alkene moieties have already demonstrated to be prone to undergo cross-linking in light conditions.<sup>205</sup> This would lead to an increase in the strength and to a improvement of the morphology of the HTL.

To sum up, for the first time a HTM based on fullerenes was prepared and tested in PSCs without resorting to any additive. An appropriate chemical design has allowed tailoring the HOMO and LUMO levels of FU7, making it able to block electrons and act as hole-selective contact. Significant efficiencies were obtained, with an average of 0.77 times (0.81 for best devices) the performance of the reference cell prepared with doped Spiro-OMeTAD. The presence of fullerenes plays a key role in the HTM layer structure, allowing the formation of spherical molecules characterized by charge separation,

an easy transport pathway interconnection, and an improvement in the structural order of the film, all these resulting in higher device performances. In addition, FU7-containing devices present higher stability than the reference cells. Moreover, for the first time efficient fullerene sandwich PSCs were prepared. Finally, a new hexakis adduct bearing external PEG chains as a result of the merging of what extrapolated from the studies presented in chapter 3.2 and 3.3 was synthesized and characterized.

These results could have important implications in the development of a new branch in the family of fullerene derivatives, with application as HTM and electron-blocking systems.

### 3.2.6 Materials and Methods

#### Reagents, Solvents, and Other Materials

Chemicals for the synthesis of the novel fullerenes and their precursors were purchased from commercial suppliers and used without further purification. Reactions under N<sub>2</sub> or Ar atmosphere were performed in flame-dried glassware with dry solvents. For flash chromatography, silica gel (40–60 μm) from Acros was used.

For the preparation of solar devices, titanium diisopropoxide bis(acetylacetonate), anhydrous DMF, anhydrous CB, Li-TFSI, and TBP were purchased from Sigma-Aldrich. MAI and PbI<sub>2</sub> were purchased from TCI and TiO<sub>2</sub> 30NR-D paste was purchased from Dyesol. Also in this case, the materials were used as received.

#### Material Characterization

NMR spectra were recorded on either a Bruker Avance 300 (<sup>1</sup>H: 300.2 MHz, <sup>13</sup>C: 75.5 MHz) or 500 (<sup>1</sup>H: 500.1 MHz, <sup>13</sup>C: 125.8 MHz) at room temperature. The chemical shift (δ) is quoted in ppm relative to the internal standard TMS. Proton spin multiplicities are: s = singlet, d = doublet, t = triplet, q = quartet, m = multiplet.

Mass spectra were recorded on either a Bruker-AUTOFLEX SPEED in San Sebastián or on a Bruker-ULTRAFLEX III (MALDI-TOF) in the facilities of the Universidad Autonoma de Madrid.

Infrared spectra were recorded either from the pure sample or from Tol solution on a Bruker ALPHA ATR-IR spectrometer.

UV-Vis spectra were recorded with a PerkinElmer Lambda 950 UV/Vis/NIR spectrometer. Experiments were carried out in 1 cm quartz cuvettes and neat solvent was used as reference.

Fluorescence and excitation spectra were recorded with a PerkinElmer LS 55 fluorescence spectrometer. Experiments were carried out in 1 cm quartz cuvettes.

Electrochemical experiments were performed with a Princeton Applied Research Parstat 2273 in a custom made glass cell using a three electrode setup with a platinum working electrode ( $\varnothing = 0.5$  mm), a platinum wire counter electrode ( $\varnothing = 0.5$  mm), and a Ag/AgNO<sub>3</sub> wire pseudoreference electrode in DCM with TBAHFP as supporting electrolyte ( $c = 0.1$ – $0.2$  M). Cyclic voltammograms and oysteryoung square-wave voltammograms were recorded at a scan rate of  $250 \text{ mV s}^{-1}$  and  $50 \text{ mV s}^{-1}$ , respectively, and referenced *vs* the ferrocene/ferrocenium (Fc/Fc<sup>+</sup>) redox couple.

Field-effect transistors (non optimized) were fabricated in a bottom-gate, bottom-contact configuration. We used a highly n-doped Silicon wafer with a 150 nm-thick SiO<sub>2</sub> thermally grown insulating layer on top which serves as a gate dielectric. Interdigitated electrodes with a width-to-length ratio of 1000 were produced by standard optical lithography and lift-off; the contact material was a bilayer of Ti (5nm) / Au (35 nm) which was grown by electron-beam deposition in ultra-high vacuum. Prior to the deposition of the molecules, the wafers were primed with hexamethyldisilazane (HMDS) to reduce the charge trapping at the molecular/dielectric

interface. The molecular layers were spin-coated from solutions in CB at a maximum speed of 4000 rpm for 30 seconds. The solutions were produced at nominal concentrations of 72,3 mg ml<sup>-1</sup> for Spiro-OMeTAD and 9 mg ml<sup>-1</sup> for FU7. The samples were then transferred to a high-vacuum probe station and the electrical characteristics were measured at room temperature using a programmable semiconductor analyser provided with preamplifiers.

#### Device preparation

- **PSCs containing TiO<sub>2</sub> as ETL:** FTO/glass substrates (Pilkington TEC15, ~ 15 Ω sq<sup>-1</sup>) were etched with zinc powder and HCl 2M. After cautious rinsing, they were cleaned with Hellmanex, rinsed with abundant Milli-Q water, sonicated for 10 min in EtOH, rinsed with acetone, and finally dried with compressed air. Right before the deposition of the compact layer, they were treated with UV/ozone for 15 min. TiO<sub>2</sub> compact layer was deposited onto the substrates through spray pyrolysis at 450 °C, using titanium diisopropoxide bis(acetylacetonate) diluted in ethanol (1:9, v/v). Mesoporous TiO<sub>2</sub> layer was deposited from a solution of TiO<sub>2</sub> paste diluted in ethanol (1:5, weight ratio) spun at 2000 rpm for 10 s. After drying at 100°C for 10 min, they were heated at 500°C for 30 min and cooled down to room temperature. The perovskite solution was prepared by dissolving PbI<sub>2</sub> (1.35 M) and MAI (1.35M) in 1 mL DMF and 80-95 μL DMSO depending on the humidity.<sup>194</sup> The perovskite layer was deposited by spin-

coating at 4000 rpm for 50 s resorting to Et<sub>2</sub>O as antisolvent, dropped approximately 9 s before the end of the program. After the deposition, the substrates were heated at 100°C during 3 min on a hot plate. The HTMs were deposited by spin coating at 4000 rpm for 30 s, Spiro-OMeTAD solution was added while spinning (dynamic deposition, after ~3-5 s from the start of the program). The Spiro-OMeTAD solution was prepared dissolving 72.3 mg of the molecule in 1 mL of CB, adding 28.8 μL of TBP and 17.5 μL of a Li-TFSI stock solution (520 mg mL<sup>-1</sup> in ACN). **FU7** and **TAA14** were dissolved in CB; several concentrations of **FU7** were tried. The solutions were sonicated for 30 min before being spun onto the perovskite layers at 4000 rpm for 30 s. Finally, an array of round Au back contacts (~0.07 cm<sup>2</sup>) was deposited by thermal evaporation at around 5 × 10<sup>-6</sup> torr with a NANO38 (Kurt J. Lesker) apparatus with a shadow mask. All the samples were prepared in air conditions.<sup>194</sup>

- **PSCs containing C<sub>60</sub> as ETL:** C<sub>60</sub> films were deposited by spin-coating in an Ar-filled glovebox. A two-step protocol with a first step of 1500 rpm for 60 s and a second step of 2700 rpm for 60 s was followed. The perovskite solution was prepared dissolving 7.71 mmol of MAI and 2.57 mmol of PbCl<sub>2</sub> (molar ratio 3:1) in 3 mL of DMF. This solution was left stirring overnight. Before the deposition, the perovskite solution was saturated with C<sub>60</sub>. The resulting solution was spun on the

substrates following a two-step protocol, which consisted of a first step of 500 rpm for 5 s followed by a second step of 2000 rpm for 45 s. Subsequently, the samples were annealed at 100°C for 2 h to ensure complete perovskite formation. On top of the perovskite layer, the Spiro-OMeTAD HTM was deposited from a solution that contained Spiro-OMeTAD (108.4 mg) in CB (953.43 mL), LiTFSI solution in ACN (17.17 mL, 520 mg ml<sup>-1</sup>), and TBP (29.4 mL). FU7 was deposited using the same procedure than for samples on TiO<sub>2</sub> substrate. The HTM was deposited by spinning the solution at 3000 rpm for 30 s. The samples were left in a desiccator overnight. Finally, an array of round Au back contacts (~0.07 cm<sup>2</sup>) was deposited by thermal evaporation at around 5 × 10<sup>-6</sup> torr with a NANO38 (Kurt J. Lesker) apparatus with a shadow mask.

### Device Characterization

The *J-V* curves were measured in Abet Technologies Sun 2000 ClassA solar simulator (AM1.5G, 100 mW cm<sup>-2</sup>) with a Keithley 2612 SourceMeter. The measurements were performed at 50 mV s<sup>-1</sup> with a dwell time of ~0.25 s using a mask with an area of 0.107 cm<sup>2</sup>.

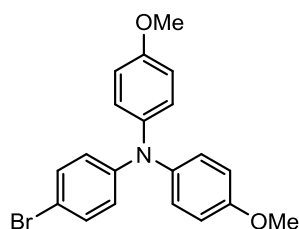
PL measurements were carried out in a HORIBA FL-1000 Fluorimeter. TRPL response was acquired using time-correlated single-photon counting (TCSPC) (IBH-5000-U, HORIBA) using a LED (464 nm) as excitation light source. SEM characterization was performed using a field emission scanning electron microscope



(FE-SEM) JEOL 7001F. Impedance Spectroscopy measurements were performed using a Metrohm Autolab PGSTAT30 potentiostat.

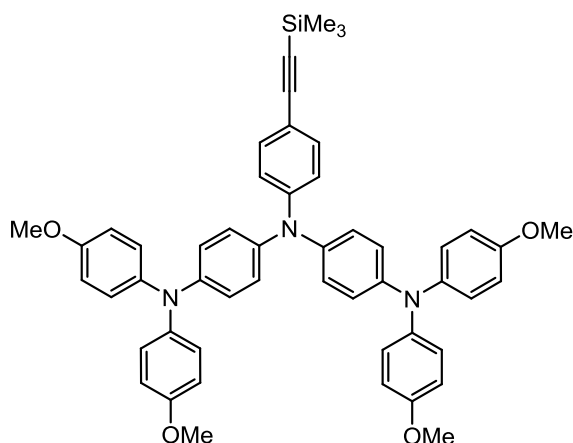
### Synthetic procedures and compound characterization

#### TAA2



Synthesis and characterization can be found in literature.<sup>206</sup>

#### TAA13



**TAA2** (2.03 g, 5.28 mmol), 4-((trimethylsilyl)ethynyl) aniline (500 mg, 2.64 mmol), and NaOtBu (990 mg, 10.3 mmol) were dissolved in dry Tol (14 ml) under Ar

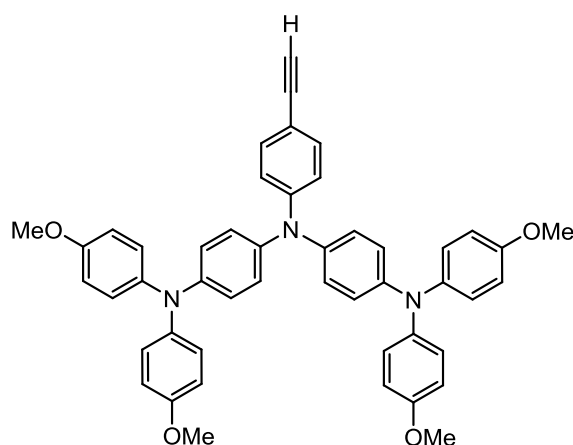
atmosphere and the mixture was degassed in a stream of Ar for 10 min. Pd<sub>2</sub>(dba)<sub>3</sub> (193 mg, 211 μmol) and PtBu<sub>3</sub> (1 M in toluene, 211 μl) were added and the mixture was refluxed for 1 d. The solvent was removed under reduced pressure and the residue was purified by column chromatography (eluent:DCM/Hex 2:1). The product was obtained as a yellow solid (491 mg, 617 μmol, 23%).

**<sup>1</sup>H-NMR** (300.2 MHz, acetone-*d*<sup>6</sup>):  $\delta$ [ppm] = 7.27–7.19 (2 H), 7.10–7.02 (8 H), 7.02–6.94 (4 H), 6.94–6.76 (14 H), 3.77 (s, 12H), 0.20 (s, 9H).

**<sup>13</sup>C-NMR** (75.5 MHz, acetone-*d*<sup>6</sup>):  $\delta$ [ppm] = 157.0, 149.9, 146.4, 141.7, 140.4, 133.5, 127.5, 127.3, 122.3, 119.7, 115.6, 114.5, 106.9, 92.5, 55.7, 0.2.

**MS (m/s):** 795.2 (M<sup>+</sup>)

#### TAA14



**TAA13** (420 mg, 528  $\mu$ mol) was dissolved in THF (15 ml) and TBAF (1 M in THF, 739  $\mu$ l, 739  $\mu$ mol) was added. After stirring the mixture at rt for 75 min the solvent was removed under

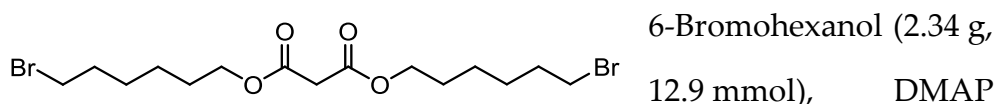
reduced pressure. The residue was dissolved in DCM (30 ml) and H<sub>2</sub>O (30 ml), the phases were separated, the aqueous phase was extracted with DCM (2 x 30 ml), the combined organic phases were washed with H<sub>2</sub>O (30 ml), dried over Na<sub>2</sub>SO<sub>4</sub>, and the solvent was removed under reduced pressure to give the product as a yellow powder (338 mg, 467  $\mu$ mol, 91%).

**<sup>1</sup>H-NMR** (500.1 MHz, C<sub>6</sub>D<sub>6</sub>):  $\delta$  [ppm] = 7.40–7.30 (2H), 7.13–7.04 (8H), 7.04–6.94 (10H), 6.77–6.67 (8H), 3.34 (s, 12H), 2.77 (s, 1H).

**<sup>13</sup>C-NMR** (125.8 MHz, C<sub>6</sub>D<sub>6</sub>):  $\delta$  [ppm] = 156.6, 149.5, 145.8, 141.8, 140.8, 133.5, 126.9, 126.7, 122.7, 120.5, 115.4, 114.4, 84.7, 76.3, 55.2.

**MS (m/z):** 723.3 (M<sup>+</sup>)

## FU2

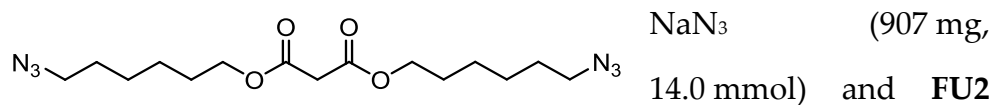


(35 mg, 284  $\mu$ mol), and NEt<sub>3</sub> (2 ml) were dissolved in DCM (70 ml) at 0°C under Ar atmosphere. A solution of malonyl chloride (1.00 g, 7.09 mmol) in DCM (5 ml) was added within 1 min and the mixture was stirred at 0°C for 1 h and warmed up to rt over night. The mixture was washed with HCl (1 M in H<sub>2</sub>O, 2 x 25 ml) and brine (2 x 25 ml) and the organic fraction was dried over Na<sub>2</sub>SO<sub>4</sub>. The solvent was removed under reduced pressure and the residue purified by column chromatography (eluent: Hex/DCM 1:4). The product was obtained as a yellowish oil (2.15 g, 4.99 mmol, 77%).

**<sup>1</sup>H-NMR** (300.2 MHz, CDCl<sub>3</sub>):  $\delta$  [ppm] = 4.15 (t, 4H), 3.41 (t, 4H), 3.37 (s, 2H), 1.93–1.82 (m, 4H), 1.73–1.62 (m, 4H), 1.54–1.33 (8H).

**<sup>13</sup>C-NMR** (75.5 MHz, CDCl<sub>3</sub>):  $\delta$  [ppm] = 166.8, 65.5, 41.8, 33.8, 32.7, 28.4, 27.9, 25.2.

**MS (m/z):** 453.0 (M+Na<sup>+</sup>)

**FU4**

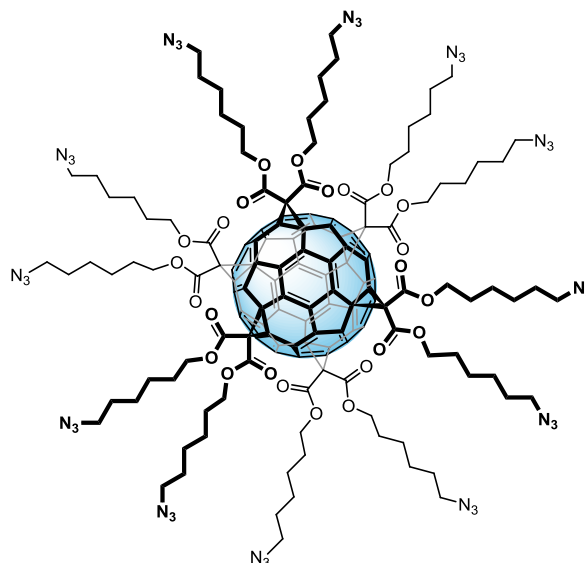
(1.00 g, 2.33 mmol) were dissolved in DMF (8 ml) under Ar atmosphere and stirred at 65°C for 18 h. Upon cooling to rt the mixture was diluted with Et<sub>2</sub>O (20 ml) and washed with H<sub>2</sub>O (40 ml) and brine (40 ml). The aqueous phase was extracted with Et<sub>2</sub>O (20 ml) and the combined organic phases were dried over Na<sub>2</sub>SO<sub>4</sub>. The solvent was removed under reduced pressure and the residue purified by column chromatography (DCM). The product was obtained as a yellow oil (675 mg, 1.91 mmol, 82%).

**<sup>1</sup>H-NMR** (300.2 MHz, CDCl<sub>3</sub>): δ [ppm] = 4.15 (t, 4 H), 3.37 (s, 2 H), 3.27 (t, 4 H), 1.74–1.57 (8 H), 1.47–1.34 (8 H).

**<sup>13</sup>C-NMR** (75.5 MHz, CDCl<sub>3</sub>): δ [ppm] = 166.7, 65.5, 51.8, 41.7, 28.8, 28.5, 26.4, 25.5.

**MS (m/z):** 377.2 (M+Na<sup>+</sup>)

## FU5



C<sub>60</sub> (80 mg, 111  $\mu$ mol), FU4 (392 mg, 1.11 mmol), and CBr<sub>4</sub> (3.67 g, 11.1 mmol) were dissolved in *o*-DCB (33 ml) under Ar atmosphere and the mixture was stirred at rt for 5 min. Subsequently, DBU (337 mg, 2.21 mmol) was added and the mixture was stirred at rt for 3 d. The solvent was removed under reduced pressure and the residue was purified by column chromatography (eluent: PE/DCM 1:9  $\rightarrow$  DCM  $\rightarrow$  DCM/EtOAc 100:1  $\rightarrow$  70:1) to yield a red glassy-like film. The product was stored as toluene solution in the fridge because it decomposes in the solid state if isolated (140 mg, 49  $\mu$ mol, 45%).

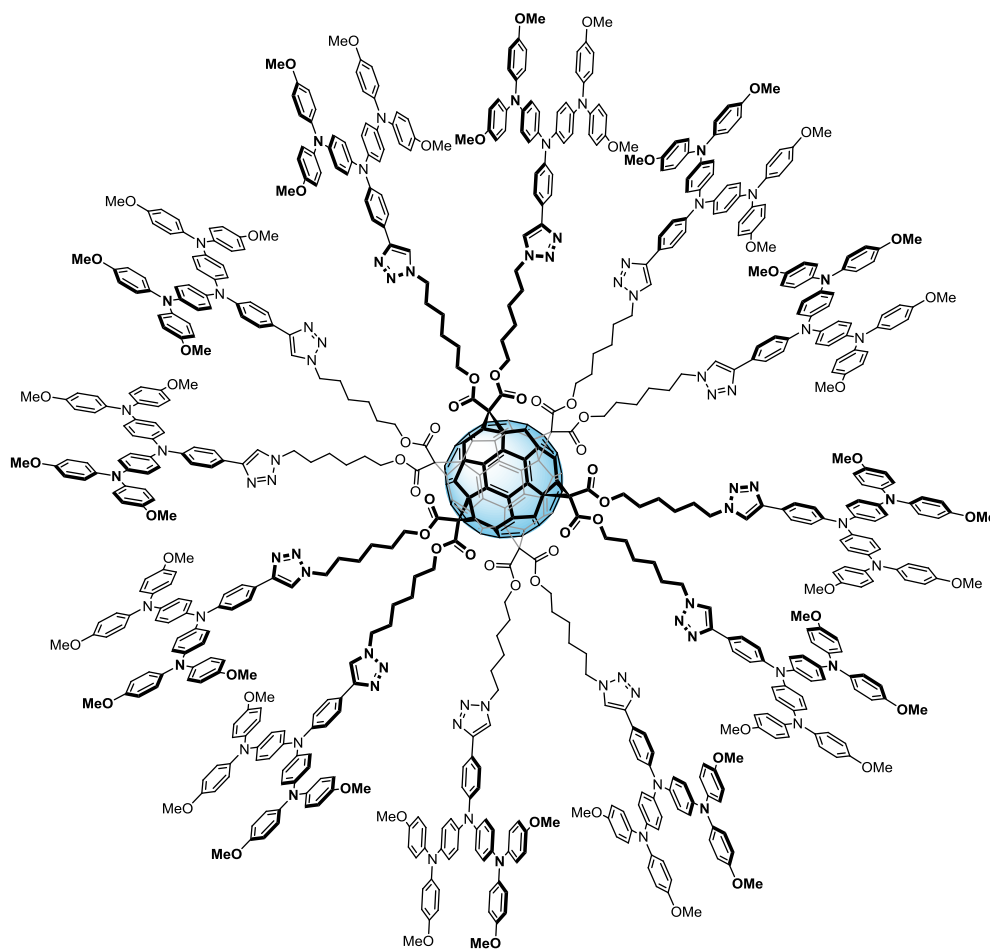
<sup>1</sup>H-NMR (300.2 MHz, CDCl<sub>3</sub>):  $\delta$  [ppm] = 4.25 (t, 24 H), 3.25 (t, 24 H), 1.85–1.15 (96 H).

<sup>13</sup>C-NMR (75.5 MHz, CDCl<sub>3</sub>):  $\delta$  [ppm] = 163.8, 145.8, 141.2, 69.2, 66.8, 51.4, 45.6, 28.8, 28.4, 26.4, 25.5.

**IR** (in toluene):  $\tilde{\nu}$ [cm<sup>-1</sup>] = 3025, 2920, 2868, 2096 (N<sub>3</sub>), 1743, 1603, 1494, 1460, 1380, 1240, 1081, 1030, 727, 693, 463.

**MS (m/z):** 2835.7 (M+H<sup>+</sup>)

### FU7



To a solution of **TAA14** (259 mg, 358  $\mu$ mol) in CHCl<sub>3</sub> (6 ml) was added a solution of **FU5** (70 mg, 25  $\mu$ mol) in CHCl<sub>3</sub> (6 ml) under Ar atmosphere. EtOH (6 ml), H<sub>2</sub>O (2 ml), CuSO<sub>4</sub>·5H<sub>2</sub>O (15.4 mg, 62  $\mu$ mol), and sodium ascorbate (36.7 mg, 185  $\mu$ mol) were added and

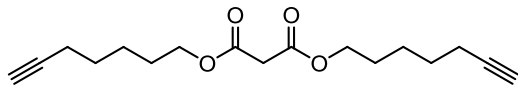
the mixture was stirred under the exclusion of light at rt for 3 d. DCM (10 ml) and H<sub>2</sub>O (10 ml) were added, the phases separated, and the aqueous phase extracted with DCM (2 x 10 ml). The combined organic phases were washed with H<sub>2</sub>O (10 ml) and brine (10 ml), dried over Na<sub>2</sub>SO<sub>4</sub>, and the solvent was removed under reduced pressure. The residue was purified by column chromatography (eluent: DCM/NEt<sub>3</sub> 200:1 → DCM → DCM/MeOH 200:1 → 100:1 → 70:1) to give a brown solid. The solid was suspended in acetone (25 ml), stirred for 5 min at rt, and filtered. Subsequently, the solid was precipitated from DCM to pentane three times to give the product as beige powder (126 mg, 21 μmol, 44%).

**<sup>1</sup>H-NMR** (300.2 MHz, C<sub>6</sub>D<sub>6</sub>): δ [ppm] = 8.04–7.84 (24 H), 7.48 (12 H), 7.36–7.24 (24 H), 7.16–6.95 (192 H), 6.81–6.60 (96 H), 4.33–3.75 (48 H), 3.33 (s, 144 H), 1.76–1.41 (24 H), 1.37–1.15 (24 H), 1.15–0.84 (48 H).

**<sup>13</sup>C-NMR** (125.8 MHz, C<sub>6</sub>D<sub>6</sub>): δ [ppm] = 163.9, 156.3, 148.7, 147.9, 146.5, 145.1, 142.4, 141.8, 141.4, 127.1, 126.5, 126.4, 124.7, 122.9, 122.2, 119.2, 115.2, 70.4, 67.2, 55.1, 50.1, 47.3, 30.4, 28.4, 26.2, 25.6.

**IR** (neat):  $\tilde{\nu}$  [cm<sup>-1</sup>] = 2933, 2833, 1741, 1610, 1493, 1234, 1030, 823, 718, 575, 538.

**MS (m/z)**: 11520.5 (M<sup>+</sup>).

**FU24**

3.00 g of 6-heptyn-1-ol (26.7 mmol), 72.0 mg of DMAP (0.588 mmol) and 4.13 ml of

NEt<sub>3</sub> (25.7 mmol) were dissolved in 75 ml of DCM and cooled down to 0°C. After 15 minutes stirring, 2.79 g of malonyl chloride (19.8 mmol) in 10 ml of DCM were added within 1 minute. The reaction was allowed to warm up to rt and left stirring for 4 days.

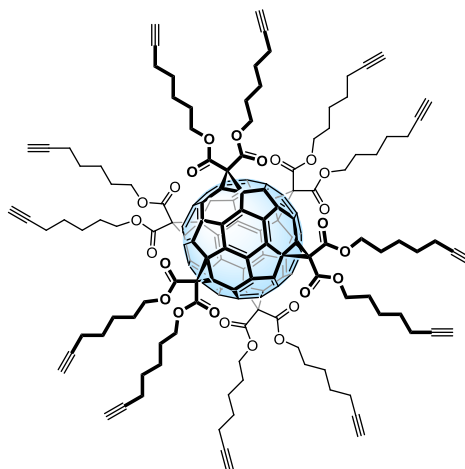
The reaction was quenched with HCl 1M and the phases were separated. The aqueous phase was extracted twice with DCM. The combined organic phases were washed with saturated NaHCO<sub>3</sub> solution twice, then with brine. After drying over Na<sub>2</sub>SO<sub>4</sub>, the solution was concentrated in a rotary evaporator and purified by column chromatography with a gradient of DCM:Hex from 3:1 to 6:1. 3.20 g of a yellowish oil were collected as a final product (10.9 mmol, 82%).

<sup>1</sup>H-NMR (300.2 MHz, CDCl<sub>3</sub>): δ [ppm] = 4.15 (t, 4 H), 3.37 (s, 2 H), 2.21 (td, 4 H), 1.95 (t, 2 H), 1.76–1.60 (m, 4 H), 1.60–1.40 (8 H).

<sup>13</sup>C-NMR (75.5 MHz, CDCl<sub>3</sub>): δ [ppm] = 166.7, 84.3, 68.6, 65.5, 41.7, 28.1, 25.1, 18.4.

**MS (m/z):** 315.15 (M+Na<sup>+</sup>)



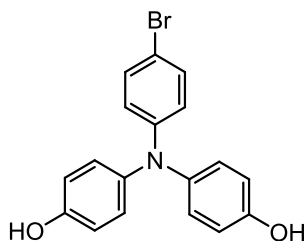
**FU25**

493 mg of C<sub>60</sub> (0.684 mmol) were dissolved in 170 ml *o*-DCB under inert atmosphere. While stirring, 22.7 g of CBr<sub>4</sub> (68.4 mmol), 2.00 g of **FU24** (6.84 mmol) and 2.08 g of DBU (13.7 mmol) were added subsequently. The reaction was left stirring for 5 days. After evaporation of the solvent, the mixture was purified by column chromatography with a gradient of Tol:MeOH from 200:1 to 70:1. A dark red oily solid was retrieved as the final product (1.433 g, 0.582 mmol, 85%).

<sup>1</sup>H NMR (300.2 MHz, CDCl<sub>3</sub>) δ[ppm] = 4.27 (2H), 2.20 (2H), 1.96 (1H), 1.70-1.50 (6H).

<sup>13</sup>C NMR (125.8 MHz, CDCl<sub>3</sub>): δ[ppm] = 163.86, 145.85, 141.21, 84.23, 84.21, 80.06, 69.21, 68.74, 67.06, 66.89, 66.83, 45.53, 38.18, 28.16, 28.10, 28.07, 27.94, 25.19, 25.14, 25.09, 19.71, 18.45, 18.41.

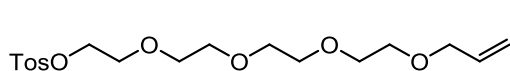
**MS** (m/z): A distribution of peaks with a different extent of ionization with bromine is visible: 2564.9 (M+Na<sup>+</sup>+Br<sup>-</sup>), 2643.9 (M+Na<sup>+</sup>+2Br<sup>-</sup>), 2722.9 (M+Na<sup>+</sup>+3Br<sup>-</sup>), 2801.8 (M+Na<sup>+</sup>+4Br<sup>-</sup>), 2880.7 (M+Na<sup>+</sup>+5Br<sup>-</sup>).

**TAA36**

3 g of 4-bromo-*N,N*-bis(4-methoxyphenyl)aniline (7.81 mmol) were dissolved in 20 ml DCM under Ar atmosphere and cooled down to 0°C. 18.7 ml of boron tribromide (1M in DCM solution, 18.74 mmol) were added and the mixture was left stirring at 0°C for 1 h and allowed to warm up to rt for 5h. The reaction was quenched with NaOH 1M, and HCl was added until acidity. Brine and a Na<sub>2</sub>S<sub>2</sub>O<sub>3</sub> saturated aqueous solution were added to the mixture, which was separated. The product was used without further purification (2.654 g, 95%).

<sup>1</sup>H NMR (300.2 MHz, Acetone-*d*<sub>6</sub>): δ [ppm] = 8.27 (s, 2H), 7.26 (d, 2H), 6.99 (d, 4H), 6.83 (d, 4H) 6.71, 6.69 (d, 2H).

Complete characterization can be found in literature.<sup>207</sup>

**FU15**

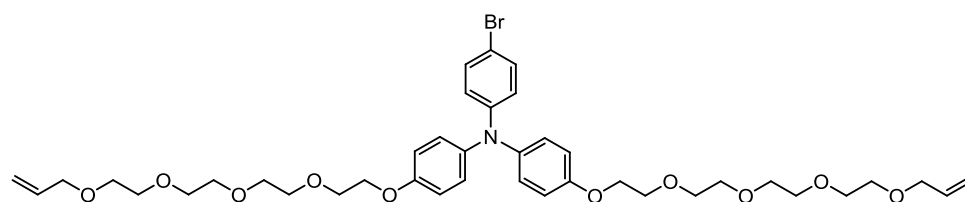
3.00 g of 3,6,9,12-tetraoxapentadec-14-en-1-ol (12.8 mmol) were dissolved in 50 ml DCM at rt. 5.35 ml of NEt<sub>3</sub> (38.4 mmol) were added, and subsequently 4.05 g (21.3 mmol) of TosCl were added portionwise. The mixture was stirred for 5h. 30 ml of water were added to quench and the phases were separated. The aqueous phase was extracted with DCM twice and the combined organic phases were washed with water and brine. After drying over

Na<sub>2</sub>SO<sub>4</sub>, the mixture was evaporated and purified through column chromatography with a gradient of EtOAc:Hex from 4:3 to 2:1. 4.16 g of the product were retrieved (84%).

<sup>1</sup>H-NMR (300.2 MHz, acetone-*d*<sup>6</sup>):  $\delta$ [ppm] = 7.81 (d, 2H), 7.49 (d, 2H), 5.90 (m, 1H), 5.25 (d, 1H), 5.10 (d, 1H), 4.16 (t, 2H), 3.98 (d, 2H), 3.67 (t, 2H), 3.60-3.50 (12H), 2.46 (s, 3H)

Complete characterization can be found in literature.<sup>208</sup>

### TAA38



6.90 g of **FU15** (17.75 mmol) and 12.0 g of K<sub>2</sub>CO<sub>3</sub> (87.00 mmol) were suspended in 100 ml acetone and heated to reflux. 3.10 g of TAA 36 (8.700 mmol) were dissolved in 100 ml acetone and added to the mixture, which was left refluxing for 2 days. After cooling down, the solvent was evaporated and the mixture separated through column chromatography with EtOAc:Hex 4:1 as eluent. 4.250 g of the product were retrieved (5.39 mmol, 62%)

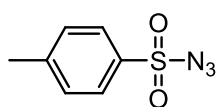
<sup>1</sup>H-NMR (300.2 MHz, acetone-*d*<sup>6</sup>):  $\delta$ [ppm] = 7.33–7.25 (2 H), 7.09–7.01 (4 H), 6.97–6.90 (4 H), 6.80–6.72 (2 H), 5.95–5.80 (m, 2 H), 5.30–5.19

(m, 2 H), 5.13–5.05 (m, 2 H), 4.16–4.08 (m, 4 H), 4.00–3.94 (m, 4 H), 3.84–3.78 (m, 4 H), 3.69–3.49 (24 H).

<sup>13</sup>C-NMR (75.5 MHz, acetone-*d*<sup>6</sup>):  $\delta$ [ppm] = 156.8, 149.3, 141.2, 136.4, 132.6, 127.8, 122.1, 116.5, 116.3, 112.2, 72.4, 71.5, 71.31, 71.25, 70.4, 68.7.

**MS (m/z):** 789.277 (M+H<sup>+</sup>).

### TAA39

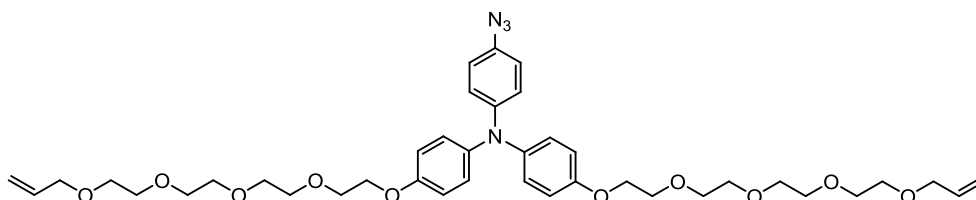


2.86 g of NaN<sub>3</sub> (44 mmol) were suspended in 20 ml of water and 20 ml of acetone. TosCl was dissolved in 20 ml acetone and added quickly to the previous mixture, which was stirred for 4h at rt. The acetone was evaporated and the product was extracted from water using Et<sub>2</sub>O. The organic phase was dried over Na<sub>2</sub>SO<sub>4</sub>, the solution was evaporated giving a yellowish oil (7.39 g, 37.5 mmol, 85%)

<sup>1</sup>H NMR (300.2 MHz, CDCl<sub>3</sub>):  $\delta$ [ppm] = 7.84 (d, 2H), 7.42 (d, 2H), 2.48 (s, 4H).

Complete characterization can be found in literature.<sup>209</sup>

### TAA40



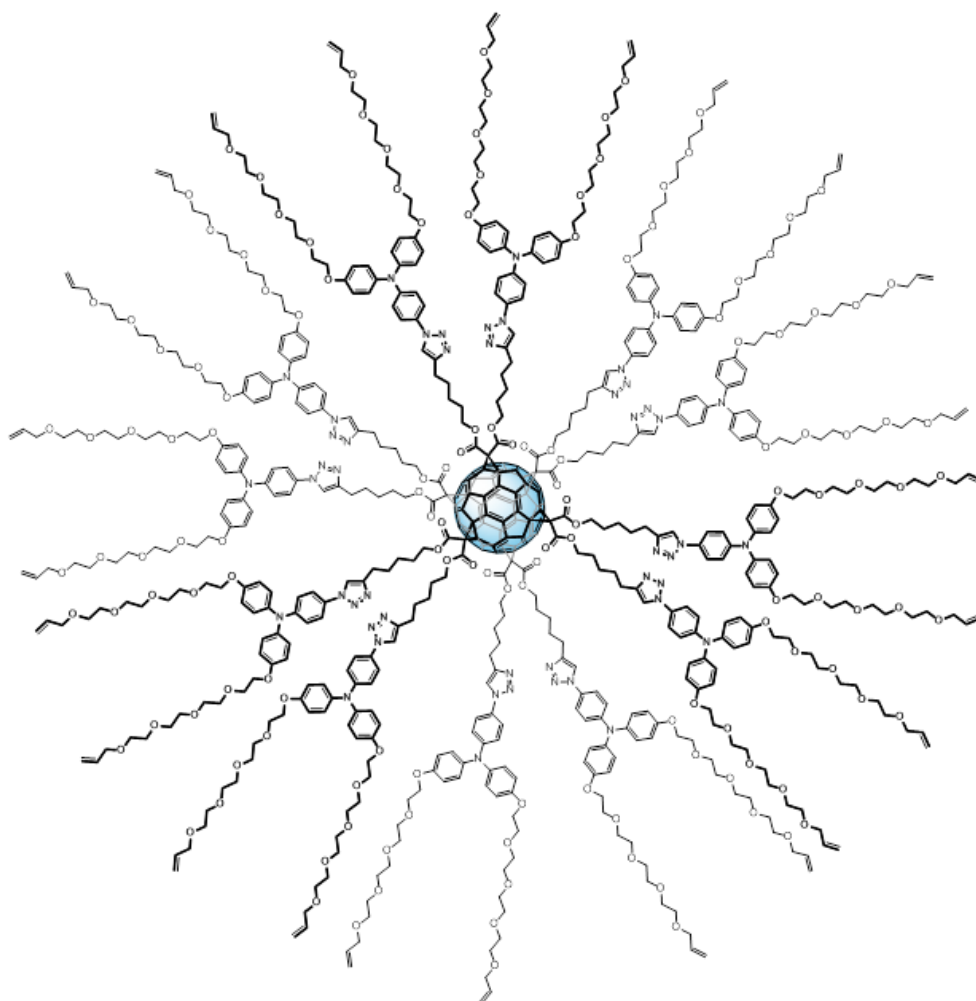
2.50g of **TAA38** (3.17 mmol) were dissolved in 120 ml THF and cooled down to -78°C in an EtOAc bath under Ar atmosphere. 2.97 ml of *n*BuLi (4.75 mmol) were added dropwise and the mixture was stirred for 2h at -78°C. 938 mg of **TAA39** were dissolved in 40 ml THF and added to the solution, which was stirred for one more hour and then allowed to warm up to rt overnight.

THF was evaporated, the residue was extracted three times with DCM and the combined organic phases were washed with water and brine. After drying over Na<sub>2</sub>SO<sub>4</sub> and evaporation of the solvent, the mixture was purified through column chromatography with a gradient of EtOAc:Hex from 3:1 to 4:1. 1.657 g of the final product were obtained (70%, 2.21 mmol)

<sup>1</sup>H-NMR (300.2 MHz, acetone-*d*<sup>6</sup>): δ [ppm] = 7.04–6.97 (4H), 6.96–6.86 (8H), 5.96–5.81 (m, 2H), 5.30–5.19 (2H), 5.14–5.04 (m, 2H), 4.15–4.08 (m, 4H), 4.00–3.94 (m, 4H), 3.85–3.78 (m, 4H), 3.68–3.48 (24H).

<sup>13</sup>C NMR (75.5 MHz, acetone-*d*<sup>6</sup>) δ [ppm] = 156.90, 142.37, 137.03, 130.44, 127.79, 126.56, 125.00, 123.52, 122.08, 121.20, 73.03, 72.09, 72.02, 71.02, 69.28.

**MS** (m/z): 752.2 (M+H<sup>+</sup>). The highest peak corresponds to the ionized species after azide loss (709.3)

**FU26**

250 mg of **FU25** (0.102 mmol), 1.105 g of **TAA40** (1.472 mmol), 151 mg of sodium ascorbate (0.761 mmol) and 63.4 mg of  $\text{CuSO}_4 \cdot 5\text{H}_2\text{O}$  (0.254 mmol) were dissolved in a mixture of 36 ml  $\text{CHCl}_3$ , 18 ml EtOH and 6 ml water. The mixture was stirred in the dark at rt for 6 d. DCM and brine were added to the solution and the phases were separated. Aqueous phase was extracted with DCM three times and the combined organic phases were washed with brine twice. After drying over  $\text{Na}_2\text{SO}_4$ , the solvent was evaporated and the crude product was purified through column chromatography ( $\text{CHCl}_3$ :MeOH

100:3.5). A slightly dirty fraction containing the product was treated with hot Et<sub>2</sub>O (which dissolves TAA40). After filtration, the solid was precipitated with pentane after being dissolved in DCM. 355 mg of a red sticky solid product were obtained (0.03 mmol, 30%).

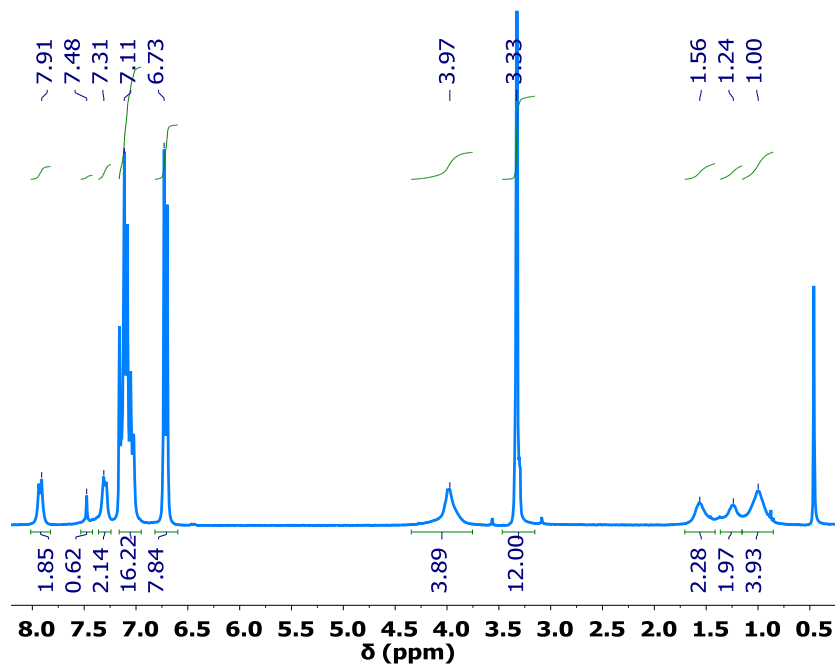
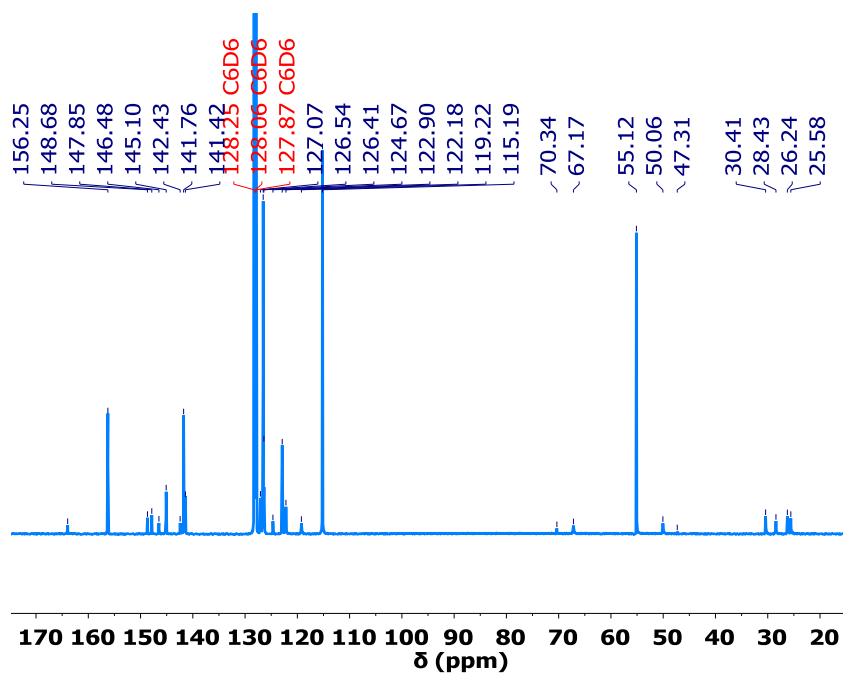
**<sup>1</sup>H-NMR** (300.2 MHz, DCM-*d*<sub>2</sub>):  $\delta$  [ppm] = 8.08 (s, 1 H), 7.70–7.40 (2 H), 7.18–6.98 (4 H), 6.96–6.72 (6 H), 5.97–5.75 (2 H), 5.30–5.15 (2 H), 5.15–5.00 (2H), 4.52–4.15 (2 H), 4.15–4.02 (4 H), 4.02–3.87 (4 H), 3.87–3.70 (4 H), 3.70–3.35 (24 H), 2.77–2.55 (2 H), 1.86–1.26 (6 H). The integration was normalized considering one arm.

**<sup>13</sup>C-NMR** (125.8 MHz, DCM-*d*<sub>2</sub>):  $\delta$  [ppm] = 164.18, 156.16, 149.44, 148.78, 146.24, 140.92, 135.62, 130.39, 127.47, 121.73, 120.56, 119.53, 116.95, 116.06, 72.54, 71.29, 71.09, 70.20, 70.10, 68.33, 29.61, 28.81, 26.10.

**IR** (neat):  $\tilde{\nu}$  [cm<sup>-1</sup>] = 2860, 1740, 1609, 1487, 1441, 1235, 1095, 1029, 927, 815, 703, 609, 525.

**MS (m/z)**: 11493 (M+Na<sup>+</sup>).

## Supplementary Figures

Figure 3.3.21:  $^1\text{H}$  NMR spectrum of FU7 in  $\text{C}_6\text{D}_6$ .Figure 3.3.22:  $^{13}\text{C}$  NMR spectrum of FU7 in  $\text{C}_6\text{D}_6$ .



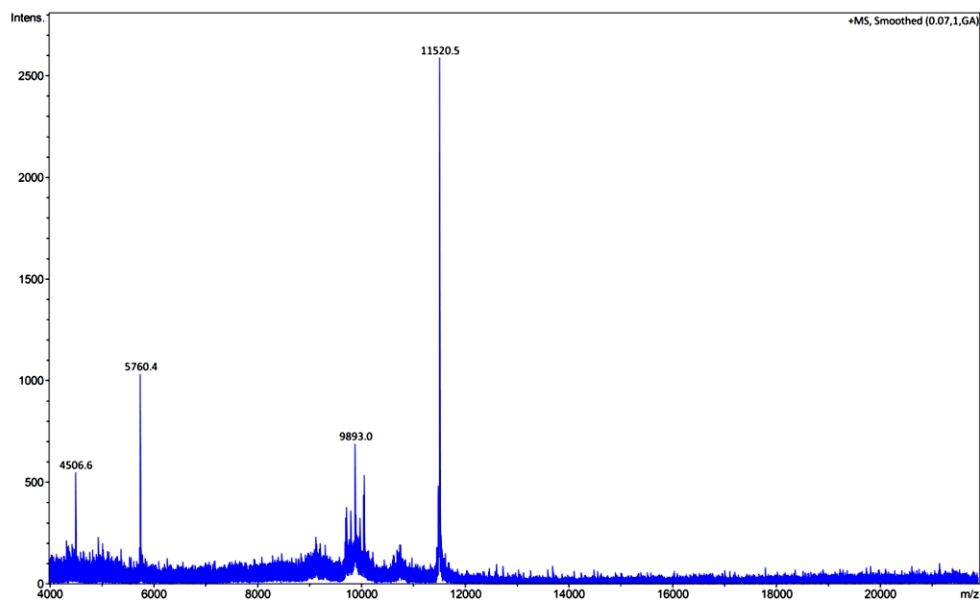


Figure 3.3.23: Complete MALDI-TOF spectrum of FU7.

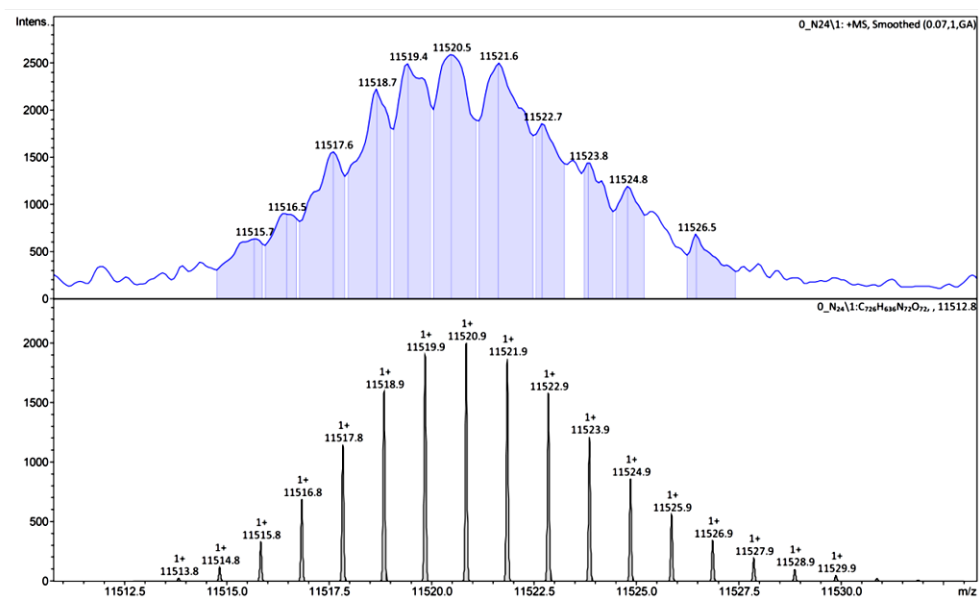


Figure 3.3.24: Amplification of the compound signal in the MALDI-TOF spectra of FU7.

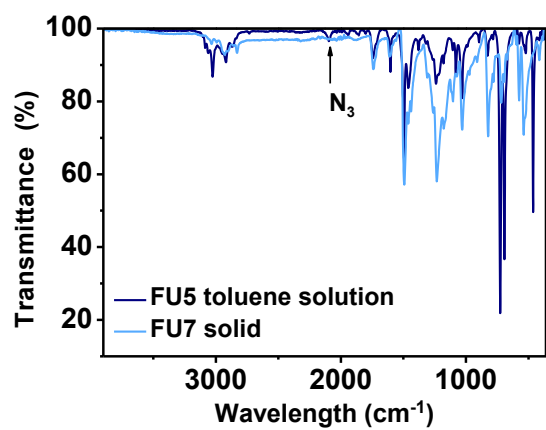


Figure 3.3.25: IR spectra of FU5 (dark blue, in toluene solution) and FU7 (light blue, neat).

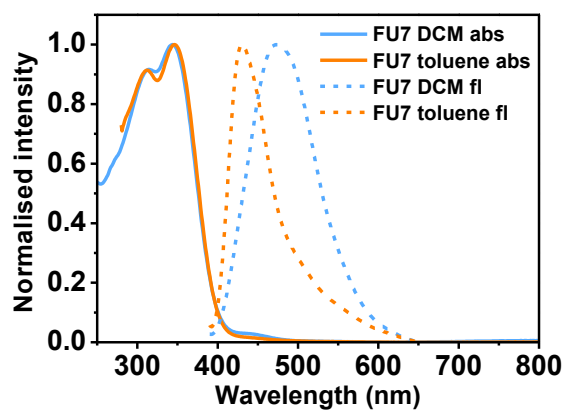


Figure 3.3.26: Absorption (solid lines) and fluorescence (dashed lines) spectra of FU7 in DCM (light blue) and toluene (orange).

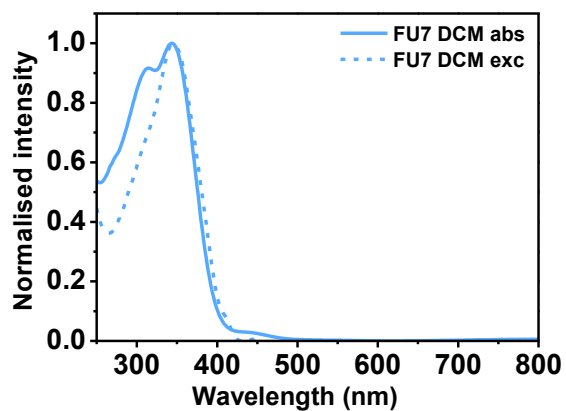


Figure 3.3.27: Absorption (solid line) and excitation (dashed line) spectra of FU7 in DCM.

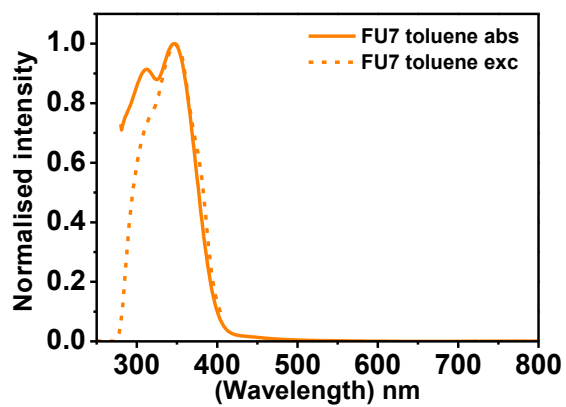


Figure 3.3.28: Absorption (solid line) and excitation (dashed line) spectra of FU7 in toluene.

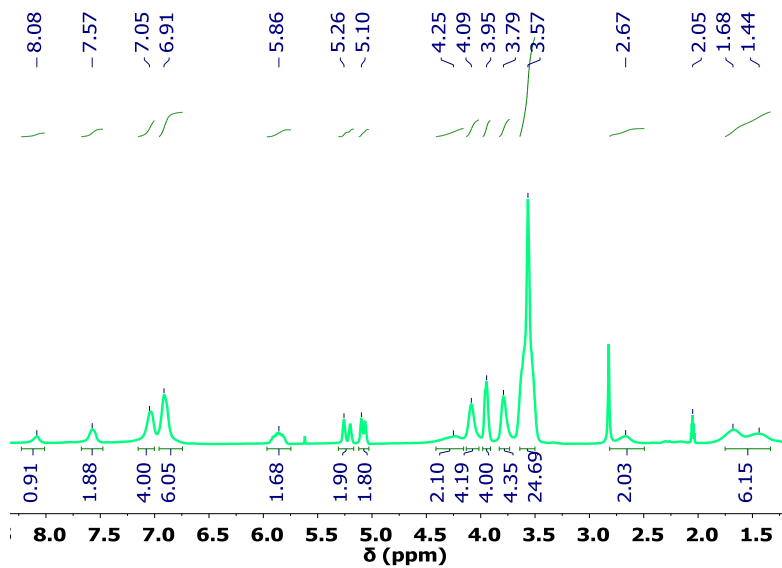


Figure 3.3.29:  $^1\text{H}$  NMR spectrum of FU26 in  $\text{DCM-}d_2$

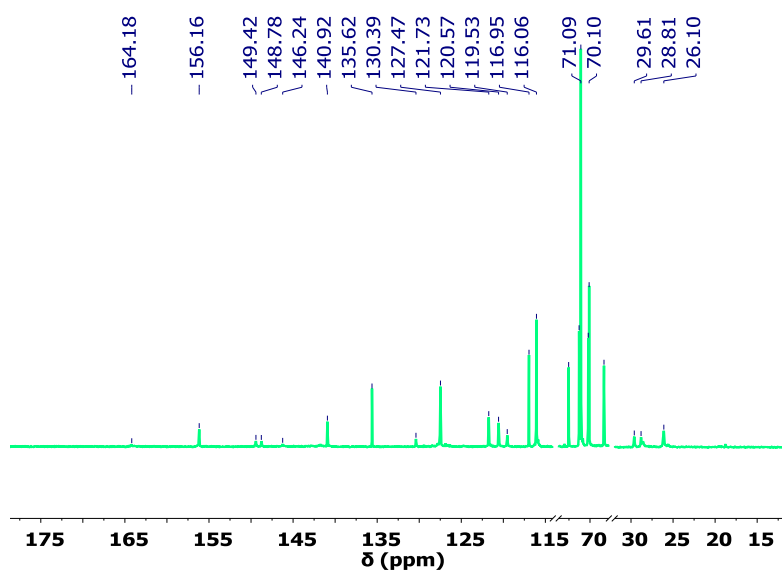


Figure 3.3.30:  $^{13}\text{C}$  NMR spectrum of FU26 in  $\text{DCM-}d_2$

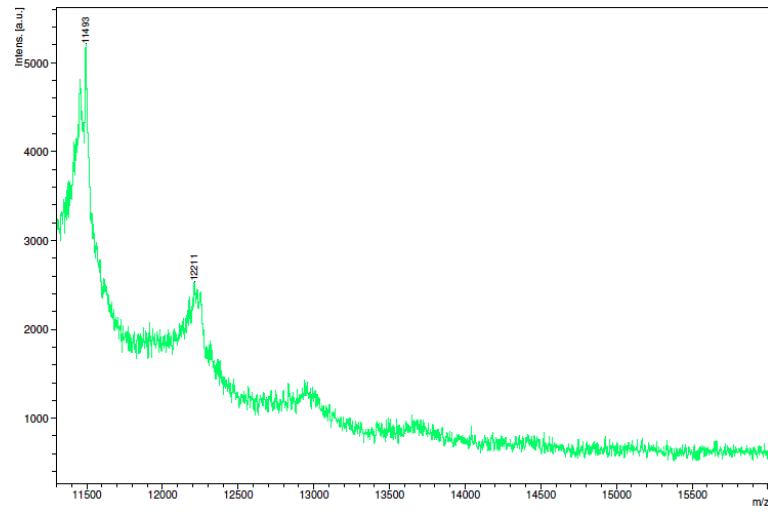


Figure 3.3.31: MALDI-TOF spectrum of FU26.

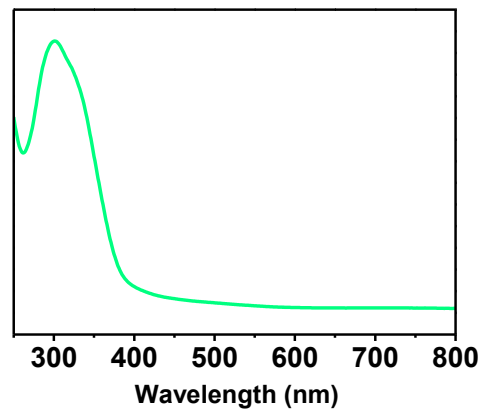


Figure 3.3.32: UV-Vis absorption of FU26 in DCM

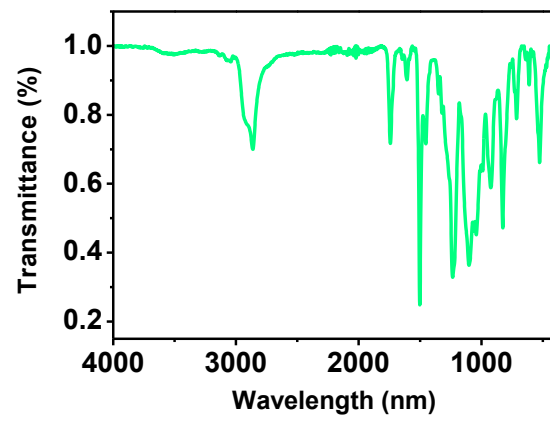


Figure 3.3.33: IR spectra of FU26.

## References

---

1. The World Bank, Energy & Mining, <https://data.worldbank.org/topic/energy-and-mining>.
2. World population projected to reach 9.8 billion in 2050, and 11.2 billion in 2100, <https://www.un.org/development/desa/en/news/population/world-population-prospects-2017.html>.
3. BP Statistical Review of World Energy, <https://www.bp.com/content/dam/bp/pdf/energy-economics/statistical-review-2016/bp-statistical-review-of-world-energy-2016-full-report.pdf>.
4. Sustainable Development Goals, <https://www.un.org/sustainabledevelopment/sustainable-development-goals/>.
5. Photovoltaic Effect, <https://www.britannica.com/science/photovoltaic-effect>.
6. J. Perlin, *Let It Shine: The 6000-Year Story of Solar Energy*, New World Library, 1999.
7. Technology Roadmap-Solar Photovoltaic Energy, [http://www.iea.org/publications/freepublications/publication/TechnologyRoadmapSolarPhotovoltaicEnergy\\_2014edition.pdf](http://www.iea.org/publications/freepublications/publication/TechnologyRoadmapSolarPhotovoltaicEnergy_2014edition.pdf).
8. U.S. Department of Energy's National Renewable Energy Laboratory (NREL), 2016 Renewable Energy Data Book, <https://www.nrel.gov/docs/fy18osti/70231.pdf>.
9. A. McEvoy, L. Castañer, and T. Markvart, *Solar Cells-Materials, Manufacture and Operation*, ScienceDirect, 2013.
10. E. Angnostou and A. F. Forestieri, in *13th IEEE Photovoltaic Specialists Conference*, 1978, 843-845.
11. D. M. Chapin, C. S. Fuller, and G. L. Pearson, *Journal of Applied Physics*, 1954, **25**, 676-677.
12. D. E. Carlson and C. R. Wronski, *Applied Physics Letters*, 1976, **28**, 671-673.
13. E. I. Adirovich, Y. D. Yuabov, and G. R. Yagudaev, *Soviet Physics: Semiconductors*, 1969, **3**, 61-65.

14. D. Bonnet and P. Meyers, *Journal of Materials Research*, 2011, **13**, 2740-2753.
15. B. J. Stanbery, *Critical Reviews in Solid State and Materials Sciences*, 2002, **27**, 73-117.
16. D. P. Bortfeld, A. R. Gobat, N. F. Lamorte, and G. W. McIver, in *1961 International Electron Devices Meeting*, 1961, 36-36.
17. V. Ganapati, M. A. Steiner, and E. Yablonovitch, in *2016 IEEE 43rd Photovoltaic Specialists Conference (PVSC)*, 2016, 3499-3501.
18. R. Xue, J. Zhang, Y. Li, and Y. Li, *Small*, 2018, **14**, 1801793.
19. K. Sharma, V. Sharma, and S. S. Sharma, *Nanoscale Research Letters*, 2018, **13**, 381.
20. C. W. Tang, *Applied Physics Letters*, 1986, **48**, 183-185.
21. S. Rafique, S. M. Abdullah, K. Sulaiman, and M. Iwamoto, *Renewable and Sustainable Energy Reviews*, 2018, **84**, 43-53.
22. N. Marinova, S. Valero, and J. L. Delgado, *Journal of Colloid and Interface Science*, 2017, **488**, 373-389.
23. J. L. Delgado, P. A. Bouit, S. Filippone, M. A. Herranz, and N. Martin, *Chemical Communications*, 2010, **46**, 4853-4865.
24. F. Matsumoto, T. Iwai, K. Moriwaki, Y. Takao, T. Ito, T. Mizuno, and T. Ohno, *ACS Applied Materials & Interfaces*, 2016, **8**, 4803-4810.
25. B. O'Regan and M. Grätzel, *Nature*, 1991, **353**, 737-740.
26. H.-S. Kim, C.-R. Lee, J.-H. Im, K.-B. Lee, T. Moehl, A. Marchioro, S.-J. Moon, R. Humphry-Baker, J.-H. Yum, J. E. Moser, M. Grätzel, and N.-G. Park, *Scientific Reports*, 2012, **2**, 591.
27. M. M. Lee, J. Teuscher, T. Miyasaka, T. N. Murakami, and H. J. Snaith, *Science*, 2012, **338**, 643-647.
28. NREL Record Efficiency Chart, <https://www.nrel.gov/pv/assets/pdfs/pv-efficiency-chart.20181214.pdf>.
29. A. Kojima, K. Teshima, Y. Shirai, and T. Miyasaka, *Journal of the American Chemical Society*, 2009, **131**, 6050-6051.
30. J. Burschka, A. Dualeh, F. Kessler, E. Baranoff, N.-L. Cevey-Ha, C. Yi, M. K. Nazeeruddin, and M. Grätzel, *Journal of the American Chemical Society*, 2011, **133**, 18042-18045.
31. G. Xing, N. Mathews, S. Sun, S. S. Lim, Y. M. Lam, M. Grätzel, S. Mhaisalkar, and T. C. Sum, *Science*, 2013, **342**, 344-347.
32. Q. Dong, Y. Fang, Y. Shao, P. Mulligan, J. Qiu, L. Cao, and J. Huang, *Science*, 2015, **347**, 967-970.
33. Y. Lee, S. Paek, K. T. Cho, E. Oveisi, P. Gao, S. Lee, J.-S. Park, Y. Zhang, R. Humphry-Baker, A. M. Asiri, and M. K. Nazeeruddin, *Journal of Materials Chemistry A*, 2017, **5**, 12729-12734.



34. G. E. Eperon, V. M. Burlakov, P. Docampo, A. Goriely, and H. J. Snaith, *Advanced Functional Materials*, 2014, **24**, 151-157.
35. J.-Y. Jeng, Y.-F. Chiang, M.-H. Lee, S.-R. Peng, T.-F. Guo, P. Chen, and T.-C. Wen, *Advanced Materials*, 2013, **25**, 3727-3732.
36. D. Luo, W. Yang, Z. Wang, A. Sadhanala, Q. Hu, R. Su, R. Shivanna, G. F. Trindade, J. F. Watts, Z. Xu, T. Liu, K. Chen, F. Ye, P. Wu, L. Zhao, J. Wu, Y. Tu, Y. Zhang, X. Yang, W. Zhang, R. H. Friend, Q. Gong, H. J. Snaith, and R. Zhu, *Science*, 2018, **360**, 1442-1446.
37. Y. Li, S. Ye, W. Sun, W. Yan, Y. Li, Z. Bian, Z. Liu, S. Wang, and C. Huang, *Journal of Materials Chemistry A*, 2015, **3**, 18389-18394.
38. L. Wagner, S. Chacko, G. Mathiazhagan, S. Mastroianni, and A. Hinsch, *ACS Energy Letters*, 2018, **3**, 1122-1127.
39. J. Pascual, I. Kosta, T. Tuyen Ngo, A. Chuvilin, G. Cabanero, H. J. Grande, E. M. Barea, I. Mora-Seró, J. L. Delgado, and R. Tena-Zaera, *ChemSusChem*, 2016, **9**, 2679-2685.
40. Q. Zhu, X. Bao, J. Yu, D. Zhu, M. Qiu, R. Yang, and L. Dong, *ACS Applied Materials & Interfaces*, 2016, **8**, 2652-2657.
41. H.-S. Kim, I. Mora-Sero, V. Gonzalez-Pedro, F. Fabregat-Santiago, E. J. Juarez-Perez, N.-G. Park, and J. Bisquert, *Nature Communications*, 2013, **4**, 2242.
42. G. G. V. D'Innocenzo, M.J.P. Alcocer, A.R.S. Kandada, S.D. Stranks, M.M. Lee, G. Lanzani, H.J. Snaith, and A. Petrozza, *Nature Communications*, 2014, **5**, 3586.
43. Q. Lin, A. Armin, R. C. R. Nagiri, P. L. Burn, and P. Meredith, *Nature Photonics*, 2014, **9**, 106-112.
44. M.-F. Lo, Z.-Q. Guan, T.-W. Ng, C.-Y. Chan, and C.-S. Lee, *Advanced Functional Materials*, 2015, **25**, 1213-1218.
45. S. Collavini, S. F. Völker, and J. L. Delgado, *Angewandte Chemie International Edition*, 2015, **54**, 9757-9759.
46. S. F. Völker, S. Collavini, and J. L. Delgado, *ChemSusChem*, 2015, **8**, 3012-3028.
47. Z. Shi and A. Jayatissa, *Materials*, 2018, **11**, 729.
48. P. Vivo, J. Salunke, and A. Priimagi, *Materials*, 2017, **10**, 1087.
49. K. Mahmood, S. Sarwar, and M. T. Mehran, *RSC Advances*, 2017, **7**, 17044-17062.
50. S. Collavini and J. L. Delgado, *Sustainable Energy & Fuels*, 2018, **2**, 2480-2493.
51. L. Etgar, P. Gao, Z. Xue, Q. Peng, A. K. Chandiran, B. Liu, M. K. Nazeeruddin, and M. Grätzel, *Journal of the American Chemical Society*, 2012, **134**, 17396-17399.

52. O. Malinkiewicz, C. Roldán-Carmona, A. Soriano, E. Bandiello, L. Camacho, M. K. Nazeeruddin, and H. J. Bolink, *Advanced Energy Materials*, 2014, **4**, 1400345.
53. T. Leijtens, G. E. Eperon, S. Pathak, A. Abate, M. M. Lee, and H. J. Snaith, *Nature Communications*, 2013, **4**, 2885.
54. J. You, Z. Hong, Y. Yang, Q. Chen, M. Cai, T.-B. Song, C.-C. Chen, S. Lu, Y. Liu, H. Zhou, and Y. Yang, *ACS Nano*, 2014, **8**, 1674-1680.
55. A. Fakharuddin, F. De Rossi, T. M. Watson, L. Schmidt-Mende, and R. Jose, *APL Materials*, 2016, **4**, 091505.
56. E. J. Juarez-Perez, M. R. Leyden, S. Wang, L. K. Ono, Z. Hawash, and Y. Qi, *Chemistry of Materials*, 2016, **28**, 5702-5709.
57. H. Zhou, Q. Chen, G. Li, S. Luo, T. Song, H.-S. Duan, Z. Hong, J. You, Y. Liu, and Y. Yang, *Science*, 2014, **345**, 542-546.
58. Z. Hawash, L. K. Ono, S. R. Raga, M. V. Lee, and Y. Qi, *Chemistry of Materials*, 2015, **27**, 562-569.
59. C. D. Bailie, E. L. Unger, S. M. Zakeeruddin, M. Grätzel, and M. D. McGehee, *Physical Chemistry Chemical Physics*, 2014, **16**, 4864-4870.
60. A. Abrusci, S. D. Stranks, P. Docampo, H.-L. Yip, A. K. Y. Jen, and H. J. Snaith, *Nano Letters*, 2013, **13**, 3124-3128.
61. L. Isaacs, R. F. Haldimann, and F. Diederich, *Angewandte Chemie International Edition*, 1994, **33**, 2339-2342.
62. H. J. Snaith, A. Abate, J. M. Ball, G. E. Eperon, T. Leijtens, N. K. Noel, S. D. Stranks, J. T.-W. Wang, K. Wojciechowski, and W. Zhang, *The Journal of Physical Chemistry Letters*, 2014, **5**, 1511-1515.
63. W. Tress, N. Marinova, T. Moehl, S. M. Zakeeruddin, M. K. Nazeeruddin, and M. Grätzel, *Energy & Environmental Science*, 2015, **8**, 995-1004.
64. E. L. Unger, E. T. Hoke, C. D. Bailie, W. H. Nguyen, A. R. Bowring, T. Heumuller, M. G. Christoforo, and M. D. McGehee, *Energy & Environmental Science*, 2014, **7**, 3690-3698.
65. M. Cai, Y. Wu, H. Chen, X. Yang, Y. Qiang, and L. Han, *Advanced Science*, 2017, **4**, 1600269.
66. G. Niu, X. Guo, and L. Wang, *Journal of Materials Chemistry A*, 2015, **3**, 8970-8980.
67. Z. Wang, Z. Shi, T. Li, Y. Chen, and W. Huang, *Angewandte Chemie International Edition*, 2017, **56**, 1190-1212.
68. B. Conings, J. Drijkoningen, N. Gauquelin, A. Babayigit, J. D'Haen, L. D'Olieslaeger, A. Ethirajan, J. Verbeeck, J. Manca, E. Mosconi, F. D. Angelis, and H.-G. Boyen, *Advanced Energy Materials*, 2015, **5**, 1500477.

69. Y. Li, X. Xu, C. Wang, B. Ecker, J. Yang, J. Huang, and Y. Gao, *The Journal of Physical Chemistry C*, 2017, **121**, 3904-3910.
70. J. P. Bastos, U. W. Paetzold, R. Gehlhaar, W. Qiu, D. Cheyns, S. Surana, V. Spampinato, T. Aernouts, and J. Poortmans, *Advanced Energy Materials*, 2018, **8**, 1800554.
71. G. Abdelmageed, C. Mackeen, K. Hellier, L. Jewell, L. Seymour, M. Tingwald, F. Bridges, J. Z. Zhang, and S. Carter, *Solar Energy Materials and Solar Cells*, 2018, **174**, 566-571.
72. J. Yang, Z. Yuan, X. Liu, S. Braun, Y. Li, J. Tang, F. Gao, C. Duan, M. Fahlman, and Q. Bao, *ACS Applied Materials & Interfaces*, 2018, **10**, 16225-16230.
73. J. M. Frost, K. T. Butler, F. Brivio, C. H. Hendon, M. van Schilfhaarde, and A. Walsh, *Nano Letters*, 2014, **14**, 2584-2590.
74. J. Xu, A. Buin, A. H. Ip, W. Li, O. Voznyy, R. Comin, M. Yuan, S. Jeon, Z. Ning, J. J. McDowell, P. Kanjanaboos, J. P. Sun, X. Lan, L. N. Quan, D. H. Kim, I. G. Hill, P. Maksymovych, and E. H. Sargent, *Nature Communications*, 2015, **6**, 7081.
75. S. Collavini, J. L. Delgado, M. Saliba, W. Tress, P. Holzhey, S. Völker, K. Domanski, S. Turren-cruz, A. Ummadisingu, S. Zakeeruddin, A. Hagfeldt, and M. Grätzel, *ChemSusChem*, 2018, **11**, 1032-1039.
76. K. Wojciechowski, T. Leijtens, S. Siprova, C. Schlueter, M. T. Hörantner, J. T.-W. Wang, C.-Z. Li, A. K. Y. Jen, T.-L. Lee, and H. J. Snaith, *The Journal of Physical Chemistry Letters*, 2015, **6**, 2399-2405.
77. R. C. Haddon, R. E. Palmer, H. W. Kroto, and P. A. Sermon, *Philosophical Transactions of the Royal Society of London. Series A: Physical and Engineering Sciences*, 1993, **343**, 53-62.
78. S. Kirner, M. Sekita, and D. M. Guldi, *Advanced Materials*, 2014, **26**, 1482-1493.
79. C. A. Reed and R. D. Bolskar, *Chemical Reviews*, 2000, **100**, 1075-1120.
80. E. Frankevich, Y. Maruyama, and H. Ogata, *Chemical Physics Letters*, 1993, **214**, 39-44.
81. O. A. Gudaev, V. K. Malinovsky, A. V. Okotrub, and Y. V. Shevtsov, *Fullerene Science and Technology*, 1998, **6**, 433-443.
82. A. A. Popov, S. Yang, and L. Dunsch, *Chemical Reviews*, 2013, **113**, 5989-6113.
83. S. Yang, T. Wei, and F. Jin, *Chemical Society Reviews*, 2017, **46**, 5005-5058.
84. M. Prato, *Journal of Materials Chemistry*, 1997, **7**, 1097-1109.
85. A. Hirsch, *The Chemistry of the Fullerenes*, Wiley VCH, 2008.

86. A. Hirsch, M. Brettreich, and F. Wudl, *Fullerenes Chemistry and Reactions*, Wiley VCH, 2004.
87. E. Castro, A. H. Garcia, G. Zavala, and L. Echegoyen, *Journal of Materials Chemistry B*, 2017, **5**, 6523-6535.
88. Y. Fang, C. Bi, D. Wang, and J. Huang, *ACS Energy Letters*, 2017, **2**, 782-794.
89. H. Imahori and Y. Sakata, *Advanced Materials*, 1997, **9**, 537-546.
90. E. Castro, J. Murillo, O. Fernandez-Delgado, and L. Echegoyen, *Journal of Materials Chemistry C*, 2018, **6**, 2635-2651.
91. S. Collavini and J. L. Delgado, *Advanced Energy Materials*, 2017, **7**, 1601000.
92. L.-L. Deng, S.-Y. Xie, and F. Gao, *Advanced Electronic Materials*, 2018, **4**, 1700435.
93. R. Ganesamoorthy, G. Sathiyam, and P. Sakthivel, *Solar Energy Materials and Solar Cells*, 2017, **161**, 102-148.
94. F. Zhang, O. Inganäs, Y. Zhou, and K. Vandewal, *National Science Review*, 2016, **3**, 222-239.
95. Z. Wu, P. Li, Y. Zhang, and Z. Zheng, *Small Methods*, 2018, **2**, 1800031.
96. F. Zhang, W. Shi, J. Luo, N. Pellet, C. Yi, X. Li, X. Zhao, T. J. S. Dennis, X. Li, S. Wang, Y. Xiao, S. M. Zakeeruddin, D. Bi, and M. Grätzel, *Advanced Materials*, 2017, **29**, 1606806.
97. S. F. Völker, M. Vallés-Pelarda, J. Pascual, S. Collavini, F. Ruiperez, E. Zuccatti, L. E. Hueso, R. Tena-Zaera, I. Mora-Seró, and J. L. Delgado, *Chemistry – A European Journal*, 2018, **24**, 8524-8529.
98. J. C. Hummelen, B. W. Knight, F. LePeq, and F. Wudl, *Journal of Organic Chemistry*, 1995, **60**, 532-538.
99. G. Yu, J. Gao, J. C. Hummelen, F. Wudl, and A. J. Heeger, *Science*, 1995, **270**, 1789-1791.
100. S. E. Shaheen, C. J. Brabec, N. S. Sariciftci, F. Padinger, T. Fromherz, and J. C. Hummelen, *Applied Physics Letters*, 2001, **78**, 841-843.
101. G. Li, V. Shrotriya, J. Huang, Y. Yao, T. Moriarty, K. Emery, and Y. Yang, *Nature Materials*, 2005, **4**, 864-868.
102. J. K. Mwaura, M. R. Pinto, D. Witker, N. Ananthkrishnan, K. S. Schanze, and J. R. Reynolds, *Langmuir*, 2005, **21**, 10119-10126.
103. O. Malinkiewicz, A. Yella, Y. H. Lee, G. M. Espallargas, M. Grätzel, M. K. Nazeeruddin, and H. J. Bolink, *Nature Photonics*, 2014, **8**, 128-132.
104. J. Seo, S. Park, Y. Chan Kim, N. J. Jeon, J. H. Noh, S. C. Yoon, and S. I. Seok, *Energy & Environmental Science*, 2014, **7**, 2642-2646.

105. Z. Xiao, C. Bi, Y. Shao, Q. Dong, Q. Wang, Y. Yuan, C. Wang, Y. Gao, and J. Huang, *Energy & Environmental Science*, 2014, **7**, 2619-2623.
106. W. Zhao, S. Li, H. Yao, S. Zhang, Y. Zhang, B. Yang, and J. Hou, *Journal of the American Chemical Society*, 2017, **139**, 7148-7151.
107. Y. Bai, H. Yu, Z. Zhu, K. Jiang, T. Zhang, N. Zhao, S. Yang, and H. Yan, *Journal of Materials Chemistry A*, 2015, **3**, 9098-9102.
108. C. Kuang, G. Tang, T. Jiu, H. Yang, H. Liu, B. Li, W. Luo, X. Li, W. Zhang, F. Lu, J. Fang, and Y. Li, *Nano Letters*, 2015, **15**, 2756-2762.
109. C. Liu, Y. Li, D. Chi, S. Chen, T. Liu, J. Wang, H. Liu, and Y. Li, *Fullerenes, Nanotubes and Carbon Nanostructures*, 2014, **22**, 289-298.
110. C.-Y. Chang, W.-K. Huang, Y.-C. Chang, K.-T. Lee, and C.-T. Chen, *Journal of Materials Chemistry A*, 2016, **4**, 640-648.
111. Z. Zhu, Q. Xue, H. He, K. Jiang, Z. Hu, Y. Bai, T. Zhang, S. Xiao, K. Gundogdu, B. R. Gautam, H. Ade, F. Huang, K. S. Wong, H.-L. Yip, S. Yang, and H. Yan, *Advanced Science*, 2016, **3**, 1500353.
112. Q. Xue, Z. Hu, J. Liu, J. Lin, C. Sun, Z. Chen, C. Duan, J. Wang, C. Liao, W. M. Lau, F. Huang, H.-L. Yip, and Y. Cao, *Journal of Materials Chemistry A*, 2014, **2**, 19598-19603.
113. G. Kakavelakis, T. Maksudov, D. Konios, I. Paradisanos, G. Kioseoglou, E. Stratakis, and E. Kymakis, *Advanced Energy Materials*, 2017, **7**, 1602120.
114. Y. Shao, Y. Yuan, and J. Huang, *Nature Energy*, 2016, **1**, 15001.
115. C.-H. Chiang, Z.-L. Tseng, and C.-G. Wu, *Journal of Materials Chemistry A*, 2014, **2**, 15897-15903.
116. C.-G. Wu, C.-H. Chiang, Z.-L. Tseng, M. K. Nazeeruddin, A. Hagfeldt, and M. Grätzel, *Energy & Environmental Science*, 2015, **8**, 2725-2733.
117. A. Puplovskis, J. Kacens, and O. Neilands, *Tetrahedron Letters*, 1997, **38**, 285-288.
118. Z. Tan, S. Li, F. Wang, D. Qian, J. Lin, J. Hou, and Y. Li, *Scientific Reports*, 2014, **4**, 4691.
119. C. Bi, Y. Yuan, Y. Fang, and J. Huang, *Advanced Energy Materials*, 2015, **5**, 1401616.
120. Y.-Y. Lai, Y.-J. Cheng, and C.-S. Hsu, *Energy & Environmental Science*, 2014, **7**, 1866-1883.
121. P.-W. Liang, C.-C. Chueh, S. T. Williams, and A. K. Y. Jen, *Advanced Energy Materials*, 2015, **5**, 1402321.
122. S. Collavini, I. Kosta, S. F. Völker, G. Cabanero, H. J. Grande, R. Tena-Zaera, and J. L. Delgado, *ChemSusChem*, 2016, **9**, 1263-1270.

123. C. Tian, S. Zhang, A. Mei, Y. Rong, Y. Hu, K. Du, M. Duan, Y. Sheng, P. Jiang, G. Xu, and H. Han, *ACS Applied Materials & Interfaces*, 2018, **10**, 10835-10841.
124. C.-B. Tian, K. Kochiss, E. Castro, G. Betancourt-Solis, H. Han, and L. Echegoyen, *Journal of Materials Chemistry A*, 2017, **5**, 7326-7332.
125. Y. Li, Y. Zhao, Q. Chen, Y. Yang, Y. Liu, Z. Hong, Z. Liu, Y.-T. Hsieh, L. Meng, Y. Li, and Y. Yang, *Journal of the American Chemical Society*, 2015, **137**, 15540-15547.
126. Q.-Q. Ye, Z.-K. Wang, M. Li, C.-C. Zhang, K.-H. Hu, and L.-S. Liao, *ACS Energy Letters*, 2018, **3**, 875-882.
127. S. Erten-Ela, H. Chen, A. Kratzer, A. Hirsch, and C. J. Brabec, *New Journal of Chemistry*, 2016, **40**, 2829-2834.
128. Y. Bai, Q. Dong, Y. Shao, Y. Deng, Q. Wang, L. Shen, D. Wang, W. Wei, and J. Huang, *Nature Communications*, 2016, **7**, 12806.
129. B. G. H. M. Groeneveld, M. Najafi, B. Steensma, S. Adjokatse, H.-H. Fang, F. Jahani, L. Qiu, G. H. t. Brink, J. C. Hummelen, and M. A. Loi, *APL Materials*, 2017, **5**, 076103.
130. C. Tian, E. Castro, T. Wang, G. Betancourt-Solis, G. Rodriguez, and L. Echegoyen, *ACS Applied Materials & Interfaces*, 2016, **8**, 31426-31432.
131. S. Shao, M. Abdu-Aguye, L. Qiu, L.-H. Lai, J. Liu, S. Adjokatse, F. Jahani, M. E. Kamminga, G. H. ten Brink, T. T. M. Palstra, B. J. Kooi, J. C. Hummelen, and M. Antonietta Loi, *Energy & Environmental Science*, 2016, **9**, 2444-2452.
132. C. Liu, K. Wang, P. Du, C. Yi, T. Meng, and X. Gong, *Advanced Energy Materials*, 2015, **5**, 1402024.
133. C.-H. Chiang and C.-G. Wu, *Nature Photonics*, 2016, **10**, 196-200.
134. K. Wang, C. Liu, P. Du, J. Zheng, and X. Gong, *Energy & Environmental Science*, 2015, **8**, 1245-1255.
135. X. Liu, F. Lin, C.-C. Chueh, Q. Chen, T. Zhao, P.-W. Liang, Z. Zhu, Y. Sun, and A. K. Y. Jen, *Nano Energy*, 2016, **30**, 417-425.
136. C. Liu, W. Li, H. Li, C. Zhang, J. Fan, and Y. Mai, *Nanoscale*, 2017, **9**, 13967-13975.
137. J. Xu, A. Buin, A. H. Ip, W. Li, O. Voznyy, R. Comin, M. Yuan, S. Jeon, Z. Ning, J. J. McDowell, P. Kanjanaboos, J.-P. Sun, X. Lan, L. N. Quan, D. H. Kim, I. G. Hill, P. Maksymovych, and E. H. Sargent, *Nature Communications*, 2015, **6**, 7081.
138. C. Park, H. Ko, D. H. Sin, K. C. Song, and K. Cho, *Advanced Functional Materials*, 2017, **27**, 1703546.
139. N. J. Jeon, J. H. Noh, Y. C. Kim, W. S. Yang, S. Ryu, and S. I. Seok, *Nature Materials*, 2014, **13**, 897-903.

140. J. Pascual, I. Kosta, E. Palacios-Lidon, A. Chuvilin, G. Grancini, M. K. Nazeeruddin, H. J. Grande, J. L. Delgado, and R. Tena-Zaera, *The Journal of Physical Chemistry C*, 2018, **122**, 2512-2520.
141. Y. Shao, Z. Xiao, C. Bi, Y. Yuan, and J. Huang, *Nature Communications*, 2014, **5**, 5784.
142. R. Sandoval-Torrientes, J. Pascual, I. García-Benito, S. Collavini, I. Kosta, R. Tena-Zaera, N. Martín, and J. L. Delgado, *ChemSusChem*, 2017, **10**, 2023-2029.
143. T. Gatti, E. Menna, M. Meneghetti, M. Maggini, A. Petrozza, and F. Lamberti, *Nano Energy*, 2017, **41**, 84-100.
144. L. Echegoyen and L. E. Echegoyen, *Accounts of Chemical Research*, 1998, **31**, 593-601.
145. S. Pfuetzner, J. Meiss, A. Petrich, M. Riede, and K. Leo, *Applied Physics Letters*, 2009, **94**, 223307.
146. J. L. Delgado, E. Espíldora, M. Liedtke, A. Sperlich, D. Rauh, A. Baumann, C. Deibel, V. Dyakonov, and N. Martín, *Chemistry – A European Journal*, 2009, **15**, 13474-13482.
147. M. M. Wienk, J. M. Kroon, W. J. H. Verhees, J. Knol, J. C. Hummelen, P. A. van Hal, and R. A. J. Janssen, *Angewandte Chemie International Edition*, 2003, **42**, 3371-3375.
148. S. H. Park, A. Roy, S. Beaupre, S. Cho, N. Coates, J. S. Moon, D. Moses, M. Leclerc, K. Lee, and A. J. Heeger, *Nat Photon*, 2009, **3**, 297-302.
149. J. A. Mikroyannidis, A. N. Kabanakis, S. S. Sharma, and G. D. Sharma, *Advanced Functional Materials*, 2011, **21**, 746-755.
150. S. P. Singh, C. H. P. Kumar, G. D. Sharma, R. Kurchania, and M. S. Roy, *Advanced Functional Materials*, 2012, **22**, 4087-4095.
151. J.-W. Lee and N.-G. Park, *MRS Bulletin*, 2015, **40**, 654-659.
152. S. T. Williams, F. Zuo, C.-C. Chueh, C.-Y. Liao, P.-W. Liang, and A. K. Y. Jen, *ACS Nano*, 2014, **8**, 10640-10654.
153. Y. Tidhar, E. Edri, H. Weissman, D. Zohar, G. Hodes, D. Cahen, B. Rybtchinski, and S. Kirmayer, *Journal of the American Chemical Society*, 2014, **136**, 13249-13256.
154. P. Docampo, F. C. Hanusch, N. Giesbrecht, P. Angloher, A. Ivanova, and T. Bein, *APL Materials*, 2014, **2**, 081508.
155. D. Zhao, M. Sexton, H.-Y. Park, G. Baure, J. C. Nino, and F. So, *Advanced Energy Materials*, 2015, **5**, 1401855.
156. D. Shen, X. Yu, X. Cai, M. Peng, Y. Ma, X. Su, L. Xiao, and D. Zou, *Journal of Materials Chemistry A*, 2014, **2**, 20454-20461.

157. W. Ke, D. Zhao, C. R. Grice, A. J. Cimaroli, J. Ge, H. Tao, H. Lei, G. Fang, and Y. Yan, *Journal of Materials Chemistry A*, 2015, **3**, 17971-17976.
158. Y. Zhao, J. Wei, H. Li, Y. Yan, W. Zhou, D. Yu, and Q. Zhao, *Nature Communications*, 2016, **7**, 10228.
159. C. Bingel, *Chemische Berichte*, 1993, **126**, 1957-1959.
160. M. Maggini, G. Scorrano, and M. Prato, *Journal of the American Chemical Society*, 1993, **115**, 9798-9799.
161. M. Cases, M. Duran, J. Mestres, N. Martín, and M. Solà, *The Journal of Organic Chemistry*, 2001, **66**, 433-442.
162. K. Kordatos, T. Da Ros, M. Prato, R. V. Bensasson, and S. Leach, *Chemical Physics*, 2003, **293**, 263-280.
163. N. G. Connelly and W. E. Geiger, *Chemical Reviews*, 1996, **96**, 877-910.
164. V. V. Pavlishchuk and A. W. Addison, *Inorganica Chimica Acta*, 2000, **298**, 97-102.
165. D. Tsiplakides, D. Archonta, and C. G. Vayenas, *Topics in Catalysis*, 2007, **44**, 469-479.
166. M. Saliba, T. Matsui, J.-Y. Seo, K. Domanski, J.-P. Correa-Baena, M. K. Nazeeruddin, S. M. Zakeeruddin, W. Tress, A. Abate, A. Hagfeldt, and M. Grätzel, *Energy & Environmental Science*, 2016, **9**, 1989-1997.
167. N. Wu, Y. Wu, D. Walter, H. Shen, T. Duong, D. Grant, C. Barugkin, X. Fu, J. Peng, T. White, K. Catchpole, and K. Weber, *Energy Technology*, 2017, **5**, 1827-1835.
168. Y. Hou, S. Scheiner, X. Tang, N. Gasparini, M. Richter, N. Li, P. Schweizer, S. Chen, H. Chen, C. O. R. Quiroz, X. Du, G. J. Matt, A. Osvet, E. Spiecker, R. H. Fink, A. Hirsch, M. Halik, and C. J. Brabec, *Advanced Materials Interfaces*, 2017, **4**, 1700007.
169. J. Wei, H. Li, Y. Zhao, W. Zhou, R. Fu, Y. Leprince-Wang, D. Yu, and Q. Zhao, *Nano Energy*, 2016, **26**, 139-147.
170. S. Kachbi-Khelfallah, M. Monteil, M. Cortes-Clerget, E. Migianu-Griffoni, J.-L. Pirat, O. Gager, J. Deschamp, and M. Lecouvey, *Beilstein Journal of Organic Chemistry*, 2016, **12**, 1366-1371.
171. S. M. Standley, Y. J. Kwon, N. Murthy, J. Kunisawa, N. Shastri, S. J. Guillaudeu, L. Lau, and J. M. J. Fréchet, *Bioconjugate Chemistry*, 2004, **15**, 1281-1288.
172. X. Pan, C. Chen, J. Peng, Y. Yang, Y. Wang, W. Feng, P. Deng, and L. Yuan, *Chemical Communications*, 2012, **48**, 9510-9512.
173. C. Cui, Y. Li, and Y. Li, *Advanced Energy Materials*, 2017, **7**, 1601251.



174. S. F. Völker, S. Collavini, and J. L. Delgado, *ChemSusChem*, 2015, **8**, 3012-3028.
175. Y. Takano, S. Obuchi, N. Mizorogi, R. García, M. Á. Herranz, M. Rudolf, D. M. Guldi, N. Martín, S. Nagase, and T. Akasaka, *Journal of the American Chemical Society*, 2012, **134**, 19401-19408.
176. T. Zhuang, X.-F. Wang, T. Sano, Z. Hong, Y. Yang, and J. Kido, *Applied Physics Letters*, 2013, **103**, 203301.
177. J. Iehl, R. Pereira de Freitas, B. Delavaux-Nicot, and J.-F. Nierengarten, *Chemical Communications*, 2008, 2450-2452.
178. J.-F. Nierengarten, *Chemical Communications*, 2017, **53**, 11855-11868.
179. C. Boudon, J.-P. Gisselbrecht, M. Gross, L. Isaacs, H. L. Anderson, R. Faust, and F. Diederich, *Helvetica Chimica Acta*, 1995, **78**, 1334-1344.
180. C. Thilgen and F. Diederich, *Chemical Reviews*, 2006, **106**, 5049-5135.
181. P. Compain, C. Decroocq, J. Iehl, M. Holler, D. Hazeldard, T. Mena Barragán, C. Ortiz Mellet, and J.-F. Nierengarten, *Angewandte Chemie*, 2010, **122**, 5889-5892.
182. J.-F. Nierengarten, J. Iehl, V. Oerthel, M. Holler, B. M. Illescas, A. Muñoz, N. Martín, J. Rojo, M. Sánchez-Navarro, S. Cecioni, S. Vidal, K. Buffet, M. Durka, and S. P. Vincent, *Chemical Communications*, 2010, **46**, 3860-3862.
183. A. Varki, *Glycobiology*, 1993, **3**, 97-130.
184. C. R. Bertozzi and L. L. Kiessling, *Science*, 2001, **291**, 2357.
185. J. Luczkowiak, A. Muñoz, M. Sánchez-Navarro, R. Ribeiro-Viana, A. Ginieis, B. M. Illescas, N. Martín, R. Delgado, and J. Rojo, *Biomacromolecules*, 2013, **14**, 431-437.
186. A. Muñoz, D. Sigwalt, B. M. Illescas, J. Luczkowiak, L. Rodríguez-Pérez, I. Nierengarten, M. Holler, J.-S. Remy, K. Buffet, S. P. Vincent, J. Rojo, R. Delgado, J.-F. Nierengarten, and N. Martín, *Nature Chemistry*, 2015, **8**, 50.
187. D. Sigwalt, M. Holler, J. Iehl, J.-F. Nierengarten, M. Nothisen, E. Morin, and J.-S. Remy, *Chemical Communications*, 2011, **47**, 4640-4642.
188. J. Iehl, M. Holler, J.-F. Nierengarten, K. Yoosaf, J. M. Malicka, N. Armaroli, and B. Delavaux-Nicot, *Australian Journal of Chemistry*, 2011, **64**, 153-159.
189. M. J. Frisch, G. W. Trucks, H. B. Schlegel, G. E. Scuseria, M. A. Robb, J. R. Cheeseman, G. Scalmani, V. Barone, G. A. Petersson, H. Nakatsuji, X. Li, M. Caricato, A. V. Marenich, J. Bloino, B. G. Janesko, R. Gomperts, B. Mennucci, H. P. Hratchian, J. V. Ortiz, A. F. Izmaylov, J. L. Sonnenberg, Williams, F. Ding, F. Lipparini, F. Egidi, J. Goings, B. Peng, A. Petrone, T. Henderson, D. Ranasinghe, V. G. Zakrzewski, J. Gao, N. Rega, G. Zheng, W. Liang, M. Hada, M.

- Ehara, K. Toyota, R. Fukuda, J. Hasegawa, M. Ishida, T. Nakajima, Y. Honda, O. Kitao, H. Nakai, T. Vreven, K. Throssell, J. A. Montgomery Jr., J. E. Peralta, F. Ogliaro, M. J. Bearpark, J. J. Heyd, E. N. Brothers, K. N. Kudin, V. N. Staroverov, T. A. Keith, R. Kobayashi, J. Normand, K. Raghavachari, A. P. Rendell, J. C. Burant, S. S. Iyengar, J. Tomasi, M. Cossi, J. M. Millam, M. Klene, C. Adamo, R. Cammi, J. W. Ochterski, R. L. Martin, K. Morokuma, O. Farkas, J. B. Foresman, and D. J. Fox, Gaussian 09, Revision A.1. Gaussian Inc., Wallingford, CT, 2016.
190. B. W. Larson, J. B. Whitaker, X.-B. Wang, A. A. Popov, G. Rumbles, N. Kopidakis, S. H. Strauss, and O. V. Boltalina, *The Journal of Physical Chemistry C*, 2013, **117**, 14958-14964.
191. C. H. Teh, R. Daik, E. L. Lim, C. C. Yap, M. A. Ibrahim, N. A. Ludin, K. Sopian, and M. A. Mat Teridi, *Journal of Materials Chemistry A*, 2016, **4**, 15788-15822.
192. S. Kazim, F. J. Ramos, P. Gao, M. K. Nazeeruddin, M. Grätzel, and S. Ahmad, *Energy & Environmental Science*, 2015, **8**, 1816-1823.
193. M. Cheng, C. Chen, X. Yang, J. Huang, F. Zhang, B. Xu, and L. Sun, *Chemistry of Materials*, 2015, **27**, 1808-1814.
194. C. Aranda, C. Cristobal, L. Shooshtari, C. Li, S. Huettner, and A. Guerrero, *Sustainable Energy & Fuels*, 2017, **1**, 540-547.
195. E. J. Juarez-Perez, M. Wußler, F. Fabregat-Santiago, K. Lakus-Wollny, E. Mankel, T. Mayer, W. Jaegermann, and I. Mora-Sero, *The Journal of Physical Chemistry Letters*, 2014, **5**, 680-685.
196. A. Guerrero, G. Garcia-Belmonte, I. Mora-Sero, J. Bisquert, Y. S. Kang, T. J. Jacobsson, J.-P. Correa-Baena, and A. Hagfeldt, *The Journal of Physical Chemistry C*, 2016, **120**, 8023-8032.
197. S. Paek, P. Qin, Y. Lee, K. T. Cho, P. Gao, G. Grancini, E. Oveisi, P. Gratia, K. Rakstys, S. A. Al-Muhtaseb, C. Ludwig, J. Ko, and M. K. Nazeeruddin, *Advanced Materials*, 2017, **29**, 1606555.
198. A. Dualeh, T. Moehl, N. Tétreault, J. Teuscher, P. Gao, M. K. Nazeeruddin, and M. Grätzel, *ACS Nano*, 2014, **8**, 362-373.
199. H.-S. Kim, J.-W. Lee, N. Yantara, P. P. Boix, S. A. Kulkarni, S. Mhaisalkar, M. Gratzel, and N.-G. Park, *Nano Lett.*, 2013, **16**, 2412-2417.
200. J. Jiménez-López, W. Cambarau, L. Cabau, and E. Palomares, *Scientific Reports*, 2017, **7**, 6101.
201. D.-Y. Son, J.-W. Lee, Y. J. Choi, I.-H. Jang, S. Lee, P. J. Yoo, H. Shin, N. Ahn, M. Choi, D. Kim, and N.-G. Park, *Nature Energy*, 2016, **1**, 16081.

202. A. Fakharuddin, L. Schmidt-Mende, G. Garcia-Belmonte, R. Jose, and I. Mora-Sero, *Advanced Energy Materials*, 2017, 1700623.
203. D. M. Guldi and N. Martin, *Fullerenes: From Synthesis to Optoelectronic Properties*, Springer Netherlands, 2002.
204. F. Langa and J.-F. Nierengarten, *Fullerenes. Principles and Applications*, RSC, Cambridge, United Kingdom, 2007.
205. J. O. Mueller, N. K. Guimard, K. K. Oehlenschlaeger, F. G. Schmidt, and C. Barner-Kowollik, *Polymer Chemistry*, 2014, **5**, 1447-1456.
206. C. Lambert, J. Schelter, T. Fiebig, D. Mank, and A. Trifonov, *Journal of the American Chemical Society*, 2005, **127**, 10600-10610.
207. S. Maniam, A. B. Holmes, G. A. Leeke, A. Bilic, and G. E. Collis, *Organic Letters*, 2015, **17**, 4022-4025.
208. A. T. Dickschat, F. Behrends, M. Bühner, J. Ren, M. Weiß, H. Eckert, and A. Studer, *Chemistry – A European Journal*, 2012, **18**, 16689-16697.
209. P. Kumar, T. Jiang, S. Li, O. Zainul, and S. T. Laughlin, *Organic & Biomolecular Chemistry*, 2018, **16**, 4081-4085.